



POLITECNICO DI MILANO  
DEPARTMENT OF ENERGY  
DOCTORAL PROGRAMME IN XXIX

---

NUMERICAL STUDY OF COHERENT STRUCTURES OF  
IN-CYLINDER FLOW BY A HYBRID RANS/LES MODEL

Doctoral Dissertation of:

**Yan Wu**

Supervisor:

**Prof. Federico Piscaglia**

Tutor:

**Prof. Angelo Onorati**

The Chair of the Doctoral Program:

**Prof. Carlo Enrico Bottani**

2016 - XXIX Cycle STEN



*Dedicated to my **parents, Wu and Li,***

*whose love supports me through  
all my panic and happiness.*



---

---

## Acknowledgements

---

First and foremost, I should express my sincere gratitude to my supervisor Prof. Federico Piscaglia, who introduced me into an entire new world of research and supported me constantly through the last three years.

I would also like to thank my tutor Prof. Angelo Onorati, who accepted me into the PhD programme in Department of Energy, through which he always gave me important advices.

My sincere thanks must also go to Dr. Andrea Montorfano, for his most patient and selfless guidance on computational fluid dynamics.

I would always be in debt to my family, whose love and support calm me down in my most difficult times.

Last and most importantly, I owe my gratitude to all the colleagues in ICE Group, your friendship, kindness and courage are my most precious treasure in this beautiful land. It is an honour to have been working with you side by side.



---

---

## Abstract

---

**T**HE present work focuses on the development and application of computational fluid dynamics (CFD) methods to the study of turbulent in-cylinder flow. The thesis work consists three parts.

In the first part, a scale resolving turbulence model [63] is further developed with more robust definition of the resolvable turbulence length scale, considering both spatial and temporal numerical resolution, which allows a dynamic damping/filtering behaviour and improved adaptivity to coarse mesh and large time step.

In the second part, enhancement of dynamic mesh strategy is applied for faster mesh interfacing and better description of the moving mesh boundaries. The COUPLING/DECOUPLING mechanism of the dynamic mesh interfacing is optimized so that redundant renumbering of the grid points is avoided, the abstraction overhead from generic programming is also reduced.

Validation of the developments made in the first two parts are performed through comprehensive comparison against experimental measurement and simulation results using the state of art RANS and LES turbulence models. It is confirmed that the proposed numerical methods are capable to resolve sufficient flow scales where the numerical resolution suffices, while recover to an computational efficient RANS model where the local grid reaches its coarse limit.

In the final part the cycle-dependent engine flow is analysed by means of proper orthogonal decomposition (POD). The results confirm that the leading POD mode corresponds closely to the ensemble mean flow even for vector field. Energy transfer between coherent structures in different POD modes are also analysed.

**Keywords** CFD, Engine Flow, Hybrid RANS/LES, DLRM, Dynamic Mesh, POD, Coherent Structure





---

---

# Contents

---

<b>1</b>	<b>Introduction</b>	<b>5</b>
1.1	Challenges of numerical study of turbulent in-cylinder flow . . . . .	5
1.2	Objective, approach and structure of the thesis . . . . .	8
<b>2</b>	<b>Turbulence method</b>	<b>11</b>
2.1	Turbulence scales and their modelling . . . . .	11
2.1.1	Range of turbulence scales in engine flow . . . . .	11
2.1.2	Scale separation and turbulence modelling . . . . .	12
2.2	RANS and LES . . . . .	13
2.3	Promising of Hybrid RANS/LES . . . . .	14
2.3.1	Zonal method . . . . .	15
2.3.2	Non-zonal method . . . . .	15
2.4	Scale resolving simulation of engine flows . . . . .	16
<b>3</b>	<b>Dynamic length-scale resolution model</b>	<b>19</b>
3.1	Formulation of length scales . . . . .	20
3.2	“Filtering” behaviour . . . . .	21
<b>4</b>	<b>Dynamic mesh strategy</b>	<b>25</b>
4.1	Moving boundaries of IC engine . . . . .	25

## Contents

---

4.2	Layer A/R . . . . .	26
4.3	Dynamic mesh interfacing . . . . .	27
4.3.1	Sliding interface . . . . .	28
4.3.2	ACMI . . . . .	30
4.4	Mass conservation . . . . .	30
<b>5</b>	<b>Validation of the numerical method</b>	<b>33</b>
5.1	Test case . . . . .	33
5.2	Numerical set-up . . . . .	35
5.2.1	Grids . . . . .	35
5.2.2	Boundary and initial conditions . . . . .	36
5.2.3	Solution of NS equation and discretization schemes . . . . .	38
5.3	Post-processing and Results . . . . .	39
5.3.1	“Uncompressed-vortex” case . . . . .	40
5.3.2	“Compressed-vortex” case . . . . .	46
<b>6</b>	<b>Coherent structure of in-cylinder flow</b>	<b>79</b>
6.1	Dynamic system and dimension reduction . . . . .	79
6.2	Proper orthogonal decomposition . . . . .	81
6.2.1	Concept and equations . . . . .	81
6.2.2	POD on engine flow . . . . .	83
6.3	Results and analysis . . . . .	85
<b>7</b>	<b>Conclusion</b>	<b>91</b>
	<b>Bibliography</b>	<b>93</b>

---

# CHAPTER *1*

---

## Introduction

---

### **1.1 Challenges of numerical study of turbulent in-cylinder flow**

---

Internal Combustion (IC) engines will continue to be the main propulsion technology for transportation. The growing demands for mobility, increasingly stringent emission regulation and the limited reserve of fossil fuel resources are ongoing driven forces behind the development of IC engines towards lower emission, higher efficiency and better reliability. Due to sophisticated geometry and the various complex thermo-physical processes involved, a comprehensive knowledge of engine behaviour and its governing processes could only be achieved by close interaction between reliable numerical simulations and properly designed experimental validation. The capacity to predict of the ongoing mechanisms in situations that are inaccessible to experiment, concurrent to the progress of high performance computing power, allows physics-based computational fluid dynamics (CFD) becoming a necessary and useful designed tool in automobile industry.

Engine process consists of complex, mutually interacting kinetic phenomena, including spray atomization, droplet-droplet interaction during fuel injection, onset of the chemical reaction, and pollutant formation. All of them are carried or even directly coupled with in-cylinder flow, and the non-linear nature of turbulence is one of the most critical challenges to face for the study of thermal power processes of several industries. In particular for IC engines, the flow is intrinsically unsteady and the occurrence of cyclic variation, or sometimes termed as “cycle-to-cycle variations” (CCV), is of great relevance for industrial design. CCV is particularly important for spark-ignition engines, as turbulence is directly coupled with air/fuel mixing, the overall speed of combustion is also influenced by flow unsteadiness. Cyclic fluctuations of charge composition and turbulence level during intake and compression stroke result in very different local conditions around the spark-plug at ignition time, and this in turn affects formation of initial flame kernel and the mixture characteristic burning speed. The optimal timing of spark or injection varies due to the variation of initial conditions among different engine cycles. In fact, large CCV in the fuel mixture may increase the covariance of indicated mean effective pressure which induces combustion instabilities that may result in engine roughness, transient vehicle vibration, or even engine knock or misfire, which have direct impact on engine efficiency and its emission control [33, 35, 80, 86].

Numerical investigation of engine CCV requires accurate information on the evolution of turbulent flow structures. Different numerical methods provide different levels of detail on flow unsteadiness [75], and scale resolving methods should be the minimum requirement for the study of engine CCV [33, 69], which unfortunately eludes the use of well developed Reynolds averaged Navier-Stokes (RANS) methods. Academic research resorts to Large-eddy simulation (LES), or even Direct Numerical Simulation (DNS) due to their capacity to provide resolved turbulent fluctuations. However LES is computationally too expensive for industry application while DNS is further restricted on fundamental flow phenomenon even for academic research due to its even higher cost [32, 51, 60, 65, 75, 76]. In particular for LES, which relies on spatial filtering, simulation result is typically grid dependent and sufficient mesh resolution is required [64]. Starting from a grid already adequate for RANS, the marginal benefit to increase the

## **1.1. Challenges of numerical study of turbulent in-cylinder flow**

---

resolution is quite limited until at least the inertial sub-range is directly resolved.

Trying to combine the best of LES and RANS, Hybrid models [26] resolve part of the flow scales where possible and model all of them elsewhere. Consequently, hybrid RANS/LES adopts “coarse grids” to keep computational efficiency of RANS and take advantage of LES to resolve large flow scales. Initially designed for the simulation of aerospace industry [76], different variants of hybrid models has been proposed and applied on engine flow [2–4, 19, 34, 35]. Experiences gathered from existing studies indicate that the promising of the hybrid concept is attractive but more evaluations on its performance and modelling behaviour are certainly necessary.

Apart from efforts on an cost-effective turbulence method, existence of moving boundaries of IC engine brings another practical issue of dynamic mesh generation: the motion of the piston changes the dimension of the computational grid up to one order of magnitude in one direction; while the periodic open and close of the valve and injector cause more complex change of the mesh connectivity, since switch between boundary and internal face is necessary for related mesh patches. Traditionally dynamic meshing are handled by remapping between several prescribed meshes. However the precision of mesh motion is fixed once the prescribed meshes are provided, so altering the precision requires tremendous extra meshing efforts. Besides, due to the grid-dependent nature of scale resolving simulation, number of the prescribed meshes also increases, since the variation of the cell size must be limited to provide enough grid resolution. An automatic dynamic mesh strategy would certainly reduce the meshing efforts, should it be able to handle mesh topology change run-time during simulation. However resolving the issues concerning the computational efficiency, the enforcement of mass conservation, as well as the compatibility with computation parallelization of an automatic dynamic mesh techniques is unfortunately non-trivial.

The immense quantity of data provided by numerical description of the turbulence flow, being it in agreement with the underlying physics or not, does not lead to an straightforward insight into the cause-effect chain of the engine CCV. The existence of coherent motion could be helpful to establish a low-dimensional description of the multi-dimensional, time-varying engine flow. However, an objective criterion to quantify the importance of different turbulence structures is necessary to decompose and

reorganize the hierarchy the flow information, so that controlling factors of cyclic variation could be possibly understood and isolated.

### 1.2 Objective, approach and structure of the thesis

---

The objective of this work is the development of cost-effective numerical methods to study in-cylinder flow, with special interest on the description of its turbulence unsteadiness, which includes:

- A cost-effective, scale-resolving turbulence method with a smooth marginal benefit curve in terms of grid resolution.

The hybrid RANS/LES model dynamic length-scale resolution (DLRM) [63] is further developed with respect to the definition of resolvable length scale. Basically the spatial and temporal resolutions are treated separately. The former one is defined as a reference to the lowest resolvable length scale allowed by local grid step size according to Nyquist criterion, while the later one borrows the concept of *CFL* number so that local resolvable time scales could be treated with a corresponding length scale. Such definition allows better differentiation between spatial and temporal resolution, robust damping/filtering behaviour and much better adaptivity to coarse mesh and large time step. Validation of the turbulence model is performed on an optical engine with detailed multi-cycle experimental measurement. Generic implementation of the hybrid model is finished within the environment of the open sourced C++ library OpenFOAM<sup>®</sup>, and the hybridization between arbitrary RANS and LES filtering shape is straightforward.

- A dynamic mesh strategy to handle the topology change automatically, which is compatible with computation parallelization and the aforementioned turbulence method.

Both generic techniques and case-specific methods are developed and validated so that the moving boundaries of IC engine are handled automatically with sufficient numerical accuracy.

Generic techniques are developed for the motion law of the piston and the run-time topology changes, including layer addition/removal (A/R) and mesh interfacing.

Motion law of the piston/valve are tracked either through curve fitting with user-provided Fourier series coefficient, or a map of the lift profile of sufficient accuracy.

Automatic layer A/R tracks the motion of the piston while keeps the mesh resolution (hence the “filter” size in the context of LES) almost unchanged through the entire engine cycle. Mesh interfacing are performed through either `sliding interface` or `arbitrarily coupled mesh interface` (ACMI). While ACMI is already available from OpenFOAM® [78] by the fork maintained by OpenFOAM Foundation, the COUPLING/DECOUPLING mechanism of the `sliding interface` has to be optimized so that renumbering of the grid points is avoided when it is not necessary.

All the generic techniques are implemented to be compatible with the polymorphism of the dynamic mesh library of OpenFOAM®, so that only the necessary topology changes during the simulation are constructed run-time as required by the user.

Case-specific character of the moving boundary problem is treated by run-time boundary condition, so that the polymorphism of the code structure is kept intact and the abstraction overhead from generic programming could be avoided. To keep the compactness and the generic nature of both the solver and the necessary library for dynamic mesh handing, the run-time boundary condition is fulfilled by the `function Object` techniques of OpenFOAM® and its entire behaviour and potential negative side effect are contained within the specific case set-ups.

- A post-processing guideline to identify coherent structures, as an attempt to describe turbulence engine flow objectively and intuitively.

To lower the dimension of the dynamic turbulent system, flow decomposition by means of proper orthogonal decomposition (POD) is applied to the time and cycle dependent flow field. Along with standard statistics such as the ensemble-averaged mean value or the variance, which are used to validate the performance of the proposed simulation methods, POD helps to identify the most important (energy containing) flow structures with mathematically well-defined criterion.

Further development based on the parallelized model reduction library `modred` [10] is carried on so that the modal decomposition directly deals with the vector field and the inner product of the “vector” in the POD domain are more consistent with the kinetic energy of the flow field in the physical domain.

In the following part of the thesis, first the turbulence methods applicable to in-cylinder flow are discussed, with an brief review of the scale resolving engine simulations. Then the detailed formation of the hybrid model DLRM is given and its theoretical filtering behaviour is discussed. Chapter 4 focuses on the dynamic mesh strategies, while validation of the proposed methods is given in chapter 5, in which simulation results with different turbulence methods are compared against experimental measurement. Chapter 6 includes the POD analysis on the engine flow under investigation in the validation chapter. The thesis is concluded in the final chapter.



---

# CHAPTER 2

---

## Turbulence method

---

### 2.1 Turbulence scales and their modelling

---

#### 2.1.1 Range of turbulence scales in engine flow

In-cylinder charge motion is three-dimensional, time-dependent and includes a wide spectrum of turbulent length and time scales. Largest turbulent structures usually have length scales ( $\mathcal{L}$ ) comparable to the macroscopic geometry of the engine, they carry most of the fluctuation energy which is transferred successively to smaller and smaller scales. The smallest structures of the interest of fluid dynamics are usually termed as Kolmogorov scales [40], where molecular viscosity takes over and inertial force is negligible. Mathematically the entire range of flow scales, from the largest ones to Kolmogorov scales, could be described by Navier-Stokes (NS) equations. Unfortunately, a numerical solution of the NS equation of engine flow is huge due to the range of the length scale being typically in the order of  $1000^3$  to  $10000^3$  depending on the

Reynolds number ( $Re$ ). In the near wall region the resolving efforts are further elevated, since the Kolmogorov scale tends even lower due to the higher shear rate and flow anisotropy [64]. As a consequence, a DNS of the entire turbulence range of the engine flow requires prohibitively high mesh resolution, which is computationally too expensive at least in the near future.

### 2.1.2 Scale separation and turbulence modelling

For practical simulation of the engine flow, the range of resolved turbulence scales must be reduced. Hence the unknown information of the unresolved scales has to be estimated by a turbulence model, which assumes some connections between the resolved and unresolved part of scales based on statistics of similar flow problems. Although an universally valid relation has not yet been found, and “backscatter” of the energy from small eddies to larger ones does exist, most of the popular turbulence models adopt the assumption of eddy-viscosity: Different turbulence scales have distinct characteristic behaviours, as the larger eddies are anisotropic, geometry-bounded and contain most of the turbulence kinetic energy, whereas sufficient smaller eddies are isotropic, uniform, and mainly serve as the inter-media to drain energy from large eddies. If such separation of scales is valid, the overall effect of unresolved scales is dissipative and could be described as additional viscous effect onto the resolved ones. To further simplify the problem, Boussinesq assumption could be applied [14], so that the eddy-viscosity force is locally aligned with the strain rate of the resolved flow. Such alignment, or even the concept of scale separation and eddy viscosity, has been recognized as not entirely physically founded through directly post-processing the experiment data or DNS calculation [18, 69]. Nevertheless, its superior advantage on numerical stability and feasibility of implementation are favoured by most of the successful modelling methods. Besides, the progress made in affordable computation power boosts the use of increasingly higher mesh resolution, which to some degree mitigate the error brought by the anisotropy of the eddy viscosity.

## 2.2 RANS and LES

---

With a realizable DNS of engine flow being at least decades away for general purpose CFD study, the concepts of RANS and LES might currently be the most successful modelling methods. RANS has already been established as the standard tool for R & D of automobile, while LES is generally regarded as the next generation practice of turbulence modelling for several industries [69].

The underline concepts of them are quite distinct from each other in the physical point of view. RANS focuses on only time (phase) averaged quantities, and the turbulence behaviour is enclosed within appropriate turbulence model that takes into account all turbulence scales. The advantage is that the modelled length and time scales are estimated from (ideally) grid-independent parameters, so that transport equations can be solved on reasonably coarse grids. Over the years different variants of RANS methods have been developed and some of them gain great success on the predictions of the mean flow and the wall shear stress. The disadvantage of RANS is simply that the small unsteady motions have to be smoothed out, since only mean flow is transported on the computational grids.

LES, on the other hand, intends to model only small turbulence scales, while keep the large scale turbulent fluctuation in the equation. This is somehow a straight-forward choice, since smaller eddies contain less kinetic energy and are more expensive to resolve but easier to be modelled into some forms of dissipative effect. The low-pass treatment of the scale frequencies are usually termed as “filter” operation in the context of LES, although only a few LES models adopt explicit filtering on the flow field.

The concept of low-pass filtering seems very promising, and simulation practices confirm that it does provide better predictions on turbulent fluctuations [7, 49, 55, 57]. However, these practices also indicate that a realistic LES requires at least one order of magnitude higher grid resolution compared with RANS. Further to that, even more computational expense must be paid to properly resolve the near wall effect, since it scales with  $Re$  at the same speed as in DNS [32, 51, 60, 64, 65, 75, 76]. The reason typically lies in the eddy viscosity assumption: Denser grid provides more resolution so that a wider range of length scales are resolved and non-linear interactions are more

likely to occur, whereas linear assumption is still used in most of the LES models, so one is forced to provide even more grid resolution to limit the error [69]. Different criteria of mesh resolution have been proposed for the “completeness” of LES [64, 65], e.g. 80 % of the turbulent kinetic energy (TKE) or the “inertial sub-range” must be resolved everywhere. Unfortunately none of the criteria promotes mesh resolutions comparable to RANS.

Despite the different physical nature, if one focus on turbulence models based on Boussinesq assumption, being it applied on a RANS or LES variant, the effects of unresolved (modelled) flow scales on the resolved (transported) ones are described by the turbulence viscous force, with formally identical model equations [69, 70]:

$$\tau_{ij}|_{RANS} - \frac{1}{3}\tau_{kk}|_{RANS}\delta_{ij} = -2\bar{\rho}\nu_t|_{RANS} \left( \bar{S}_{ij} - \frac{1}{3}\bar{S}_{kk}\delta_{ij} \right) \quad (2.1)$$

$$\tau_{ij}|_{LES} - \frac{1}{3}\tau_{kk}|_{LES}\delta_{ij} = -2\hat{\rho}\nu_t|_{LES} \left( \hat{S}_{ij} - \frac{1}{3}\hat{S}_{kk}\delta_{ij} \right) \quad (2.2)$$

Where  $S_{ij}$  is the strain rate of the resolved flow field. The overbar “ $\bar{\phi}$ ” stands for the Reynolds average operation, and the “ $\hat{\phi}$ ” hat stands for spatial filtering. In both cases, turbulence viscosity  $\nu_t$  is unknown, and it is assumed to be proportional to the modelled length scale and a corresponding velocity scale, according to dimensional study:

$$\nu_t \propto \ell_m \cdot u_m \quad (2.3)$$

It is the constitution of the  $\ell_m$  and  $u_m$  defines their different model behaviours, as RANS resorts to (ideally) physical, grid-independent parameters whereas LES relies on local grid so that spatial filtering is performed implicitly through  $\nu_t$  [26].

### 2.3 Promising of Hybrid RANS/LES

---

The low cost of RANS and resolving capability of LES motivate the combination of these two approaches: To perform LES where it is needed while using RANS in regions where LES is too expensive or unnecessary [26]. Several hybrid LES/RANS methods have been proposed and applied to study of engine flow. To the author’s opinion they

could be grouped into two categories: zonal method and non-zonal method.

### 2.3.1 Zonal method

Detached-Eddy Simulation (DES) [19, 76] proposed by Spalart *et al.* might be the first successful hybrid model. Initially DES is designed for the LES of flow field around wing, it is motivated by the high computational cost to resolve the near wall turbulent effect, since the Re in aerospace application is in the order of  $10^6$  (much higher than that in engine flow). DES proposes to use RANS within the boundary layer for “attached eddies”, and switch to LES after massive separation for “detached eddies” which are “cheaper” to be resolved compared with “attached eddies”. As other forms of zonal hybrid models, DES has two distinct zones that work under either RANS or LES, and they are interfaced by either just zone boundaries or “grey area” [33] region. The same concept is also adopted in hybrid models like Delayed Detached-Eddy Simulation (DDES) [83], RANS-limited LES [15], and Limited Numerical Scales (LNS) [5, 6]. For engine flow, the ability of DES to predict scale-resolved in-cylinder flow has been exploited by Hasse *et al.* in their numerical study of engine CCV [34, 35].

### 2.3.2 Non-zonal method

As an alternative to switching between LES and RANS depending on the wall distance or local mesh resolution, hybrid models using uniform model equations have also been developed. This is partially motivated by the difficulties to address the “grey area” of zonal approaches. Hybrid between the RANS and LES usually is performed through damping the turbulence viscous stress provided by a parent RANS model, since a direct blending tends to generate unphysical flow structures [1, 74]. Partially Averaged Navier-Stokes (PANS) [27], for example, damps turbulent viscosity by decreasing the destruction term of the dissipation rate of TKE, its performance for simulation of engine flow is analyzed by Basara *et al.* [2, 3].

One of the benefits of non-zonal method is the “smooth” transition between RANS and LES, as the same hybrid NS equation is used for the entire simulation domain. However, this brings a issue of consistency, which is not so obvious, that the RANS variables would lose its time (phase) averaged nature, and a undesirable “double damp-

ing” is applied on the turbulence viscosity. The reason is that only part of the TKE is left unresolved in the modelled scales, this automatically decreases the turbulence viscosity estimated by the parent RANS model. Without a proper correction, this turbulence viscosity is assumed as the comprehensive one, which would be further reduced by the damping factor. For ensemble averaged steady state problem the consistent issue could be solved by run-time averaging the solution of previous time steps, for complex problems like engine flow, either a reference RANS case has to be performed simultaneously, or the RANS variables have to be estimated from the partially resolved flow fields.

### 2.4 Scale resolving simulation of engine flows

---

RANS is currently still the state of the art turbulence method of engine simulation for industry application. For academic research, practical scale resolving studies of the engine flow are performed by means of either (fully resolved) LES or more recently, hybrid RANS/LES.

It is generally accepted that LES captures better CCV than RANS-based phase averaged mean computations [21, 29]. A necessary and common practice for LES, or more generally for any scale resolving simulation is that multiple engine cycles are calculated for statistical converged realizations of the cycle-dependent flow fields. Earlier LES applications are typically based on original Smagorinsky model [73] and wall functions derived from RANS, and the number of engine cycles calculated have to be limited [36]. Progress made in the recent years on both turbulence model and affordable high performance computation promotes adoptions of more sophisticated sub-grid scale (SGS) models [8, 17, 57] and perhaps more importantly much refined computational grids [7, 67], with more engine cycles been calculated [28]. Rutland’s recent review [69] discusses the most important challenges of SGS model critically, including sub models not only for the transport of momentum, but also on the transport of mass & heat, as well as the coupling with chemical kinetics. All those studies confirm the capability or more conservatively the potential of LES as an important computational approach to understand the unsteadiness nature of cyclic varying in-cylinder flow. However, apart from the prohibitively high computational cost, it is also recognized that an

conventional “fully-resolved” LES is much more sensitive to boundary conditions and requires high order numerical schemes, which are typically quite difficult to be applied on complex unstructured grid. Besides, if direct resolving the near wall region has to be avoided, a wall model that consistent with the spatial filter concept of LES is also much needed to shield the resolved free shear region from the ensemble-average nature of wall functions developed for RANS.

An attempt to overcome the disadvantage of both RANS and LES is the implementation of hybrid RANS/LES. Success of the LES for free shear flow and the high cost of resolving near wall region inspire the concept of Detached-Eddy Simulation (DES), which treats near wall region with RANS and applies LES where the sub-grid scales are free from the influence of wall distance. Concept of DES is shared and further developed by a range of hybrid models, including DES with  $k - \omega$  model [82], DES with  $k - \epsilon$  model, and delayed DES (DDES) [71]. Strategies other than a split description of flow region favour a unified turbulence equation, examples are flow simulation methodology (FSM) [77] or partially-averaged Navier-Stokes (PANS).

Examples of hybrid RANS/LES application on engine flow are limited though. A few examples include the DES study on the engine CCV by Hasse *et al.*, on both a simplified engine set-up [12, 34] and motored production SI-engine [35] and a few performance studies on the feasibility of applying PANS to complex problems including engine related flow [4, 31]. Although these studies suggested that hybrid models are potentially the most cost-effective tool for engine simulation at least in the near future [33], a general best practice is not established due to the complex flow phenomena involved in the in-cylinder turbulence evolution. Deeper and wider investigation in terms of model formulation, near wall treatment, numerical schemes, quality access, and even post-processing are necessary for better evaluation and feasibility analysis of applying hybrid RANS/LES on engine flow.





---

# CHAPTER 3

---

## Dynamic length-scale resolution model

---

The hybrid model adopted in this work is the latest development of Dynamic Length Scale Resolution Model (DLRM) [63] for the scale-resolving simulation of engine flow. The non-zonal hybrid strategy is followed by DLRM, so that the efforts for a physical description of the “grey area” involved in the zonal method could be avoided. The entire flow field is transported by an unified hybrid NS equation apart from the first layer near the wall, where necessary wall model inherited from the parent RANS is applied. Besides, due to the existence of periodic high speed jet flow generated by the open of engine valve, resolving the free shear region with a conventional SGS model is also quite expensive compared with RANS. In this case a zonal method would either switch to LES outside the wall region where the grid resolution is actually insufficient, if a “hard interface” [26] is defined; or recover back to pure RANS mode everywhere which abuse the potential resolving capability of the grid, should a “soft interface” being adopted.

DLRM performs the damping or “rescaling” on the turbulence viscosity of RANS through comparing of the local reference turbulence length scales and numerical resolution (resolvable length scales). Original studies on steady state engine flow and wind turbine [54, 63] indicate that DLRM has great potential to reduce the computational cost of conventional LES. Further development of the model would be discussed in this paper, along with the validation of its performance in moving boundary problem.

### 3.1 Formulation of length scales

---

One important object of a hybrid turbulence model is to distinguish between resolvable and non-resolvable scales, so that an objective criterion of how “resolvable” is the numerical set-up could be established to control the hybridization between RANS and LES. Characteristic grid resolution ( $\Delta_{mesh}$ ), or more generally the local resolvable length scale ( $\ell_t$ ) is an common measurement to give general ideas about the numerical resolution of the simulation. However, flow conditions inside engine cylinder varies greatly in both space and time,  $\ell_t$  alone as a criterion could not respect the local turbulence level since a universal characteristic turbulence length scale is not available for engine flow. As a local reference scale has to be provided to represent the turbulence level, DLRM uses the integral turbulent length scale ( $L_t$ ) so that comparison between  $\ell_t$  and  $L_t$  yields better measurement of local numerical resolution.

Considering a two-equation RANS model based on Boussinesq assumptions, where the definition of turbulence kinetic energy ( $k$ ) and its dissipation rate ( $\epsilon$ ) are available or at least could be calculated with minor effort. Evaluation of the  $L_t$  and velocity scale ( $u_m|_{RANS}$  as defined in Eq. 2.3) is straightforward:

$$\begin{aligned} L_t &= \ell_m|_{RANS} = k^{3/2}\epsilon^{-1} \\ u_m|_{RANS} &= k^{1/2} \end{aligned} \tag{3.1}$$

As the parent RANS model takes care of the calculation of  $L_t$ , formulation of  $\ell_t$  is specified by DLRM, considering both spatial and temporal resolution.

For spatial resolution, one obvious connection should be linked to the local mesh resolution  $\Delta_{mesh}$ :

$$\Delta_{\text{spatial}} = \beta \Delta_{\text{mesh}} \quad (3.2)$$

Where  $\beta$  is the number of grid points(cells) needed to properly resolve a flow length scale. On Cartesian grids  $\beta$  should be no smaller than 2 to satisfy Nyquist criterion. The study by Gyllenram and Nilsson indicates that a value of  $\beta \leq 3$  is necessary to obtain accurate results [31]. In DLRM, value of  $\beta$ , alone with the formulation of  $\Delta_{\text{mesh}}$  is up to user’s choice. In the simulation part of this work, a constant value of 5 is used for  $\beta$  while the cubic root rule is applied for  $\Delta_{\text{mesh}}$ .

As for the temporal resolution, the concept of  $CFL$  number is used and  $|\mathbf{U}|\delta t$  is regarded as the smallest local resolvable length scale allowed by time step, where  $|\mathbf{U}|$  is the norm of velocity being transported on local grid, and  $\delta t$  is the time step. In fact  $|\mathbf{U}|\delta t$  is the shortest distance over which a fluid particle can be traced in an unsteady computation, and Batten *et al.* commented that a in theory a steady RANS calculation should correspond to an infinite time step, for which  $\ell_t = L_t$

Combine both spatial and temporal resolution, final formulation of  $\ell_t$  is defined as

$$\begin{aligned} \ell_t &= \gamma \max(\Delta_{\text{temporal}}, \Delta_{\text{spatial}}) \\ &= \gamma \max(|\mathbf{U}|\delta t, \beta \Delta_{\text{mesh}}) \end{aligned} \quad (3.3)$$

Where  $\gamma$  is a safe factor and it is found that a constant value of 3 is enough. For flow regions where numerical resolution is not high enough to resolve even the integral length scales,  $\ell_t$  is limited to  $L_t$  to make sure that  $\alpha$  is bounded by unity.

### 3.2 “Filtering” behaviour

---

Let’s go back a little bit to a more general concept of non-zonal hybrid model, where  $\nu_t|_{RANS}$  is damped based on the observation that it is typically much stronger than  $\nu_t|_{LES}$ , since  $\nu_t|_{RANS}$  intends to smooth out all turbulent fluctuations. A hybrid turbulence viscosity could then be defined as:

$$\nu_t|_{\text{hybrid}} = \alpha \nu_t|_{RANS} \quad (3.4)$$

$\alpha$  is called the damping factor or damping function and the quantification of its value defines the hybridization of the turbulence model. Following the approach proposed by Willems [85] and developed by Gyllenram [31], DLRM computes  $\alpha$  by comparing the integral length scale estimated by RANS( $L_t$ ) and the smallest resolvable length scale defined in LES ( $\ell_t$ ).

As defined in Eq. (2.3), turbulence viscosity is proportional to the characteristic length and velocity scale. Since  $L_t$  stands for the modelled length scale of RANS, there is:

$$\nu_t|_{RANS} \propto L_t \cdot u_m|_{RANS} \quad (3.5)$$

Combine Eq. 3.5 and 2.3 yields

$$\begin{aligned} \nu_t|_{RANS} &\propto L_t \cdot (L_t \epsilon)^{1/3} \\ &\propto L_t^{4/3} \cdot \epsilon^{1/3} \end{aligned} \quad (3.6)$$

Assuming that the shape of Eq. (3.6) stays unchanged for a hybrid model where  $\hat{k}$  also provides the velocity scale for the  $\hat{u}_m$ , with a characteristic dissipation rate of  $\hat{\epsilon}$ , Eq. (2.3) of the hybrid model then takes the same formulation of RANS:

$$\nu_t|_{hybrid} \propto \ell_t^{4/3} \cdot \sqrt[3]{\hat{\epsilon}} \quad (3.7)$$

Since  $\epsilon$  takes actions on Kolmogorov scale which practically is almost never the interest of a hybrid model, one further assumption is that  $\epsilon$  estimated by RANS is regarded accurate enough so that:

$$\hat{\epsilon} = \epsilon \quad (3.8)$$

Thus Eq. (3.6), (3.7), and (3.8) link  $\nu_t$  with the characteristic length scales locally used by different turbulence models, in this case  $L_t$  and  $\ell_t$ , and the damping function  $\alpha$  in DLRM is thus defined as:

$$\begin{aligned}\alpha &= \frac{\nu_t|_{hybrid}}{\nu_t|_{RANS}} \\ &= (\ell_t/L_t)^{4/3}\end{aligned}\quad (3.9)$$

The hybridization between RANS and LES in Eq. (3.9) is that as RANS provides grid-independent information such as the turbulence kinetic energy and the integral length scale, a grid-dependent length scale  $\ell_t$  is used to damp or “filter”  $\nu_t|_{RANS}$  so that local resolvable flow structures are not smoothed out by RANS.

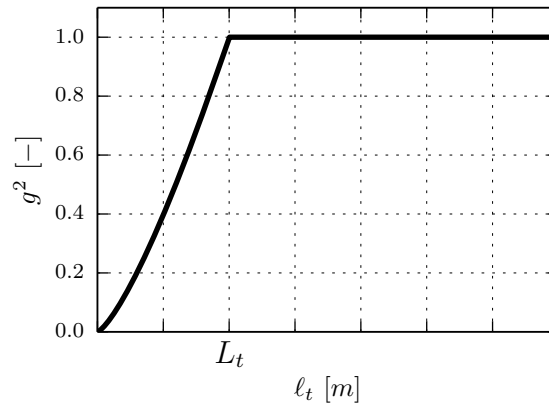


**Figure 3.1:** The damping factor  $g^2$  as a function of smallest resolvable length scale  $\ell_t$  and turbulence integral length scale  $L_t$

For a better indication that the damping factor always takes a positive value, as shown in Fig. 3.1, an equivalent function  $g$  is defined as:

$$g^2 \equiv \alpha = (\ell_t/L_t)^{4/3}\quad (3.10)$$

And the damping function would also be referred as “ $g^2$ ” from then on. It is straightforward that  $g^2$  tends to 0 in the fine limit of the grid (and time step) resolution, as

$$\left. \frac{\partial (g^2)}{\partial \ell_t} \right|_{\ell_t \rightarrow 0} = \frac{4}{3} \left( \frac{\ell_t}{L_t} \right)^{1/3} \Big|_{\ell_t \rightarrow 0} \rightarrow 0\quad (3.11)$$

Another behaviour inherited from RANS is a positive second order dependency of  $\nu_t$  on the turbulence length scale:

$$\left. \frac{\partial^2 (g^2)}{\partial \ell_t^2} \right|_{\ell_t \rightarrow 0} = \frac{4}{9} \left( \frac{\ell_t}{L_t} \right)^{-2/3} \Big|_{\ell_t \rightarrow 0} \geq 0 \quad (3.12)$$

Which allows an correct formulation of the damped turbulence viscosity since increase of  $\ell_t$  in its coarse limit corresponds to faster recovery to its standard RANS behaviour.

One clear advantage of Eq. (3.10) is that should  $L_t$  being correctly estimated by the parent RANS model,  $g^2$  provides an (ideally) objective measurement of the numerical resolution with respect to the flow field been simulated. An lower value of  $g^2$  is a direct indication that a larger portion of the flow scales are resolved rather than modelled. In an extreme case when  $g^2$  tends to 0, DLRM works as an implicit LES whose SGS treatment relies on the numerical diffusion. On the other hand, should the local resolvable length scale is greater than (limited to) the integral length scale, DLRM recovers to standard RANS and only (ensemble) mean flow is transported.

---

# CHAPTER 4

---

## Dynamic mesh strategy

---

### 4.1 Moving boundaries of IC engine

---

Automobile IC engine uses the reciprocating motion of the piston to convert heat into the mechanical energy onto the rotation crankshaft, and the respiration of the engine charge is controlled by the lift motion of engine valve (guillotine). Compared with the rotatory design of aircraft engine, the reciprocating cycle allows for higher combustion temperature and better adaptivity to variable working conditions. This unfortunately brings difficulties for engine simulation, as the dynamic mesh is necessary to properly track the motion of all the moving boundaries. As a simple stretch, or relocation of the grid points could not describe the grid dynamics with appropriate quality, connectivity, or sometimes terms as “topology” of the mesh has to be changed during the simulation. The topology change could be grouped into two categories, namely Layer Addition/Removal (A/R) and mesh interfacing [56].

### 4.2 Layer A/R

---

Layer A/R is necessary due to the variation of the geometric volume of the flow domain, hence also the computational grid. Change of the volume of the combustion chamber is an obvious example as shown in Fig. 4.1: Commercial IC engine has a typical compression ratio around 10:1, this is achieved through the motion of the piston in only one direction ( $z$  in Fig. 4.1) between the top dead center (TDC) and bottom dead center (BDC). Considering that most of the clearance volume is provided by the pent roof (or the bowl of piston in diesel engine), the ratio ( $R_\Delta$ ) of the grid step sizes  $\Delta_{mesh}$  at different engine times could vary up to 40 times depending on the specific engine design, if the topology of the mesh is kept unchanged during the entire engine cycle. This is obviously not favoured by any scale resolving simulation, as the lower limit of the filter size depends explicitly on  $\Delta_{mesh}$ . Even in an extreme case that the computational expense is not of concern and grid resolution is forced to be sufficient enough even at BDC, the aspect ratio is still in the order of  $\sqrt{R_\Delta}$  for a considerably large portion of the grid cells in the cylinder.

One solution to balance the resolution is to prepare multiple predefined grids for different crank angles (CAs), and remap between them runtime during simulation. Remapping provides user defined grid distribution so that the quality is maintained [48], however, as already briefed in the introduction chapter, the extra meshing efforts could be huge. Considering a typical gasoline engine today has a stroke around 100 mm, and we assume that a characteristic  $\Delta_{mesh}$  between 2 to 3 mm is already sufficient for scale resolving simulation, which is rather optimistic even for cold flow without combustion [7, 33, 57]. Nevertheless, this suggests that at least 30 grids have to be provided, even for a close cycle simulation without the motion of valve. One might argue that once the first grid is finished it takes minor efforts to generate the rest of them, but this is at least over optimistic in author's experience: Grid dependency check is common practice for scale resolving simulation, so any change of the initial grid resolution requires re-meshing the entire series of grids.

Automatic layer A/R would be a win-win solution since it avoids re-meshing effort while at the same time maintain an user defined grid resolution. The dynamic mesh



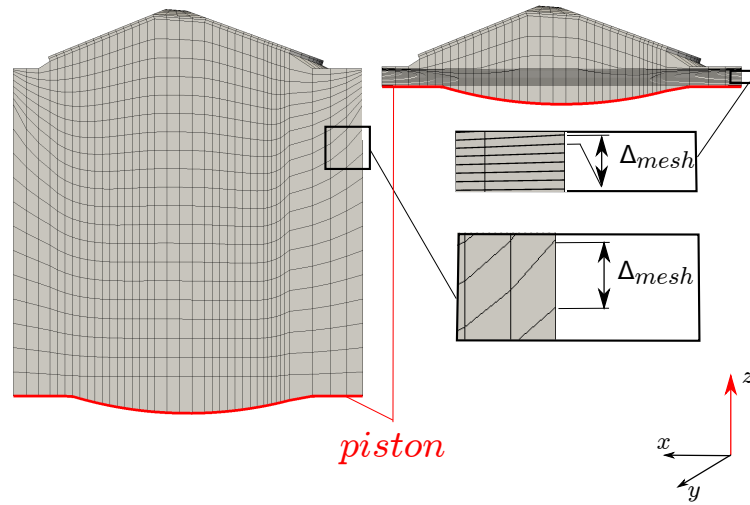


**Figure 4.1:** Change of grid size  $\Delta_{mesh}$  due to volumetric variation of the combustion chamber. (Left: BDC, right: TDC)

strategy developed by Montorfano *et al.* [56] at ICE Group of Politecnico di Milano is adopted in this study. As shown in Fig. 4.2,  $\Delta_{mesh}$  of the entire mesh domain is kept unchanged during the mesh motion, except for one layer of the mesh where the points are stretched according to the prescribed piston motion law. Layer A/R is triggered if the thickness of this layer grows above or decreases under a certain value specified by the user. The major advantages of this dynamic mesh strategy are:

- Grid resolution is practically decoupled from the piston motion, as only small variation of  $\Delta_{mesh}$  has to be performed on only one mesh layer, and
- Location of this layer is specified by the user so that it could be put away from the wall to preserve the mesh quality of the boundary layer.
- Much less meshing efforts compared with mesh remapping

### 4.3 Dynamic mesh interfacing

Lift of the valve or injector requires more numerical considerations compared with piston motion. Not only the volume would change during the valve motion, but part of the grid patches also has to be switched between internal and boundary faces during the lift motion. Fig. 4.3 shows an simplified guillotine (valve) lifting along with the moving piston, without considering the volume change of different mesh structures

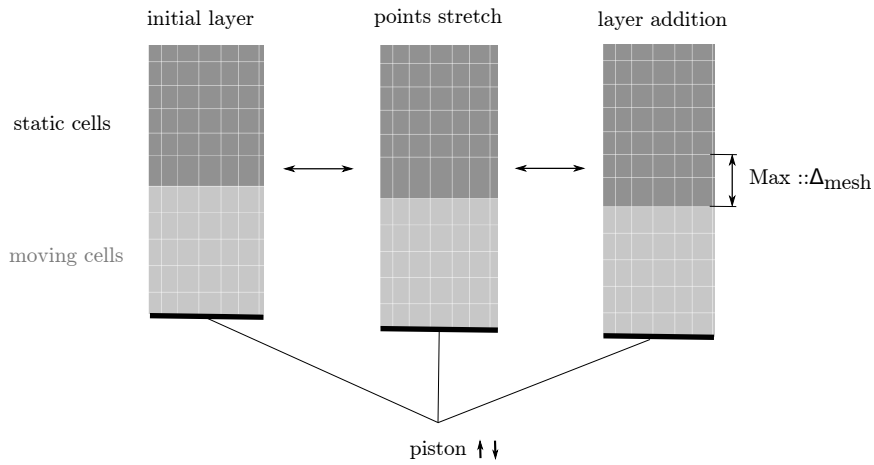


**Figure 4.2:** Automatic grid layer A/R

typically involved in simulation of 4-stroke engines [56]. Connectivity of different mesh regions, shown by different colors in sub figure (a), (b), (c) in Fig. 4.3, is changed due to the switch of the roles of mesh patches around the engine guillotine. The required dynamic mesh interfacing could be obtained through two numerical methods, namely sliding interface and Arbitrarily Coupled Mesh Interface (ACMI).

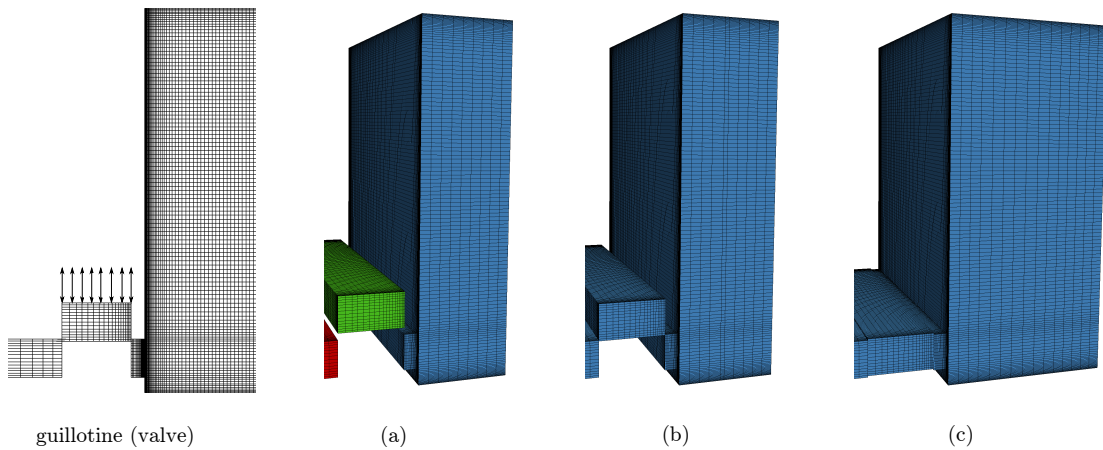


**Figure 4.3:** Switch between internal and boundary faces. (a) boundary faces, (b) part of the patches are internal faces, (c) internal faces

### 4.3.1 Sliding interface

Sliding interface is a straight forward way to handle mesh interfacing. The basic concept is that different mesh structures are firstly decoupled from each other, so that the

mesh points of the moving part could then be displaced on to the new location, after the mesh motion the decoupled mesh structures are coupled back again so that flow calculation could be performed. The procedure of the COUPLING/DECOUPLING is performed through points injection, through which the connectivity of between different mesh structures are changed, as shown in Fig. 4.4. Since the original topology of the coupled master and slave sliders are preserved during simulation, the decoupling procedure is performed without any loss of information.

Sliding interface is considered to be a general solution since mesh motion is decoupled from flow calculation, this in theory could provide a more diagonal dominated matrix for flow calculation so that the impact of mesh motion on the convergence of the simulation is minimized. However, COUPLING/DECOUPLING procedure is computationally expensive. Since the patches are changed from boundary to internal faces and vice versa, renumbering of the grid faces has to be performed twice during one time step. Besides, the complicated topology information preserved during flow calculation limits the execution of COUPLING/DECOUPLING applicable on only single computer processor, since parallelization brings considerable communication overhead.

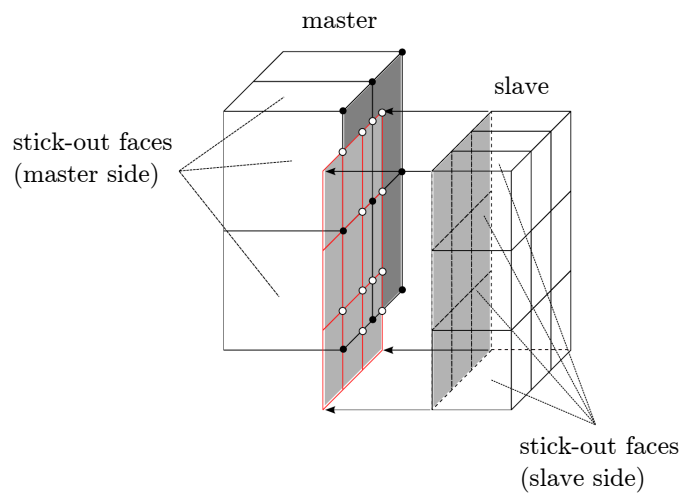


**Figure 4.4:** Sliding interface, point projection of slave patch (red) onto master patch. Solid dots are master points (which are retained), hollow circles are slave points added due to direct hits or intersections. (Figure taken from [56])

### 4.3.2 ACMI

ACMI [22, 56], or sometimes termed as generalized grid interface (GGI) [9] aims to provide a faster and more parallelization friendly interfacing method than sliding interface. The difference is that the patches involved the interfacing procedure are always treated as boundary faces, so that the renumbering of the mesh faces is avoided, which is the major bottle neck for the speed up of sliding interface. Besides, since the topology of the mesh is not changed, parallelization is also much more straight forward.

Since the interfaced patches are always regarded as boundary faces, interpolation of the flow rate are necessary when the physical flow domain are actually connected with each other. Interpolation is based on the weighted factor of the coverage area between neighbouring patches. Details of how the weighted factor is calculated could be found in original works of Beaudoin [9] and Farrell [22]

Despite its much improved computational efficiency compared with sliding interface, ACMI does have one potential drawback in terms of mesh quality. Since the related patches are always treated as boundary even when the interfaced mesh structures are connected, explicit interpolation is necessary, and this leads to less diagonal dominated matrix for flow calculation. However, due to the necessity of parallel computing, such drawback became somehow tolerable, since parallelization is typically based on mesh decomposition, in which explicit interpolation between different processors could not be avoided, regardless of the mesh interfacing method.

## 4.4 Mass conservation

---

Movement of the grid points in the direction not normal or tangential to the grid faces would generate artificial source term of mass, which violates the conservation law with a first order continuity error proportional to time step [24]. Practically this is not an issue for the simulations in this study, since both the piston and the valve moves in one direction. Nevertheless, to make the dynamic mesh strategy more general, enforcement of the mass conservation should also be considered.

Correction of the artificial mass is performed so that space conservation law (SCL) is satisfied [30, 56, 79]:

$$\frac{d}{dt} \int_V dV - \int_S \mathbf{v}_b \cdot \mathbf{n} dS = 0 \quad (4.1)$$

Where  $dV$  is change of the control volume of the grid cell,  $\mathbf{v}_b$  is the moving patch velocity.

In discretized form, Eq. 4.1 reads:

$$\frac{(\Delta V)^{n+1} - (\Delta V)^n}{\Delta t} = \sum_c (\mathbf{v}_b \cdot \mathbf{n})_c S_c \quad (4.2)$$

Where  $c$  stands for different faces of the grid cell. Satisfying SCL in the form of Eq. 4.2 is not automatic when the grid points moves in direction not normal or tangential to the grid patch [24], so additional “`meshPhi`” has to be applied according to the volume swept by a cell face  $\mathbf{v}_{sweep}$  within the time step.

Corrections of `meshPhi` without topology change have already been implemented individually for all the available time schemes in OpenFOAM®. However, in case of topology change, namely layer A/R and sliding interface in current study, calculation of  $\mathbf{v}_{sweep}$  is not strait forward, as the mesh faces are renumbered so that their information in the previous time step are lost. Recovery of the information is performed by mapping the field from the old grid points to the new ones, and the way how `meshPhi` is updated depends on the types topology change undergoes:

- Patches that generated through layer A/R
- Patches get deleted
- Patches changes its shape or topology but still maintain its definition

In the first case `meshPhi` is specified to 0 for the new patch, whereas for the last two cases, the remapped velocity field on the new points does not satisfy continuity equation, hence a pressure correction has to be performed so that the velocity field of the old time on the new point is complaint with mass conservation. For incompressible flow, similar to pressure/velocity coupling in segregated solvers:

$$\nabla^2 p_{correction} + \nabla \cdot \mathbf{u}(x^{n+1}, t^n) = 0 \quad (4.3)$$

$$\mathbf{u}_{n+1}^n = \mathbf{u}_n^n - \sum \frac{1}{A_p} \nabla p_{correction} \quad (4.4)$$

Extension of Eq. 4.3 and Eq. 4.4 to compressible conditions is straightforward. It has been noted that for Eq. 4.3, care must be taken on the choices of boundary condition of  $p_{correction}$ , the detail explanation could be found in the original work of Montorfano *et al.* [56].

---

# CHAPTER 5

---

## Validation of the numerical method

---

### 5.1 Test case

---

The validation of the proposed approach has been carried out on the experimental set-up of Boreé et al. [12, 13], who did comprehensive study of the evolution of tumbling motion in an optical compression machine. The compression machine reproduces engine-like setup with similar engine strokes, and its simplified geometry allows for easier reproducibility of the boundary and initial conditions for simulations and good optical access.

As shown in Fig. 5.1, the compression engine has a squared cylinder (approximately  $100 \times 100 \times 100$  mm at BDC) and a flat piston head. The piston is motored by mechanics typically adopted by filling machine at 206 rpm, and a quasi-sinusoidal motion is expected. The volumetric compression ratio ( $r$ ) of the engine is about 4, with the engine stroke around 75 mm and the head clearance at TDC around 25 mm. Actual value of  $r$  in the experiments differs from the geometric one, for that air leakage is

inevitable between the cylinder and piston ring. An intake (outlet) channel is used for the aspiration of engine charge. The length of the channel is 30 times of its width, so that well developed turbulence flow is expected at the inlet of the cylinder during intake stroke, where the bi-dimensional jet flow, tangential to the cylinder floor, is deflected by the moving piston and generates the tumbling vortex. The intake channel is connected by a plenum with sufficient large volume to damp the pressure fluctuation, the plenum also provides a seeding pool for particle image velocimetry (PIV) measurement.

Different engine strokes are defined through open/close of a guillotine (engine valve) device (Fig. 5.1). During the experiment, two operating modes were tested:

- (a) The so-called “**uncompressed-vortex**” case, with the guillotine valve fixed during the piston motion and the inlet channel fully opens, the engine cycle includes an intake and an exhaust stroke
- (b) The “**compressed-vortex**” case, with the guillotine open/close according to the reciprocating movement of piston, the engine cycle includes 4 strokes typically operated by automobile IC engine.

Velocity fields are measured on the symmetric x-y plane where the “Laser sheets”(see Fig. 5.1) penetrates the cylinder through optical window. Two dimensional PIV measurements were performed at different crank angles, and more than 100 consecutive cycles are measured at each crank angle for a converged statistical description of the flow field.

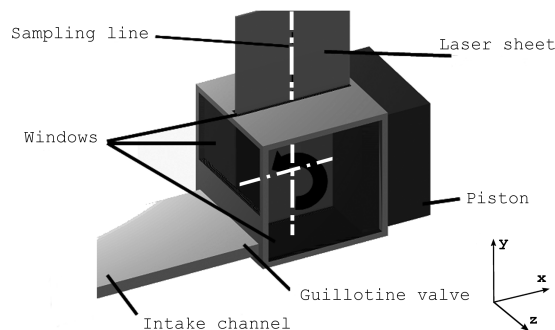


**Figure 5.1:** Experimental setup of the test case. The plenum connected to intake channel is not shown. The laser sheet used for PIV passes through the piston axis.



## 5.2 Numerical set-up

### 5.2.1 Grids

Fig. 5.2 sketches the basic dimensions of the computational domain, which consists of the cylinder, the intake channel and a large plenum. To exploit the computational efficiency of the proposed approach, the “coarse” grid typically used for RANS is adopted for the baseline simulation. Total cell count of the “coarse” grid varies from 0.2 M at TDC to 0.4 M at BDC. For the boundary layer, the first cell centres normal to the wall are placed at  $y_{max}^+ \approx 30$ . For grid-dependency check and a better understanding of the hybrid model’s filtering behaviour, simulations are also performed on a comparably “fine” grid. Total cell count of the fine grid varies from 1 M to 1.8 M, and  $y^+$  at the walls is lower than 3. The author assumes that the resolutions of both grids are sufficient for RANS, however it should be noted that even the fine grid is considered merely adequate for conventional LES with wall modelled rather than resolved, since a resolved near wall treatment requires the refinement on the boundary layer being applied on all three directions [64].

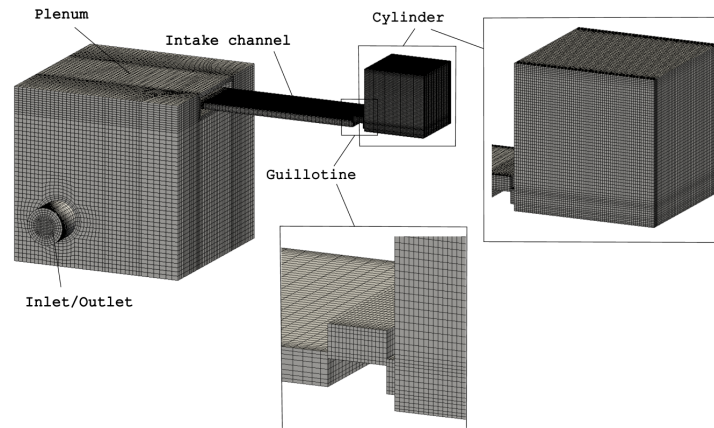


**Figure 5.2:** Finite volume mesh used in the simulations for “compressed-vortex” case.

For the dynamic mesh handling, the motion laws of piston and guillotine are reported in Fig. 5.3. For both “uncompressed-vortex” case and “compressed-vortex” case, the beginning of the intake stroke is set at  $CA = 0^\circ$ , and the end of the consecutive stroke (exhaust stroke for “uncompressed-vortex” case and compression stroke for “compressed-vortex”) is at  $CA = 360^\circ$ . Motion of the piston is accomplished by

run-time layer A/R [56, 62]. Since measurements of the piston motion [12] show small deviations from an ideal sinusoidal one, prescribed motion of the piston in simulation was set by providing measurements as input data. For the lifting of the guillotine (Fig. 5.3-b), both ACMI [22, 23, 78] and `sliding interface` [56] is tested, but no significant difference has been noticed in terms of their impact on the calculation of flow field when the simulation is performed on multiple CPUs. ACMI does have better computational efficiency though, due to the fact that for `sliding interface`, renumbering of the faces has to be conducted twice in one time step if the dynamic grid undergoes topology changes. Calculation of one engine cycle of “uncompressed-vortex” case takes about 4 hours on a Linux Desktop-PC powered by a 8-core Intel-Xeon CPU (E5-2650, 2.30 GHz) and 32 GB RAM, while the “compressed-vortex” case which doubles the number of stokes takes almost exactly twice the CPU wall-time.

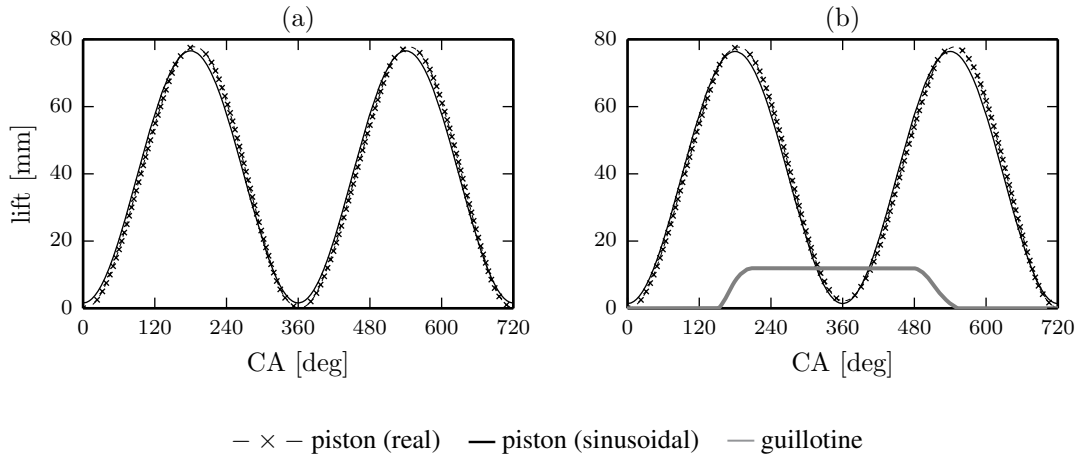


**Figure 5.3:** Piston and guillotine lift: a) “uncompressed-vortex” case (two strokes, engine cycle = 360 CA); b) “compressed-vortex” case (four strokes, engine cycle = 720 CA).

### 5.2.2 Boundary and initial conditions

No-slip boundary condition is applied for all the wall boundaries, except for the inlet (outlet) of the plenum (see Fig. 5.2) and the moving walls. For the inlet, both inflow and outflow can happen, depending on the fluid-dynamic condition of the inner domain. For subsonic inflow to the boundary, the outside total pressure and temperature are prescribed, and velocity vector is specified as normal to the boundary patches. For the out flow, the static pressure is set at the face-centers of the boundary and a zero-gradient

boundary condition is applied on outlet velocity.

More care has to be taken for the boundary conditions of the walls moved with guillotine during “compressed-vortex” case. As shown in Fig. 5.4, wall boundaries marked in red color in Fig. 5.4 have a non-zero tangential velocity whereas the upper walls of the guillotine (in blue color Fig. 5.4) are fixed in the real configuration, so their velocities are zero. In order to enforce a realistic boundary condition on these surfaces, the guillotine velocity was set at run-time on the sliding faces of the moving grid (Fig. 5.4, top): Faces belonging to the blue or red area of Fig. 5.4 are updated at each time step:

- Dirichlet boundary condition  $\vec{u} = 0$  for the blue area in Fig. 5.4);
- Constant value boundary condition for the red area in Fig. 5.4, with the value updated from the motion of the guillotine.

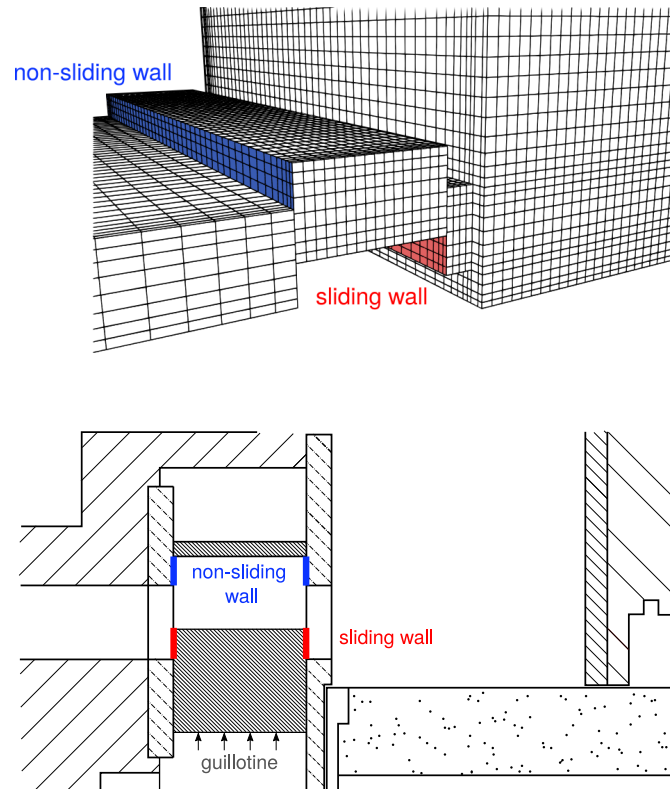


**Figure 5.4:** Boundary condition of moving walls of guillotine: Finite Volume mesh (top); experimental set-up (bottom).

Moreover, the COUPLE/DECOUPLE procedure of the `sliding interface` [62] has

been slightly improved with respect to the first version. The motivation is that COUPLING/DECOUPLING of the sliders are not necessary when the guillotine is not moving, e.g. in the in “fully open” or “fully closed” position. Operation of the sliding interface is deactivated and the interface becomes static. Idling the COUPLING/DECOUPLING procedure allows for a noticeable reduction of the computational cost, for that it is indeed computationally expensive even when no actual topology change is involved, due to the reason explained in the previous chapter.

Wall function is applied on the wall boundaries for all the turbulence variables, namely KTE ( $k$ ) and its specific dissipation rate ( $\omega$ ), as well as turbulence viscosity ( $\nu_t$  or  $\mu_t$ ). Zero-gradient boundary condition is applied for pressure, and the temperature of the wall is specified by the experiment measurement.

To properly initialize the flow field, simulation is performed for 2 consecutive cycles from an uniform values of velocity, pressure, temperature and all the turbulence variables. The simulation results of the last time step of the 2nd cycle are regarded as the initial condition for each case calculated.

### 5.2.3 Solution of NS equation and discretization schemes

The software used for the simulations is based on OpenFOAM<sup>®</sup>, in the development version released by the OpenFOAM Foundation [78], with the necessary extensions for LES turbulence modelling [20, 61] on dynamic meshes [56].

Time-step is adjusted runtime to satisfy the limit of the CFL number and the dynamic layering of the mesh [56]. Since in all cases subsonic compressible conditions apply, pressure-velocity coupling is solved by PIMPLE (merged PISO-SIMPLE) algorithm, the convergence of pressure-velocity is enforced by iterating the coupling procedure for each time-step. Detailed description of the extensions made to solver used and examples of its application to non-conformal dynamic meshes can be found in [56, 62]. It's worth mentioning that even with the maximum CFL number lower than 1, the standard PISO suffers from potential stability issues caused by the fluid compressibility. Although it is quite difficult to identify the underlying reason, one practical work around is to increase the number of outer iteration, in that the momentum equation is solved more than once during one time step.

As for the discretization schemes, time derivative is approximated by second-order backward scheme, and convection of momentum and energy has been discretized by means of Linear-Upwind Stabilized Transport (LUST) [84] for its numerical stability and quasi second order behaviour. Convections of turbulence variables  $k$  and  $\omega$  are discretized by a “limitedLinear” scheme that performs under central difference schemes but limits towards upwind schemes in regions of rapidly changing gradient [78].

### 5.3 Post-processing and Results

---

For a comprehensive validation of the proposed simulation methods, simulations are conducted so that the behaviour of different turbulence models and the dependency on time step and mesh resolution of the proposed hybrid model could be analysed. The baseline simulation is performed on the coarse mesh and adopts DLRM as turbulence model, and the Maximum CFL number is limited to 1. Simulation using conventional LES and RANS are also performed with identical numerical set-ups as the baseline simulation. In particular, “Sigma” sub-grid scale (sgs) model [58, 59] has been used as the reference of conventional LES, being Sigma currently considered one of the best models when applied to LES of Internal Combustion (IC) Engines [8, 41, 49, 53]. RANS is performed by using the well-established  $k$ - $\omega$  SST turbulence model, based on the formulation by Menter [50] with updated coefficients from [52]. Additional simulations using DLRM are also performed by adopting higher CFL number or on the “fine” grid, to study the sensitivity of the proposed numerical method to time-step size and grid resolution. Comparison of the ensemble mean and the variance (Reynolds tensor components) of the resolved velocity field are performed on the global reference frame of the symmetry x-y plane shown in Fig. 5.1, where experimental measurement is available. Flow field is plotted on two sample lines in vertical and horizontal direction for more detailed comparison.

30 consecutive engine cycles are calculated for each case simulated. Although lower than what is available from the experiment, the number of cycles is chosen based on the observation that it could already being used to study the 2nd moment of flow statistics, as the variance of the velocity field could be considered in convergence if more than 25 cycles are sampled, as shown in Fig. 5.5. The DES study of Hasse *et al.* [34] on the

same test case also indicates that even 10 cycles are able to reveal part of information on the cyclic variation of the engine flow. As mentioned before, the first two of the 30 cycles are not sampled for the comparison of phase-averaged quantities, since they served to initialize the flow field.

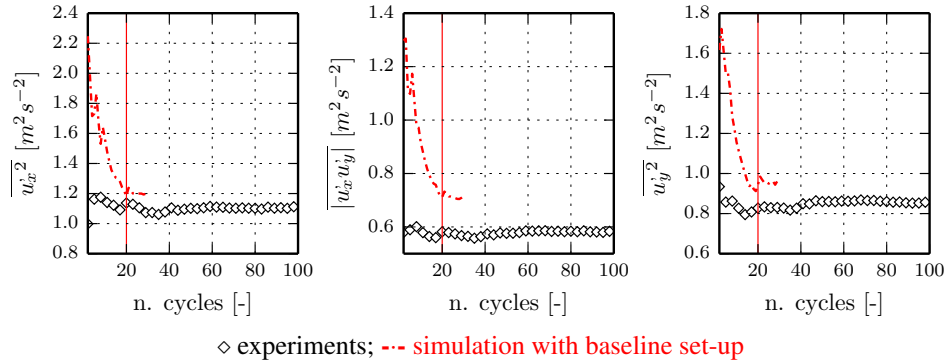


**Figure 5.5:** Convergence of the Variance of the resolved velocity field on the symmetry plane.

### 5.3.1 “Uncompressed-vortex” case

**Table 5.1:** CPU wall-clock time per cycle of all simulation cases

turbulence model	grid resolution	CFL	coupling algorithms	wall-clock time (hours)
DLRM	low <sup>1</sup>	0.9	PISO	≈ 4.0
LES (sigma)	low <sup>1</sup>	0.9	PISO	≈ 3.9
RANS ( $k - \omega$ SST)	low <sup>1</sup>	0.9	PISO	≈ 4.0
DLRM	low <sup>1</sup>	5	PIMPLE	≈ 5.0
DLRM	high <sup>2</sup>	5	PIMPLE	≈ 21.5

1: “coarse grid”,  $\Delta_{mesh} \approx 2mm$

2: “fine grid”,  $\Delta_{mesh} \approx 1mm$

Table 5.1 reports the dependences of the computational power from the turbulence model, the time step and the average dimension of the mesh. All simulations are performed on a Linux Desktop-PC powered by a 8-core Intel-Xeon CPU (E5-2650, 2.30 GHz) and 32 GB RAM. It’s worth mentioning that a higher CFL number actually increases CPU time. The reason is that PISO algorithm is not sufficient when CFL number is higher than unity, and more outer iterations are necessary for the more consistent PIMPLE algorithm to enforce the mass conservation.

First validation of the numerical methods is performed by comparing the mean flow tumble ratio ( $R_t$ ).  $R_t$  is defined as the ratio between the mean angular velocity of the

two-dimensional flow and the angular velocity of the crankshaft [47]. Fig. 5.6 shows two sets of  $R_t$  calculated with different choices of the reference rotation axes [39]: Values of the  $R_t$  using large scale vortex center as reference axes (Fig. 5.6, left) differ slightly from those using geometric center of the x-y plane as a reference axes (Fig. 5.6, right). In both cases, values of  $R_t$  are higher than a typical gasoline engine in the real world, since the square piston engine works under low speed (RPM = 206), and its layout of the intake channel greatly facilitates tumble generation. Nevertheless, simulation results of DLRM show good agreement with experimental data, despite the low grid resolution used.

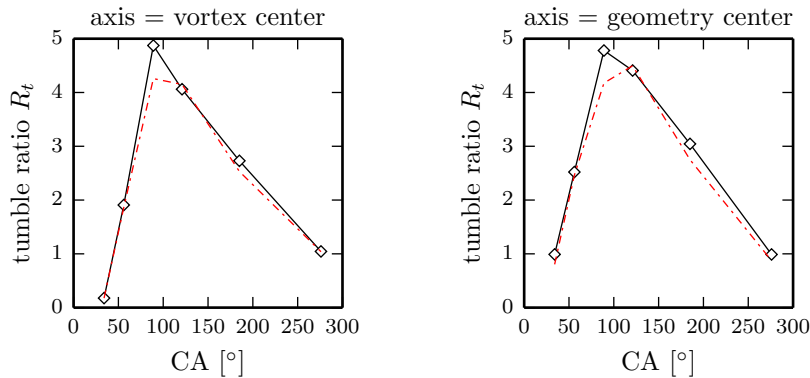


**Figure 5.6:** Mean Tumble Ratio of the “uncompressed-vortex” case: —◇— experiments; --- DLRM

Fig. 5.7 shows the sequence of snapshots of the trajectories and the contour plot of the ensemble mean flow on the symmetry x-y plane. During intake stroke (34, 56, 89, 121 CA), the velocity field is dominated by the development of two counter-rotating vortices, the large-scale tumble vortex is generated by the reflection of the inlet jet develops along the surface of the piston, and a smaller recirculation vortex is generated before the corner between the piston and lower cylinder liner due to the separation of boundary layer. Performances of turbulence models are different from each other in the region around the jet and near the piston wall, where hybrid model DLRM recovers to RANS since grid resolution is regarded as not enough to properly resolve the turbulent scales of interest. As a consequence, in the case of using the coarse grid, DLRM and RANS are more accurate than conventional LES thanks to the less grid dependent nature and the more robust near wall treatment inherited from RANS.

During exhaust stroke (276, 306, 327 CA), the inlet jet disappears and the large

scale tumble motion is gradually pushed out of the cylinder. The overall turbulence level is reduced as the kinetic energy of the mean flow dies down. DLRM and conventional LES behave similarly in the recirculating regions during exhaust stroke, indicating that the numerical resolution is sufficient there for LES to resolve enough flow scales. RANS, on the other hand provides less accurate results compared to the scale resolving approaches. More detailed analysis would be discussed based on the results shown in Fig. 5.8 to 5.23, which compare the mean flow and the variance on two sample lines intersecting the center of the symmetric x-y plane. For each crank angle analysed, the performance of different turbulence models are compared, with identical numerical set-up, namely coarse mesh, and lower than 1 CFL number. Then the dependency of the proposed method on time step advancement and mesh resolution are investigated separately.

Fig. 5.8 and 5.9 correspond to a very early stage of the intake stroke ( $CA = 34^\circ$ ). The tumble vortex is already visible at this time, although with much smaller length scale compared with its later evolution, since the redirection of the jet consume a large portion of small liner height at current CA. As for the verdict of different turbulence method, both DLRM and conventional LES give accurate predictions on both mean flow and the second moment, however the mean flow calculated by RANS is far from being reasonable. In fact, conventional LES slightly out performs DLRM, suggesting a low turbulence level of the flow field at current CA, which could be an explanation for the somehow poor performance of RANS.

Second and third row of Fig. 5.8 and 5.9 show the influence of the time step advancement and mesh resolution, with the first sub-figure ( $g$  or  $m$ ) of each row plots the phase averaged value of damping function  $\overline{g^2}$ . It is found that the hybrid model (DLRM) works in pure RANS mode in the regions of boundary layer and the inlet jet. The former one is desirable so that wall function derived from RANS could be adopted without ambiguity, whereas for the inlet jet, the explanation is just that the mesh resolution is regarded as not sufficient, based on the integral length scales estimated by RANS ( $k - \omega SST$  in current study). Considering the fact that prediction of RANS on the mean flow is not very satisfactory at least for current CA, performance of DLRM is also influenced. It is also noted that smaller time steps provide little benefit on the



coarse mesh, since the maximum CFL lies in the jet region where all turbulence scales are modelled by RANS. However, a direct refinement of the mesh yields more effective numerical resolution, leading to both much decreased values  $\overline{g^2}$  and better prediction compared with experimental measurement, as shown in the 3rd row of Fig. 5.8 and 5.9

As the piston continues to accelerate and moves towards BDC, the large scale tumble vortex take a more definite form, as shown in Fig. 5.7 and Fig. 5.10 to 5.13. The tumble motion gains momentum from the inlet jet, which is intensified by downward motion of the piston. As a consequence the vortex core lifts gradually in  $y$  direction and at  $CA = 89^\circ$  it is located almost in the middle of the cylinder. Moreover, the separation of the boundary layer on the bottom cylinder wall forms a recirculation vortex in the lower right corner of the cylinder, which rotates in the opposite direction of the tumble motion. Both of these two macroscopic structures in the mean flow are captured by all the turbulence methods, while DLRM does provide slightly better prediction, due to the reason mentioned before. Predicting the flow fluctuation is much more demanding though, as shown in the sub-figures in the first row of Fig. 5.10 to 5.13 comparing the variances on the sample line. Compared with the experiment measurement, highest discrepancies typically occur at the edge of tumble motion (conventional LES at  $CA = 56^\circ$ ), or within the area where tumble and recirculation vortex compete and transfer energy between each other (DLRM at  $CA = 89^\circ$ ). Clearly small scale fluctuations are stronger in the periphery of the coherent motions in the mean flow, where mean flow could not maintain its dominance and transfer more kinetic energy to higher order structures. The most effective way to improve the prediction is to increase the mesh resolution, as shown in the 3rd row of Fig. 5.10 to 5.13. Lower time steps give little benefit though, due to the reason explained before and the fact that the jet region is still nowhere near being partially resolved, as shown by the  $\overline{g^2}$  plotted in sub-figures  $g$  and  $m$ .

The tumble vortex gets further lifted along  $y$  direction during later stages of the intake stroke and occupies the majority of the cylinder, as shown in Fig. 5.14 and 5.15 for  $CA = 121^\circ$ . While DLRM continues to give reasonable predictions on the mean flow structures, conventional LES struggled with the poor near wall resolution, which also pollutes the quality of simulation of the entire flow domain. It is necessary, how-

ever, to keep in mind that the major reason behind the poor prediction of LES could be attributed to the low grid resolution being adopted by the baseline set-up, which is not at all the suitable case for conventional LES. In fact, quality of the simulation improves on finer mesh, sometimes significantly even for hybrid model (DLRM) which is designed to be more compatible with coarse mesh. However, as better computational efficiency is one of the most important object of the proposed numerical method, a sufficient coarse mesh is adopted by the baseline set-up (shown by the first row of Fig. 5.14 to 5.23), since the quality of the simulation with low computational cost is of great interest in current study.

Fig. 5.16 and 5.17 shows the flow structure in proximity of bottom dead center (BDC). The averaged profiles of  $\bar{U}_x$  and  $\bar{U}_y$  are predicted with good accuracy by DLRM and conventional LES, while tumble vortex center predicted by RANS shows a small deviation from experimental measurement in the x direction, which actually yields an somehow unfair discrepancy if results are compared only on the vertical sample line in the first row of Fig. 5.16, as the gradient of velocity is huge near the vortex center. As for the predictions of flow unsteadiness conventional LES still struggles with the low mesh resolution of the near wall region where it turns to overestimate the turbulent fluctuation. DLRM managed to maintain a more reasonable prediction however the overall quality is not comparable to the previous crank angles. Once again a refined grid is a much more effective solution to improve the quality, whereas smaller time steps are not as efficient.

It is necessary to admit that for the “uncompressed vortex ” case, flow conditions during the exhaust stroke (from CA = 185 ° to CA = 360 °) are quite different from those of a real engine. However, comparisons between simulation and experiment results would still be discussed briefly, as part of the validation of the proposed simulation method.

For the test case currently being studied, as the piston moves back towards cylinder head during exhaust stroke, the uncompressed charge, along with large scale tumble vortex, are gradually pushed out of the cylinder. As shown in Fig. 5.18 and 5.19, the recirculation vortices originated by the separation of boundary layer became the only major coherent structure in the exhaust stroke, however due to the disappear of the inlet

jet, such rotation motion is only sustained by the inertial force and it is also pushed away from the original recirculation region (the corner between piston and lower liner wall). As shown in the first row of Fig. 5.18 and 5.19, conventional LES still suffers from the insufficient grid resolution, however it captures the transition procedure with better accuracy than other two turbulence models. A more detailed analysis would be discussed in the following chapter, however one explanation for the lower performance of RANS and hence DLRM could be the adoption of wall function, which in theory and in most cases as discussed before is the advantage of RANS and DLRM. Wall functions, especially the log law are based on the statistics from well-developed channel flow, however during the transition (from BDC to around  $CA = 306^\circ$  as shown in Fig. 5.7), the inlet jet is in very low speed or most of time totally disappears, whereas the reversed in-cylinder motion has not being established to justify enough similarity to a well-developed channel flow, especially in the near wall region around lower cylinder liner. The error caused by the wall function could be mitigated by a sufficiently refined (in the RANS point of view) boundary layer, since the low Reynolds treatment of the wall function would not resort to the log law assumption. The third row of Fig. 5.18 and 5.19 show that reproduction of the flow field gets improved by using fine mesh, whose first cell near the wall is put inside the viscous sub-layer.

At the end of the exhaust stroke (i.e. for  $CA = 306^\circ$  and  $327^\circ$ ), the recirculation vortex is also pushed out of the cylinder. Inertial of the inlet flow dies down so the velocity of the charge is organized towards the intake (outlet) channel. It is found that RANS is capable of provide more accurate phase-averaged information after the transition period mentioned before, indicated by the improved prediction from both RANS and DLRM, as shown in the first row of Fig. 5.20 to 5.23. Conventional LES turns to overestimate the turbulence fluctuation, since the SGS model could not provide enough dissipation should a coarse mesh being used. Solution of DLRM on the same grid is much more stable, and it is noted that smaller time steps alone do bring some advantages when using the coarse grid, although the benefit from a refined mesh is still much more straightforward.

As a brief conclusion of the validation of DLRM on the “uncompressed-vortex” case, it is safe to regard DLRM as an scale resolving turbulence method with good

adaptability to coarse mesh. Thanks to the non-zonal hybridization, the wall function derived from RANS could be adopted without the ambiguity on the nature of the flow being ensemble averaged or spatial-filtered. DLRM certainly would suffer from some of the inherent drawbacks of the parent RANS model, especially when RANS fails to reproduce the mean flow. Similar to conventional LES, simulation results of DLRM is both grid and time dependent unless the numerical resolution is sufficient for a “fully-resolved” LES. Since a refined mesh provides both higher spatial resolution and better temporal resolution (through the CFL criterion), the effect of increase grid resolution is much more obvious compared with adopting smaller time steps.

### 5.3.2 “Compressed-vortex” case

The “compressed-vortex” case includes the valve (guillotine) motion (Fig. 5.3) so it is more representative of the operation of a four-stroke engine [12]. Besides, the dynamic mesh algorithms required to move the piston and the guillotine together also agrees with the need for more realistic IC-Engine simulation [56].

Similar to the uncompressed-vortex case, 30 consecutive engine cycles are simulated and the first two are discarded. The same coarse grid (apart from the guillotine region) is used as the proposed simulation method intends to maintain the low the computational cost of RANS.

Fig. 5.24 show the trajectory of the mean flow on the x-y symmetric plane at different crank angles, during the intake (35, 57 and 90 CA) and the compression (185, 278, 293 and 310 CA) stroke, which is coloured by the magnitude phase-averaged velocity. It is shown that the major flow features are properly reproduced by simulation, despite the low grid resolution being adopted.

Fig. 5.25 to 5.36 report the comparison of ensemble-mean and the variance of the resolved velocity field on the sample lines over the x-y symmetric plane. Most of the crank angles are chosen from the intake and the compression stroke, where the evolution of the tumble flow and the energy transfer between large and small scale flow motions are of great interest to the real engine, as the modern direct injection gasoline engine relies ongoing elevated tumble ratio to promote higher turbulence level for spray atomization and faster flame propagation [81].

The intake strokes of “compressed vortex” and “uncompressed vortex” are quite similar since they start from similar initial conditions, at least from an ensemble-averaged point of view. As a results, similar behaviours are observed for the performance of different turbulence models: In the early stage of the intake stroke, as shown in Fig. 5.25 to 5.26 for  $CA = 35^\circ$  and  $74^\circ$ , flow velocity, hence the overall turbulence level of the engine charge is low. RANS is not designed for such flow situation so it tends to over-predict the dissipation effect, which would certainly has its impact on DLRM, as sometimes a large portion of the fluctuation in the resolved velocity is smoothed out (e.g. in Fig. 5.26-(f) and (i)). Part of the over dissipation effect should also be attributed to the use of wall function. Converse to RANS or hybrid model, conventional LES typically performs better where turbulence level is low, however turns to underestimate the dissipation effect from sub-grid scales where turbulence level is high enough to justify RANS. This clearly is directly due to the insufficient mesh resolution, never the less, combine the best performance of conventional LES and RANS, there is still more potential for a hybrid model to take the best from both sides.

During the later stage of intake stroke and the initial stage of the compression stroke (eg. Fig. 5.27 to 5.29 for  $CA = 123^\circ$ ,  $185^\circ$  and  $248^\circ$ ), the performance of DLRM gets improved, as the overall turbulence level is increased so turbulence statistics are estimated with better accuracy. DLRM generally out-performs conventional LES since the later overestimates the flow fluctuations due to the reason mentioned before, one extreme example is found for  $CA = 248^\circ$ , where the variance of velocity in the x direction predicted by conventional LES is one order of magnitude higher than DLRM, whose prediction agrees reasonably well with experimental measurement.

The later stage of compression stroke is quite different from the 2nd stroke of the “uncompressed case”, as the large scale tumble motion is not pushed out of the cylinder, but rather kept inside and get intensified due to the reduction of the cylinder volume. The energy transfer between the tumble vortex and smaller turbulence scales is quite important since it is an important strategy to promote high turbulence level in the cylinder. Results sampled for  $CA = 278^\circ$ ,  $293^\circ$ ,  $310^\circ$ ,  $334^\circ$  in Fig. 5.30 to 5.33 show that the overall turbulence level does get improved, as the magnitude of the variance almost gets doubled from the middle of the stroke to the compression TDC. Overall DLRM

gives reasonable prediction for both mean flow and 2nd moment unsteadiness, which out-performs both RANS and LES. However, underestimation of the fluctuation should also be noticed, especially for the area around the tumble vortex center. Such underestimation should mostly be attributed to the different positions of vortex centres of the experimental measurement and the one predicted by DLRM. The underlying reason for such error is still unknown to the author, however it could be result of the charge leakage during the experiment, which is expected to be as high as 10 % of the overall engine charge [12].

After the compression stroke, the remaining CAs are less representative to a real-world engine, since the optical engine does not consider combustion. The results shown after the compression TDC ( $CA \leq 365^\circ$ ) are compared purely for validation purpose. Overall during expansion stroke all the turbulence method managed to give reasonable predictions. However in the late stage of exhaust stroke, similar behaviour of overestimation of the unresolved turbulent dissipation as in the early stage of intake stroke could be observed.

The general conclusion for the validation on the “compressed vortex” case is similar to that for the “uncompressed vortex”. As the hybrid model is generally capable to adjust its modelling behaviour according to the local flow conditions, it also inherits some of the drawbacks of the parent RANS model. Especially in situations where the overall turbulence level is low, and RANS provides inaccurate flow statistics. Due to the fact that a conventional LES tends to behave better in those circumstances, the hybrid method could potentially improve its modelling behaviour.

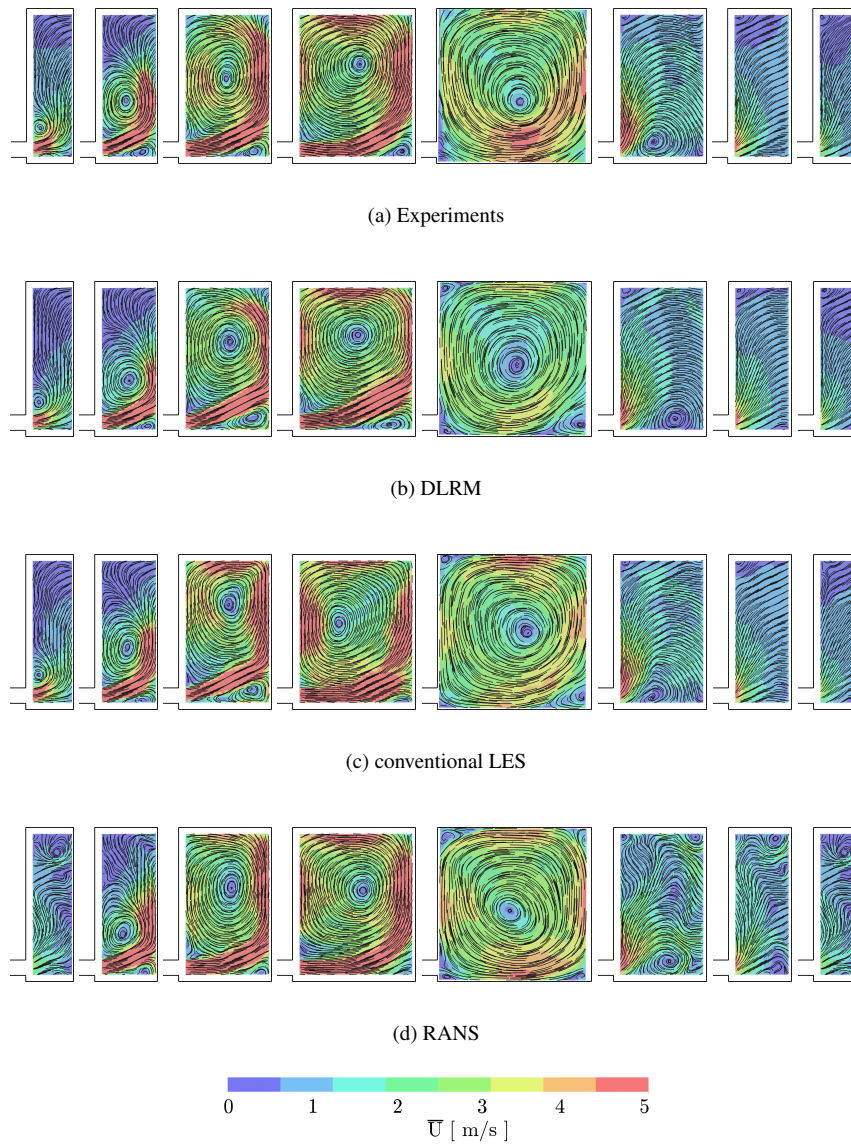
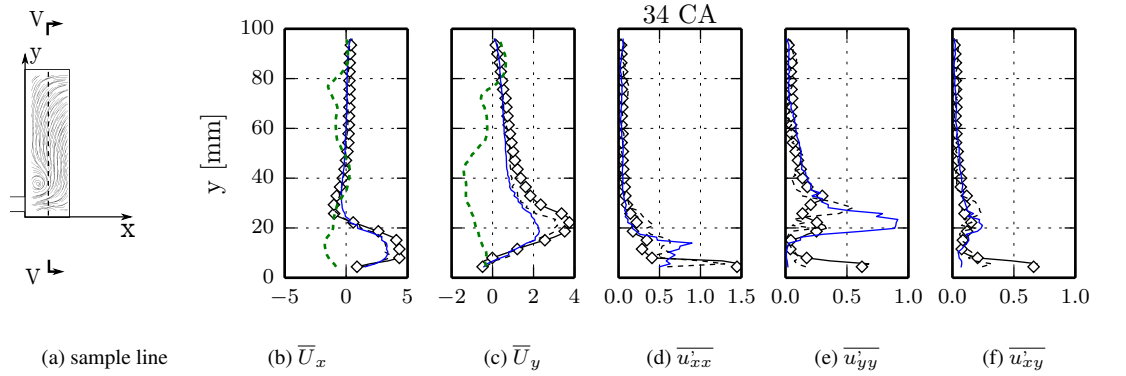
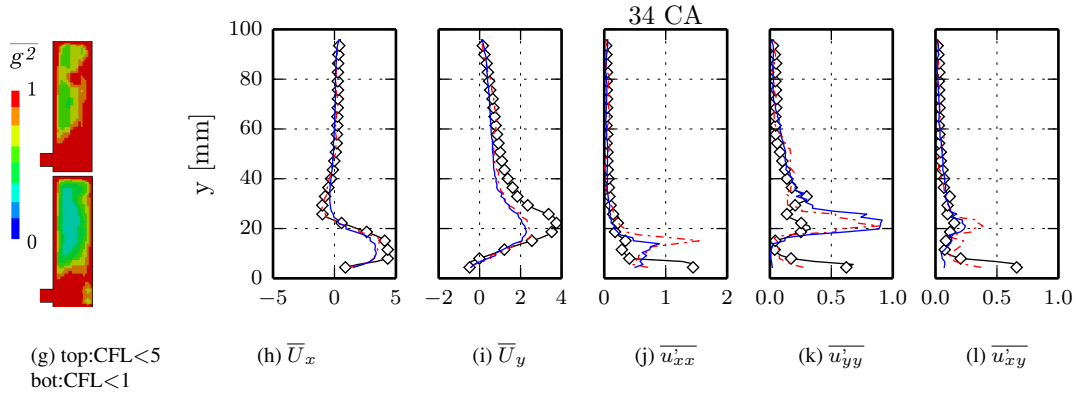


**Figure 5.7:** Evolution of the ensemble mean flow on symmetric  $x$ - $y$  plane over the engine cycle at (left to right): 34, 56, 89, 121, 185, 276, 306, 327 CA. a) averaged over 100 PIV realizations; b), c), d): coarse grid,  $CFL < 1$ , averaged over 28 simulation cycles

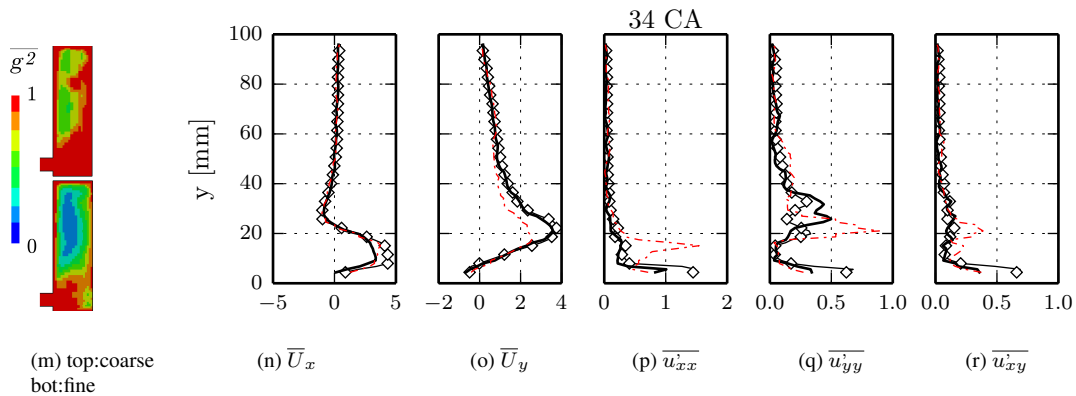
Chapter 5. Validation of the numerical method



Comparison of different turbulence models (coarse grid, CFL<1):  $\diamond$  Exp; — DLRM; - - - LES; ····  $k\text{-}\omega$  SST



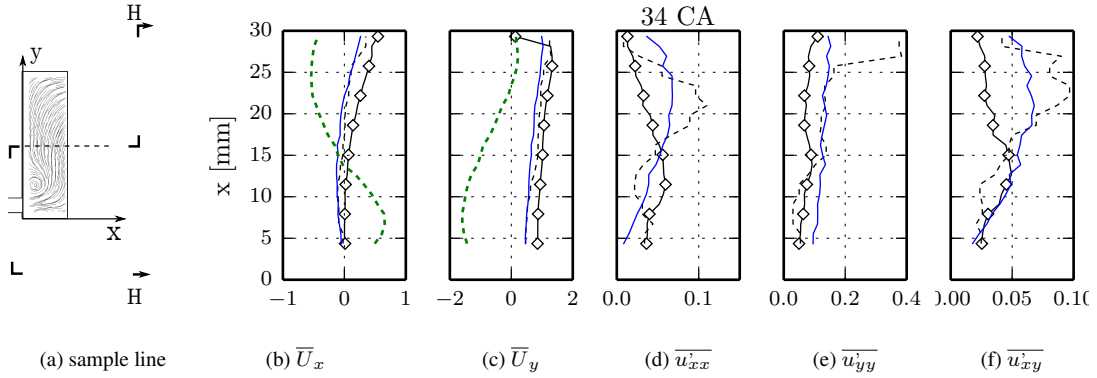
Influence of time step advancement (DLRM, coarse grid): — CFL<1; - - - CFL<5



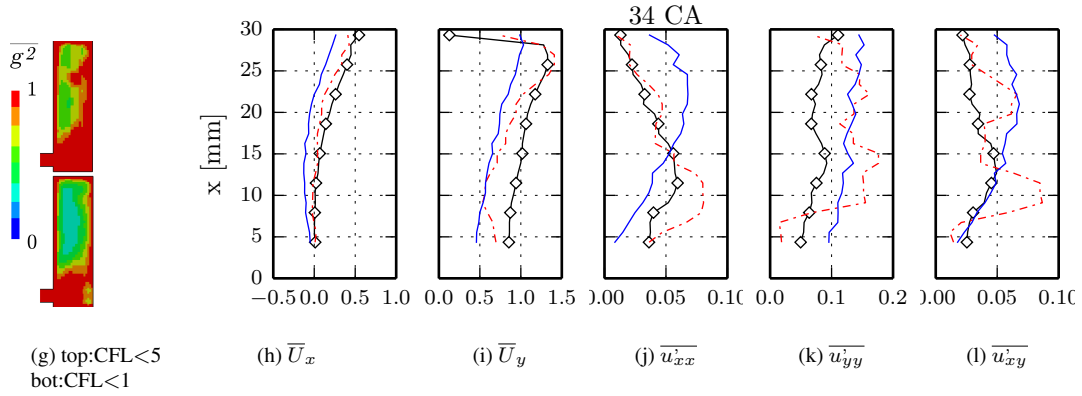
Influence of mesh resolution (DLRM, CFL<5): - - - coarse grid; — fine grid

Figure 5.8: Comparison of the phase-average and variance of the velocity field calculated by different turbulence models on a centered vertical line over the mid-cross x-y measurement plane, “uncompressed vortex” case.

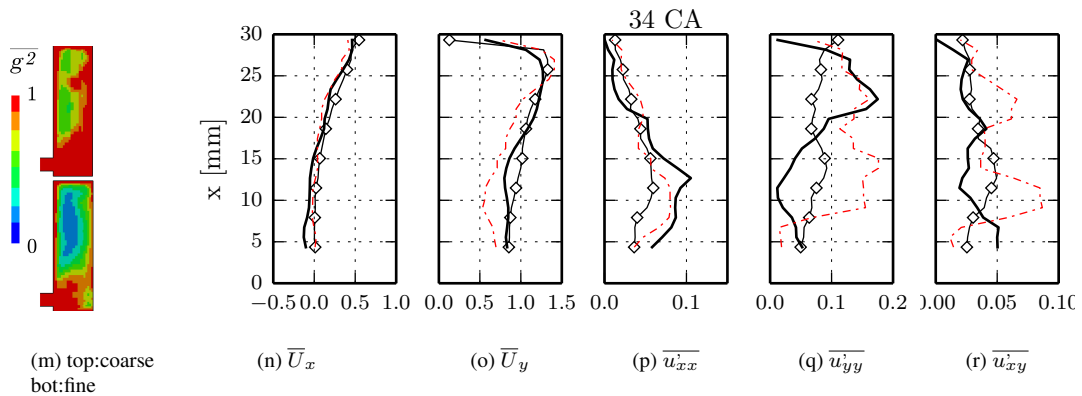




Comparison of different turbulence models (coarse grid, CFL<1):  $\diamond$  Exp; — DLRM; --- LES; ····  $k-\omega$  SST



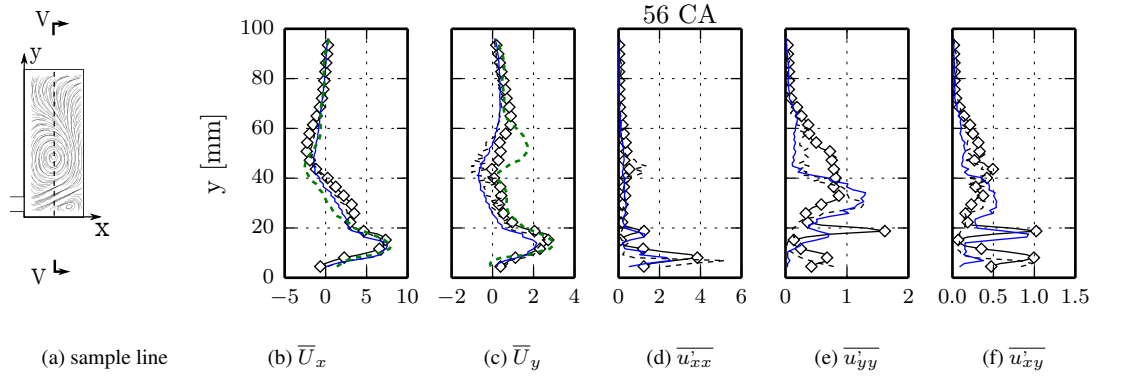
Influence of time step advancement (DLRM, coarse grid): — CFL<1; --- CFL<5



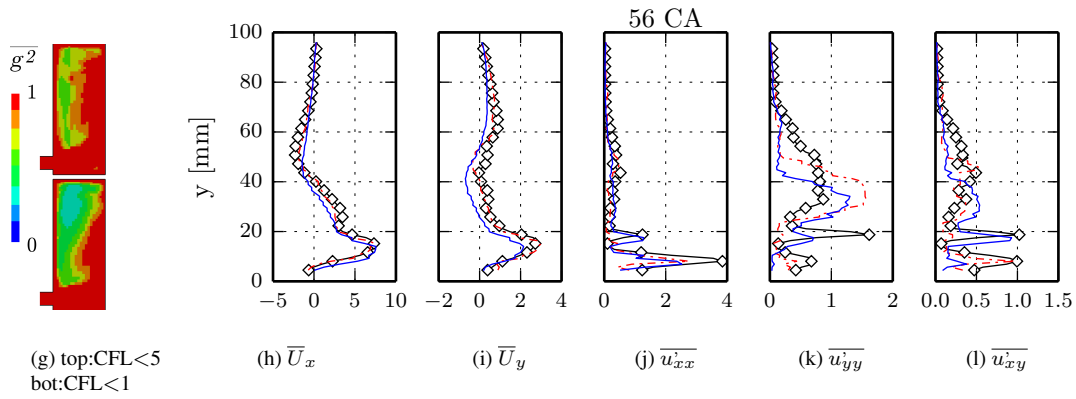
Influence of mesh resolution (DLRM, CFL<5): --- coarse grid; — fine grid

Figure 5.9: Comparison of the phase-average and variance of the velocity field calculated by different turbulence models on a centered horizontal line over the mid-cross  $x$ - $y$  measurement plane, “uncompressed vortex” case.

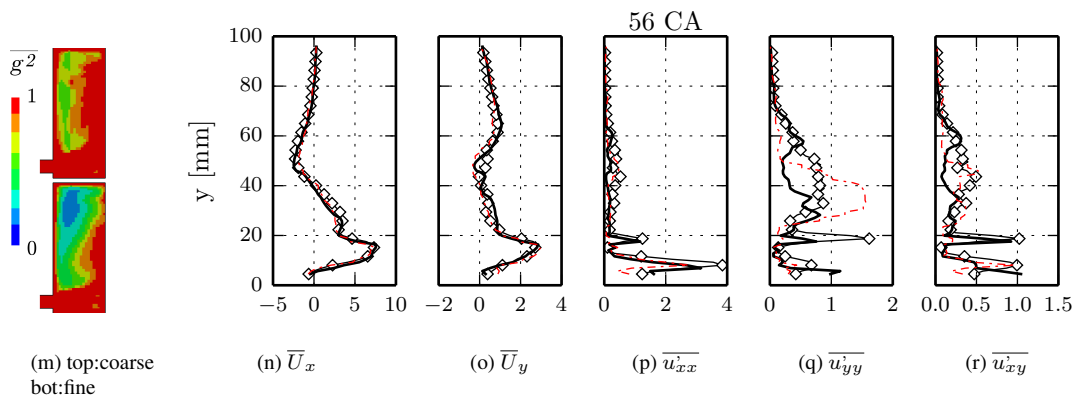
## Chapter 5. Validation of the numerical method



Comparison of different turbulence models (coarse grid, CFL<1):  $\diamond$  Exp; — DLRM; - - - LES; - · - ·  $k$ - $\omega$  SST

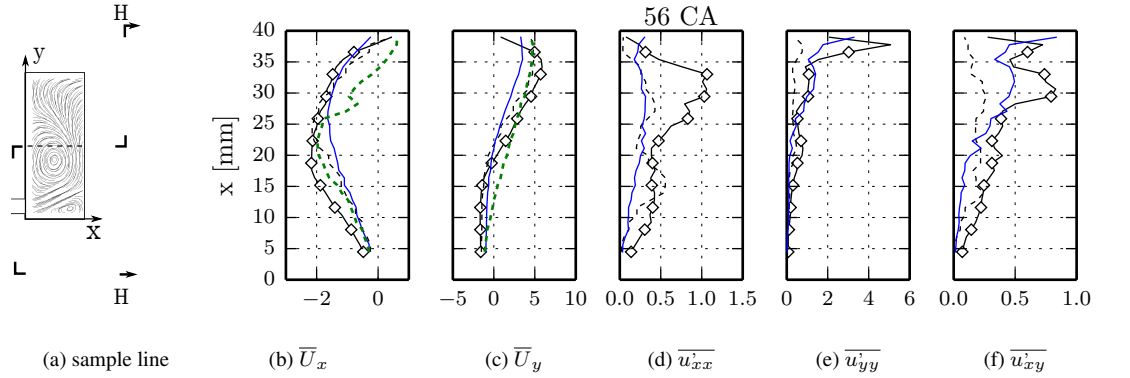


Influence of time step advancement (DLRM, coarse grid): — CFL<1; - · - · CFL<5

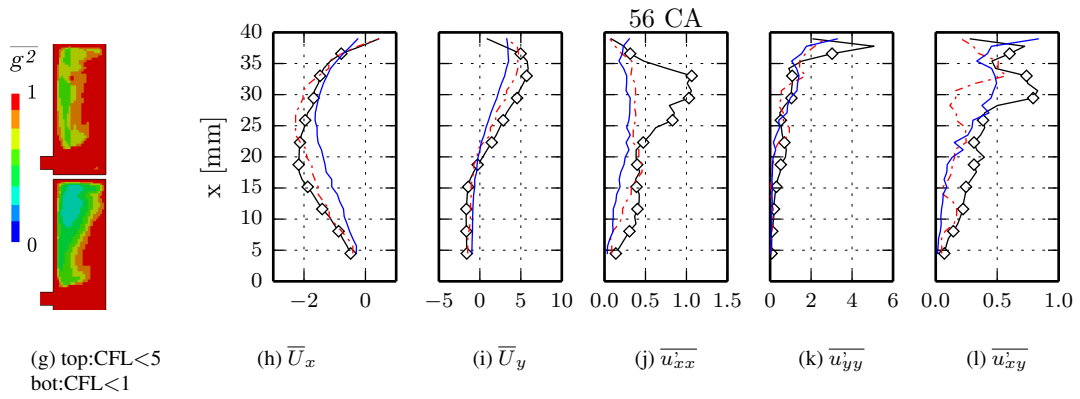


Influence of mesh resolution (DLRM, CFL<5): - · - · coarse grid; — fine grid

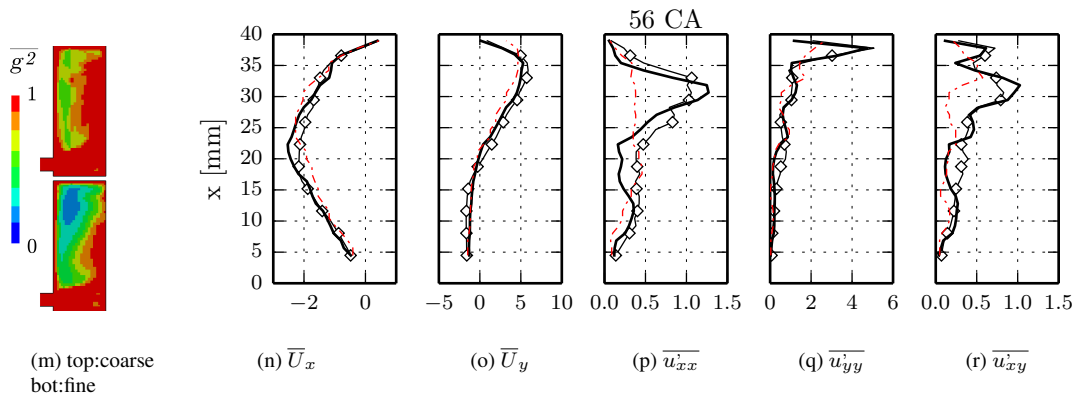
**Figure 5.10:** Comparison of the phase-average and variance of the velocity field calculated by different turbulence models on a centered vertical line over the mid-cross x-y measurement plane, “uncompressed vortex” case.



Comparison of different turbulence models (coarse grid, CFL<1):  $\diamond$  Exp; — DLRM; --- LES; -.-  $k-\omega$  SST



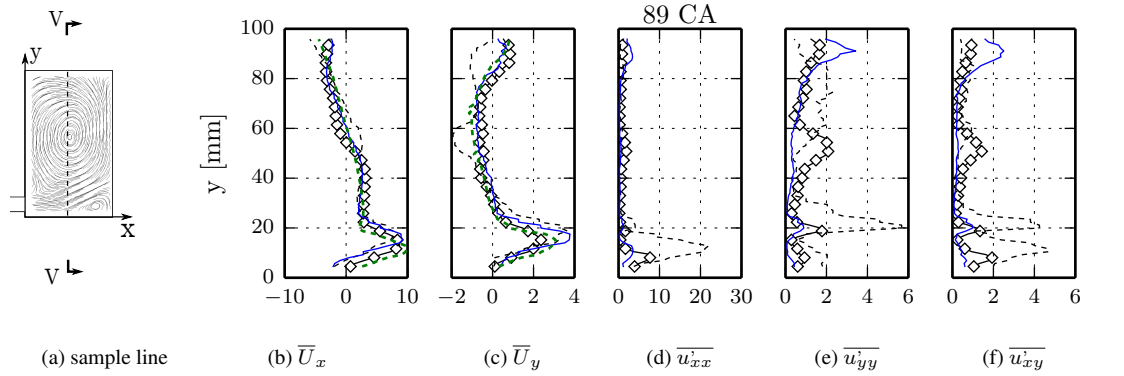
Influence of time step advancement (DLRM, coarse grid): — CFL<1; --- CFL<5



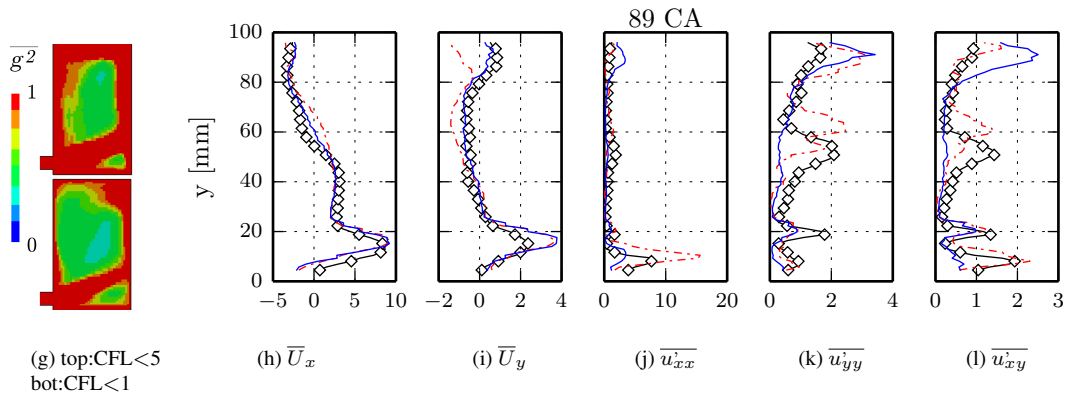
Influence of mesh resolution (DLRM, CFL<5): --- coarse grid; — fine grid

**Figure 5.11:** Comparison of the phase-average and variance of the velocity field calculated by different turbulence models on a centered horizontal line over the mid-cross  $x$ - $y$  measurement plane, “uncompressed vortex” case.

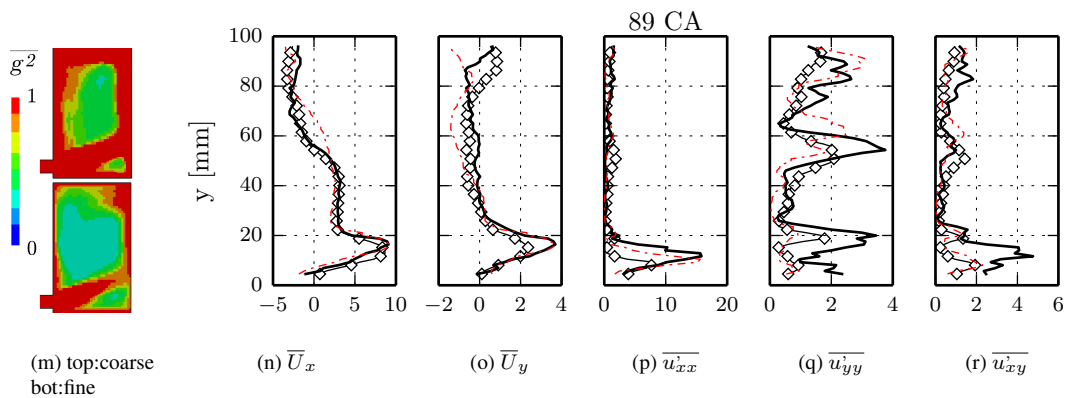
## Chapter 5. Validation of the numerical method



Comparison of different turbulence models (coarse grid, CFL<1):  $\diamond$  Exp; — DLRM; - - - LES; - · - ·  $k$ - $\omega$  SST

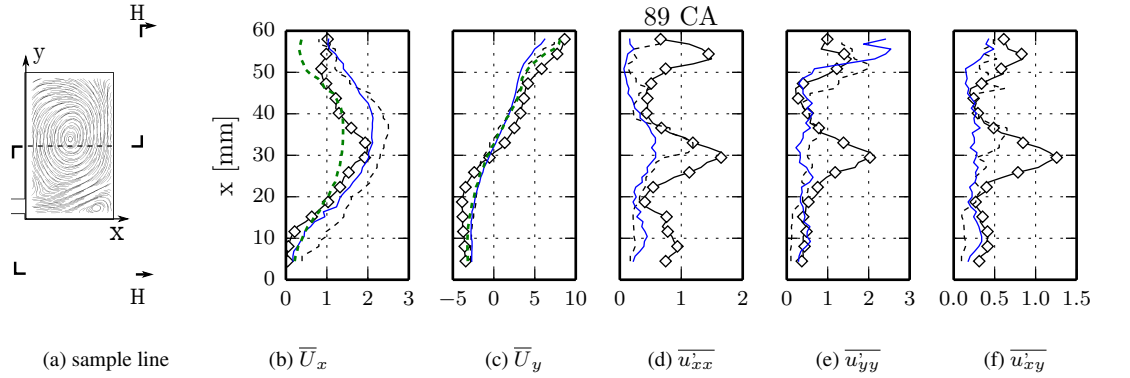


Influence of time step advancement (DLRM, coarse grid): — CFL<1; - - - CFL<5

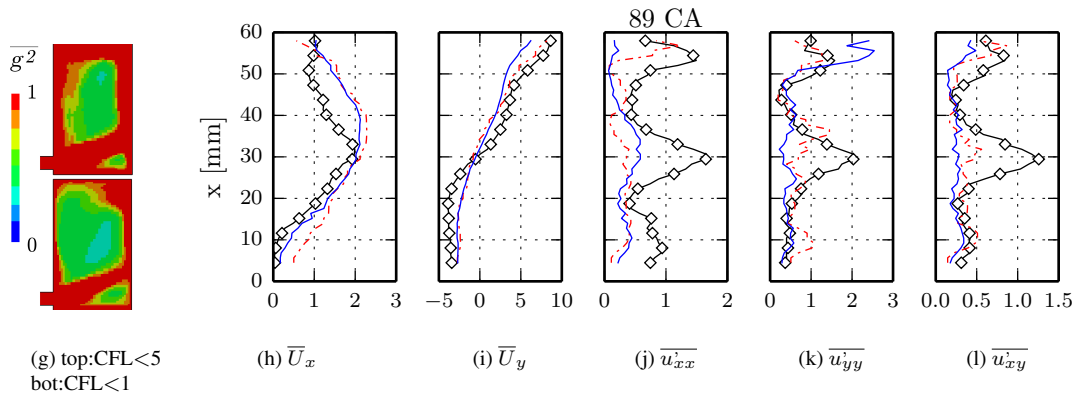


Influence of mesh resolution (DLRM, CFL<5): - - - coarse grid; — fine grid

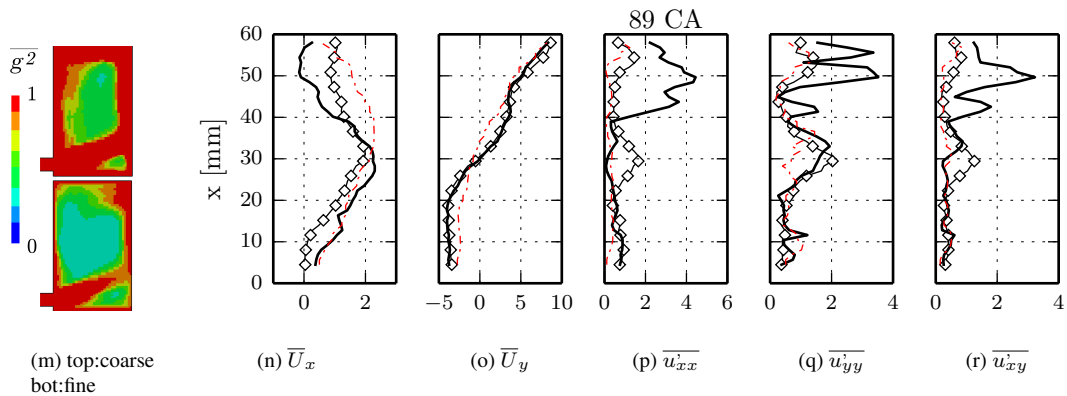
**Figure 5.12:** Comparison of the phase-average and variance of the velocity field calculated by different turbulence models on a centered vertical line over the mid-cross  $x$ - $y$  measurement plane, “uncompressed vortex” case.



Comparison of different turbulence models (coarse grid, CFL<1):  $\diamond$  Exp; — DLRM; - - - LES; - · - ·  $k-\omega$  SST



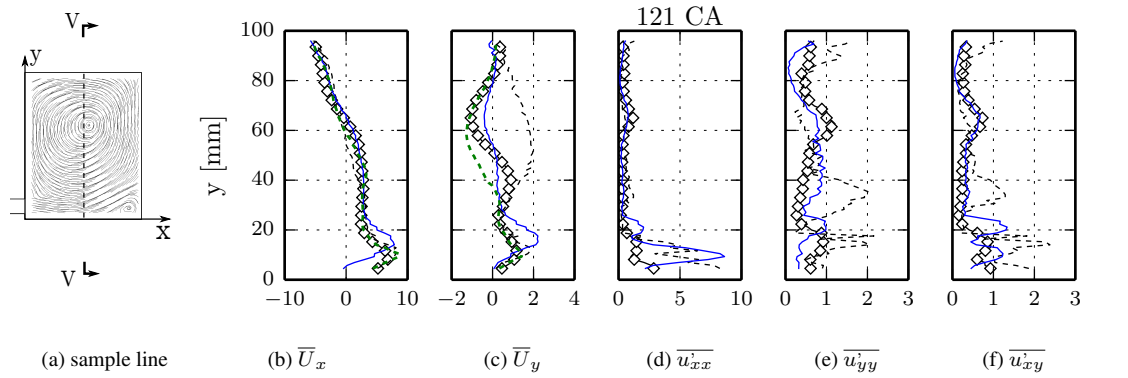
Influence of time step advancement (DLRM, coarse grid): — CFL<1; - - - CFL<5



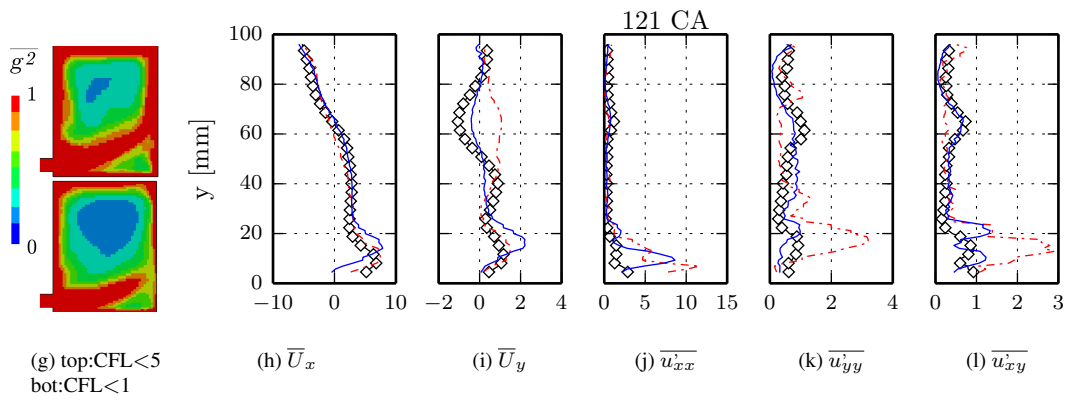
Influence of mesh resolution (DLRM, CFL<5): - - - coarse grid; — fine grid

**Figure 5.13:** Comparison of the phase-average and variance of the velocity field calculated by different turbulence models on a centered horizontal line over the mid-cross x-y measurement plane, “uncompressed vortex” case.

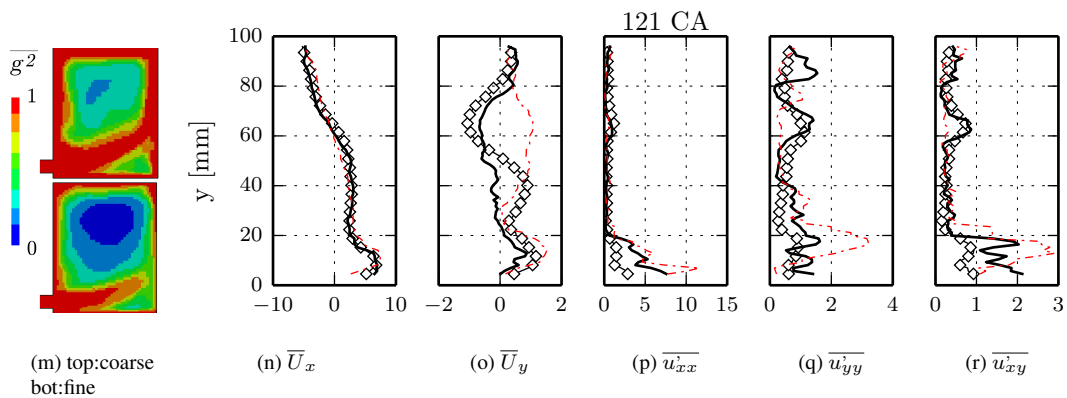
## Chapter 5. Validation of the numerical method



Comparison of different turbulence models (coarse grid, CFL<1):  $\diamond$  Exp; — DLRM; - - - LES; - · - ·  $k$ - $\omega$  SST

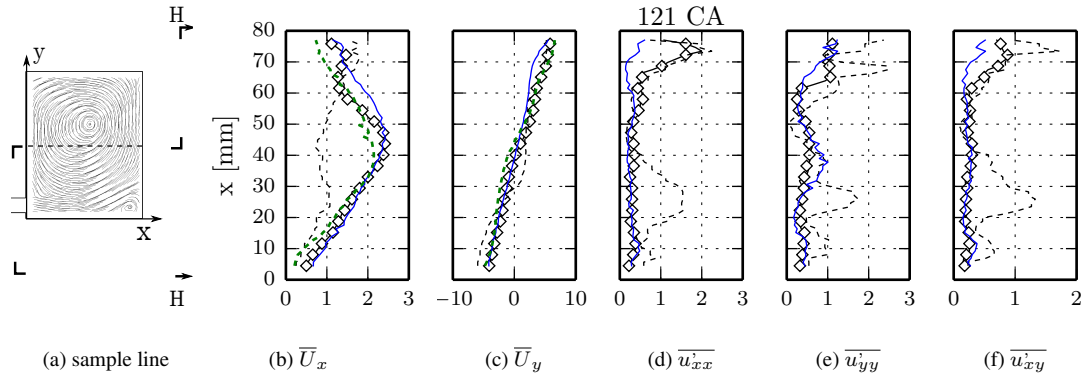


Influence of time step advancement (DLRM, coarse grid): — CFL<1; - - - CFL<5

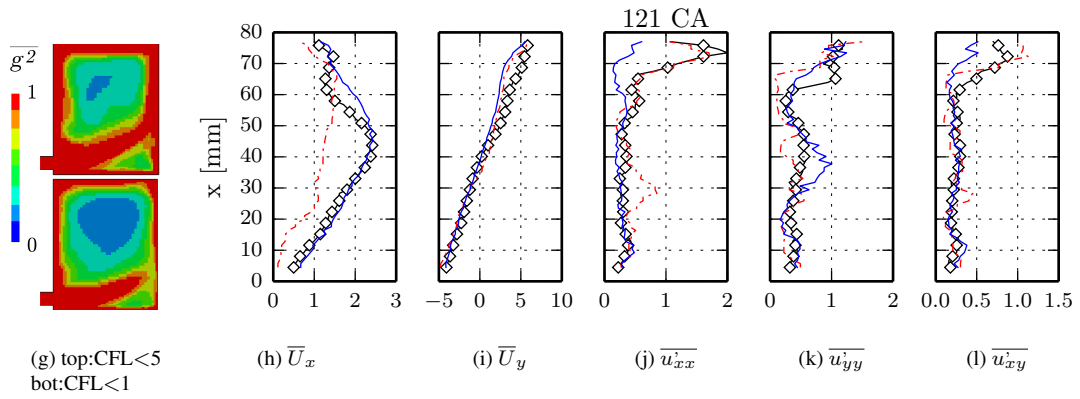


Influence of mesh resolution (DLRM, CFL<5): - - - coarse grid; — fine grid

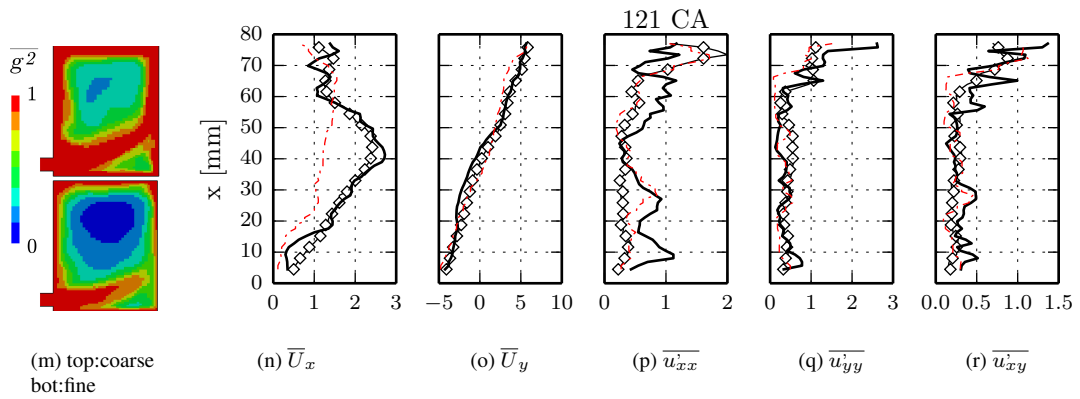
**Figure 5.14:** Comparison of the phase-average and variance of the velocity field calculated by different turbulence models on a centered vertical line over the mid-cross x-y measurement plane, “uncompressed vortex” case.



Comparison of different turbulence models (coarse grid, CFL<1):  $\diamond$  Exp; — DLRM; --- LES; -.-  $k-\omega$  SST



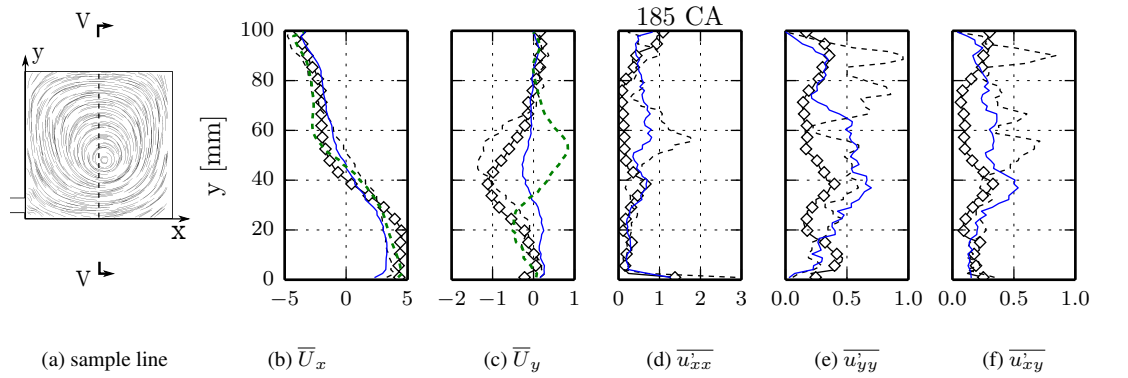
Influence of time step advancement (DLRM, coarse grid): — CFL<1; --- CFL<5



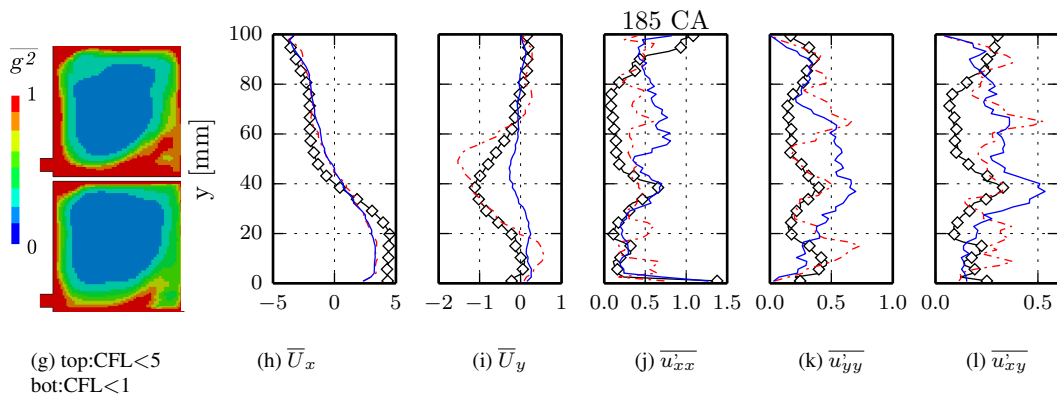
Influence of mesh resolution (DLRM, CFL<5): --- coarse grid; — fine grid

Figure 5.15: Comparison of the phase-average and variance of the velocity field calculated by different turbulence models on a centered horizontal line over the mid-cross x-y measurement plane, “uncompressed vortex” case.

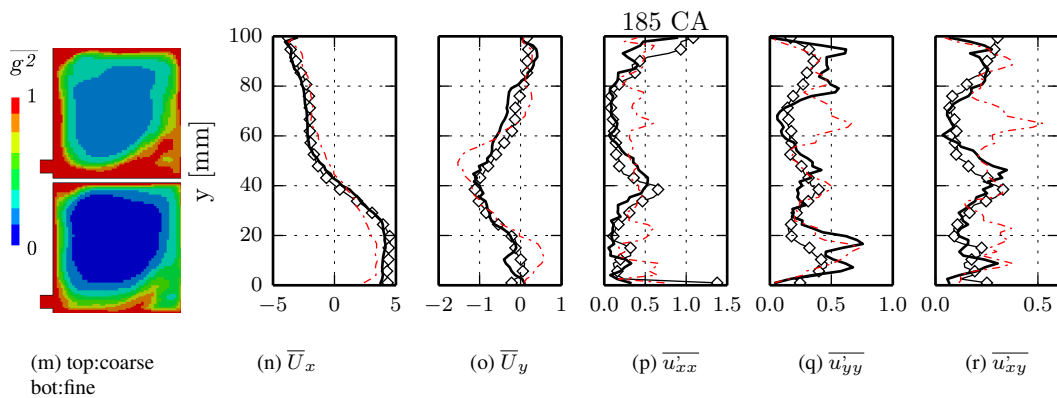
## Chapter 5. Validation of the numerical method



Comparison of different turbulence models (coarse grid, CFL<1):  $\diamond$  Exp; — DLRM; - - - LES; - · - ·  $k-\omega$  SST



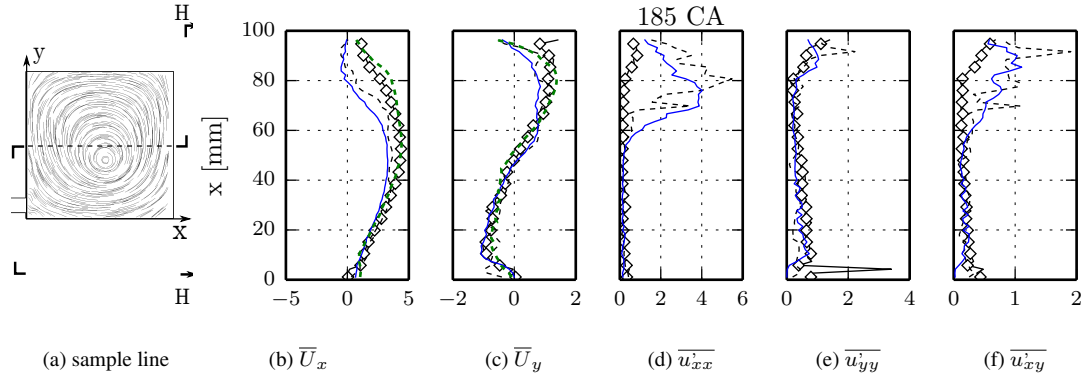
Influence of time step advancement (DLRM, coarse grid): — CFL<1; - - - CFL<5



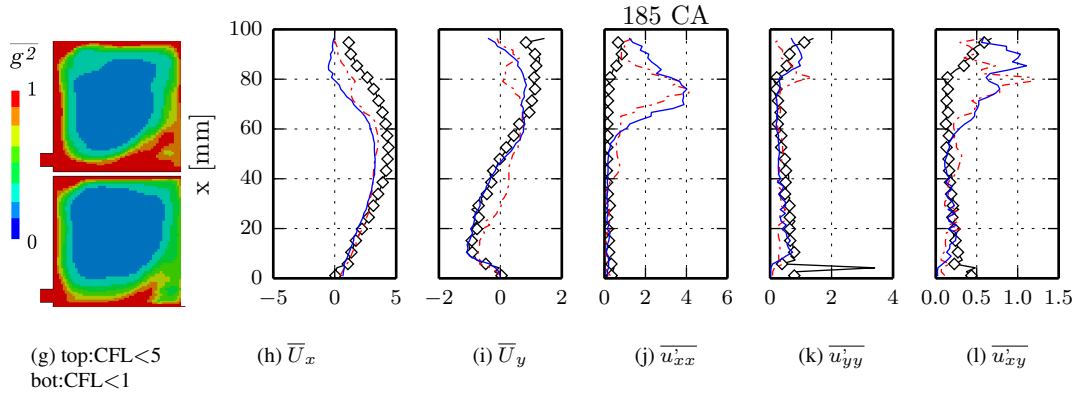
Influence of mesh resolution (DLRM, CFL<5): - - - coarse grid; — fine grid

**Figure 5.16:** Comparison of the phase-average and variance of the velocity field calculated by different turbulence models on a centered vertical line over the mid-cross x-y measurement plane, “uncompressed vortex” case.

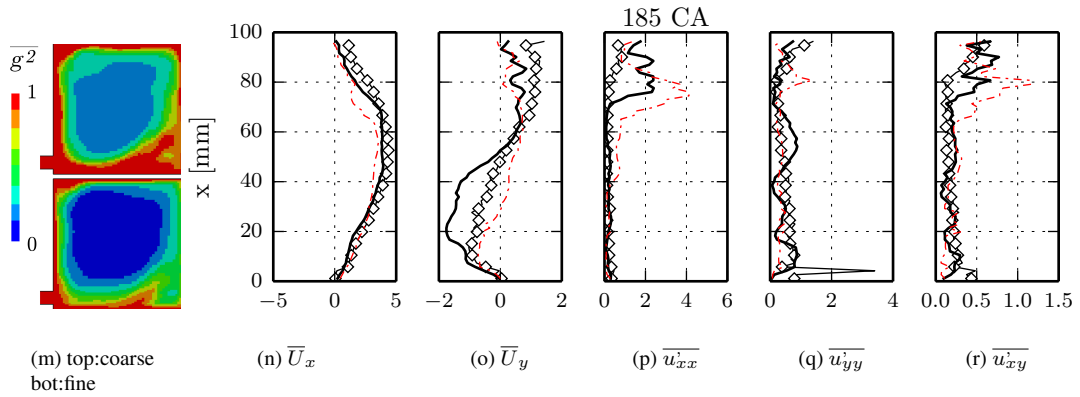




Comparison of different turbulence models (coarse grid, CFL<1):  $\diamond$  Exp; — DLRM; - - - LES; - · - ·  $k-\omega$  SST



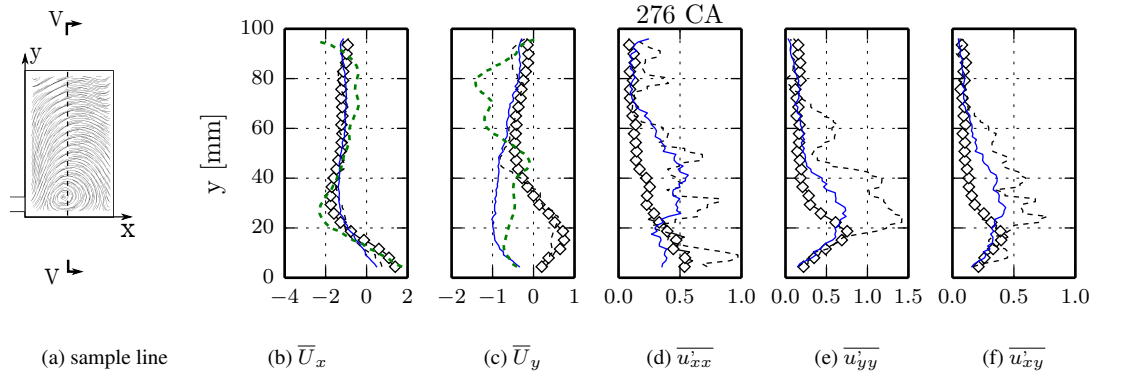
Influence of time step advancement (DLRM, coarse grid): — CFL<1; - - - CFL<5



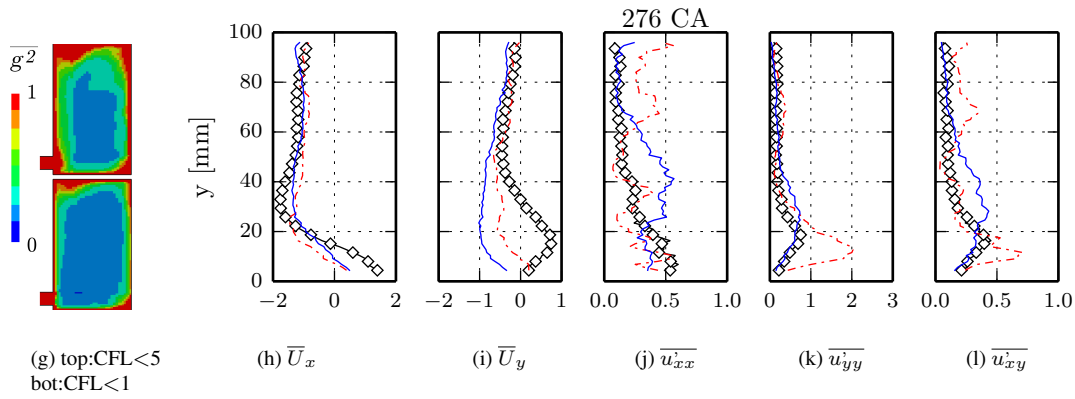
Influence of mesh resolution (DLRM, CFL<5): - - - coarse grid; — fine grid

**Figure 5.17:** Comparison of the phase-average and variance of the velocity field calculated by different turbulence models on a centered horizontal line over the mid-cross  $x$ - $y$  measurement plane, “uncompressed vortex” case.

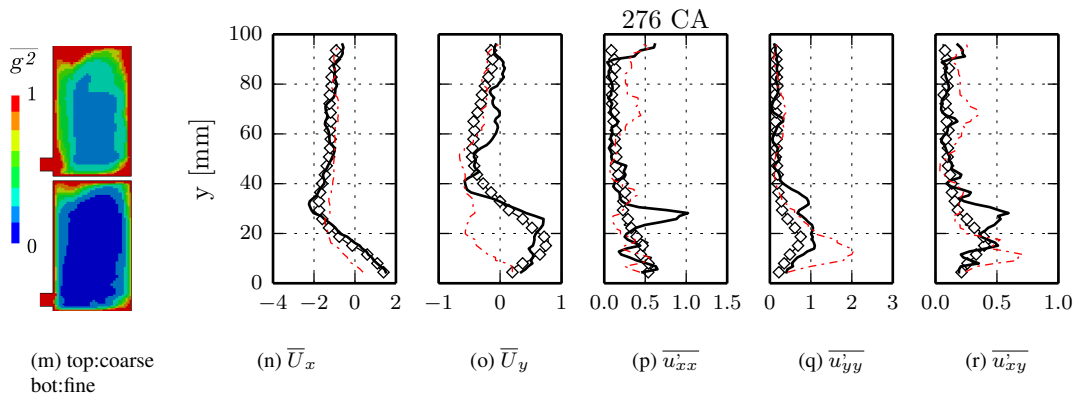
Chapter 5. Validation of the numerical method



Comparison of different turbulence models (coarse grid, CFL<1):  $\diamond$  Exp; — DLRM; - - - LES; - · - ·  $k\text{-}\omega$  SST

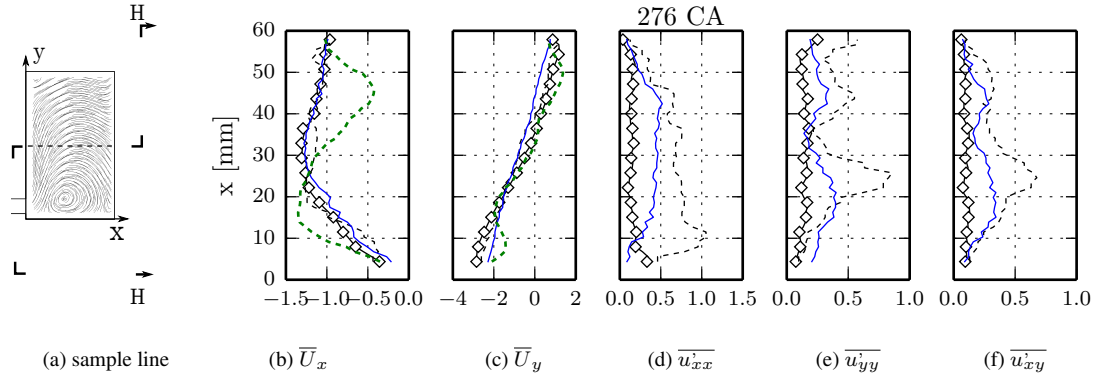


Influence of time step advancement (DLRM, coarse grid): — CFL<1; - - - CFL<5

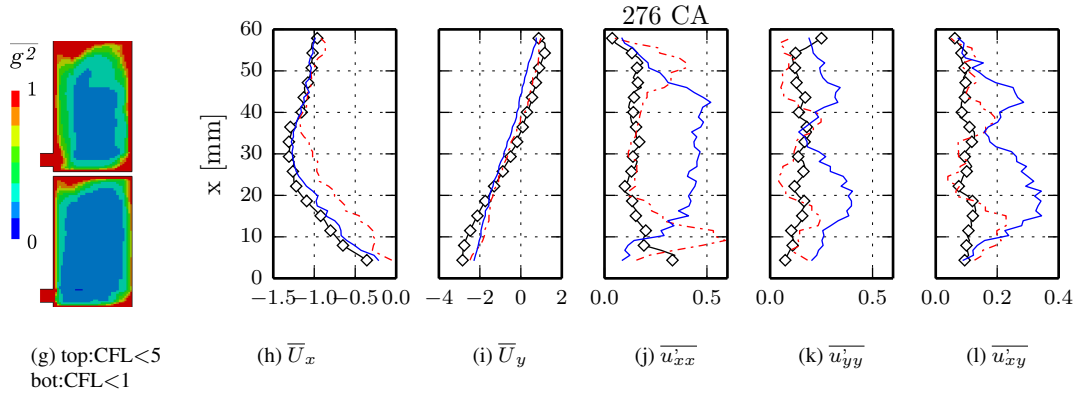


Influence of mesh resolution (DLRM, CFL<5): - - - coarse grid; — fine grid

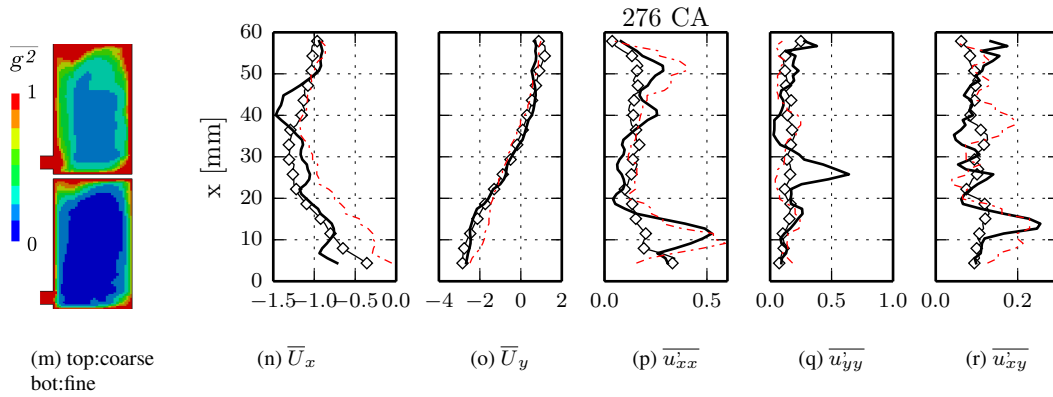
Figure 5.18: Comparison of the phase-average and variance of the velocity field calculated by different turbulence models on a centered vertical line over the mid-cross x-y measurement plane, “uncompressed vortex” case.



Comparison of different turbulence models (coarse grid, CFL<1):  $\diamond$  Exp; — DLRM; --- LES; -.-  $k-\omega$  SST



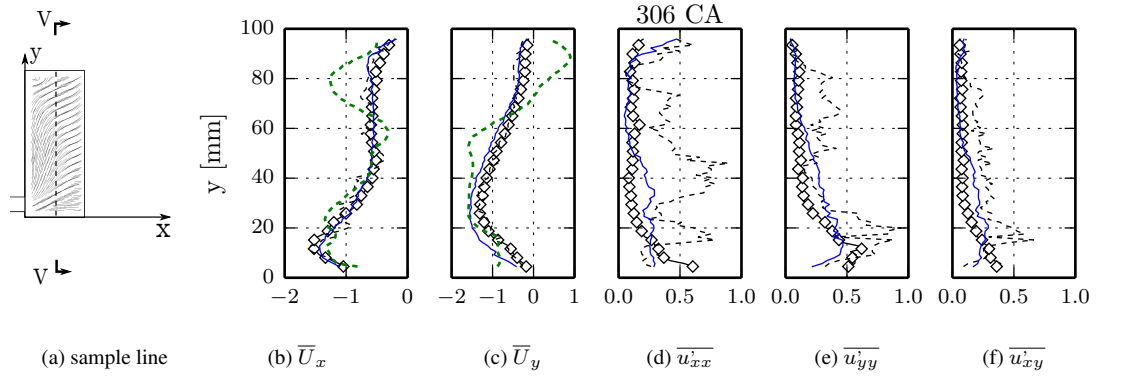
Influence of time step advancement (DLRM, coarse grid): — CFL<1; --- CFL<5



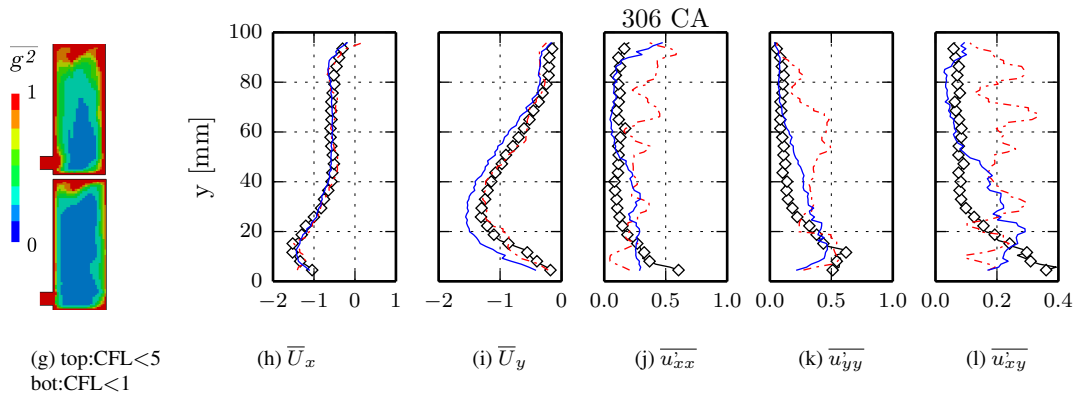
Influence of mesh resolution (DLRM, CFL<5): --- coarse grid; — fine grid

Figure 5.19: Comparison of the phase-average and variance of the velocity field calculated by different turbulence models on a centered horizontal line over the mid-cross x-y measurement plane, “uncompressed vortex” case.

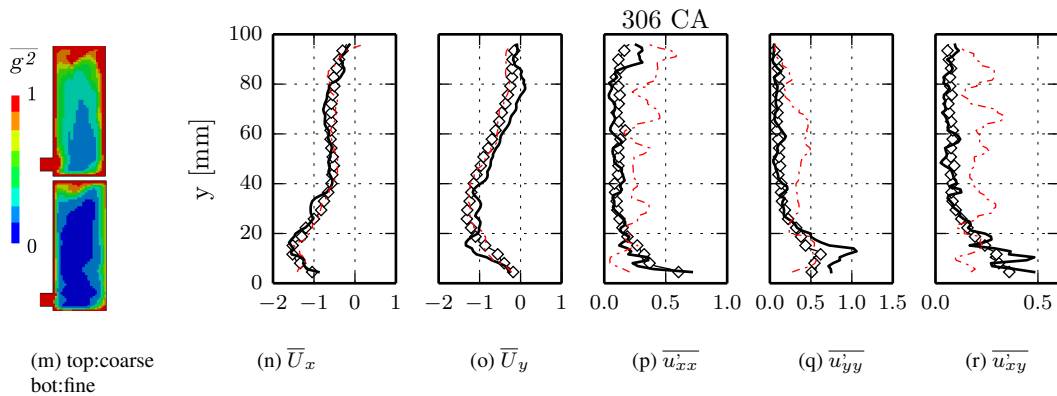
Chapter 5. Validation of the numerical method



Comparison of different turbulence models (coarse grid, CFL<1):  $\diamond$  Exp; — DLRM; - - - LES; - · - ·  $k-\omega$  SST

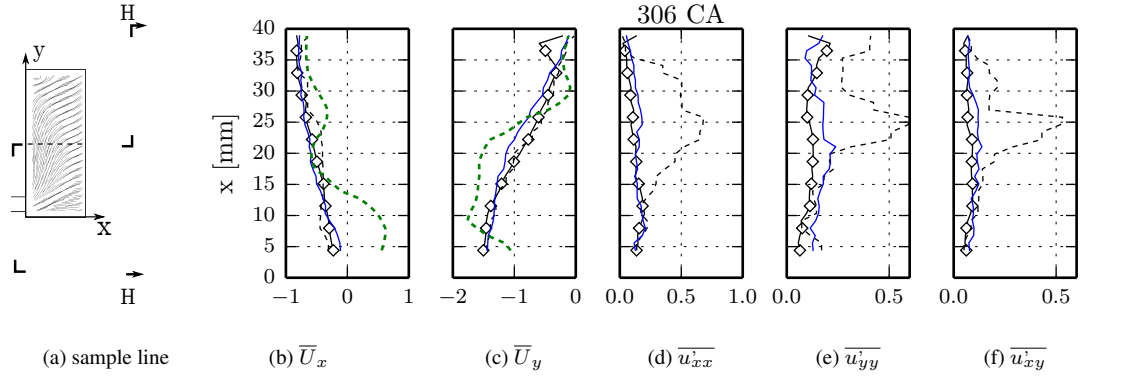


Influence of time step advancement (DLRM, coarse grid): — CFL<1; - - - CFL<5

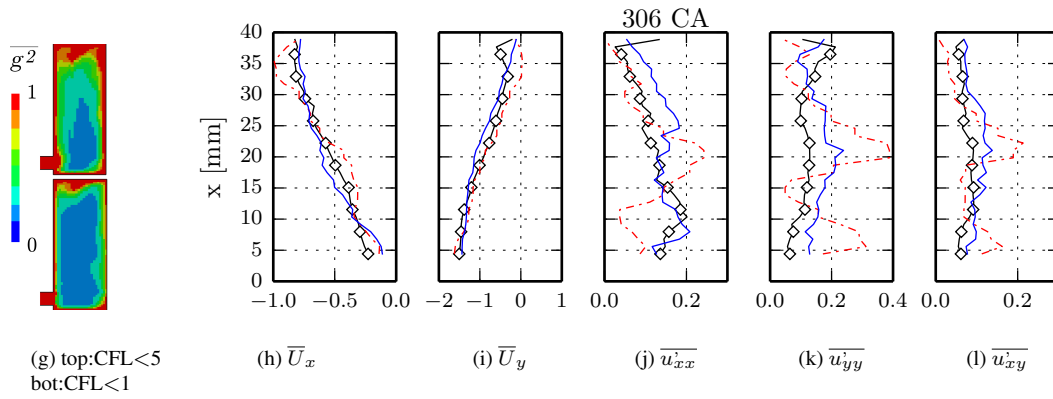


Influence of mesh resolution (DLRM, CFL<5): - - - coarse grid; — fine grid

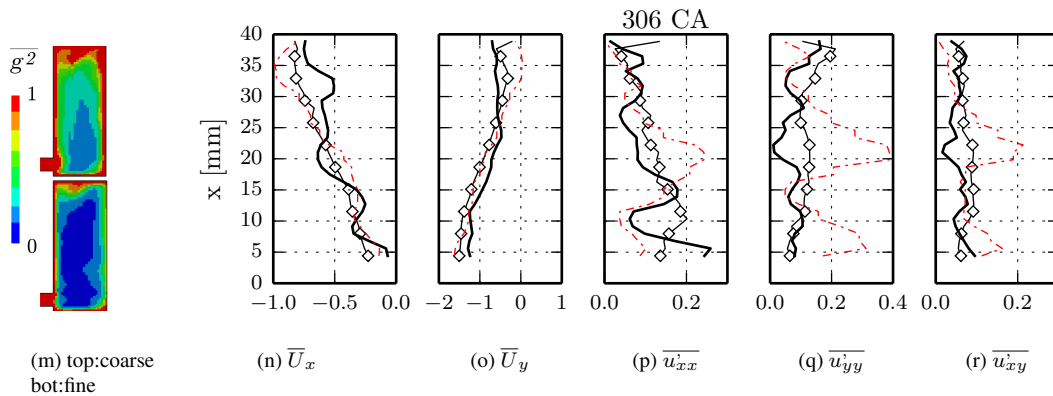
Figure 5.20: Comparison of the phase-average and variance of the velocity field calculated by different turbulence models on a centered vertical line over the mid-cross x-y measurement plane, “uncompressed vortex” case.



Comparison of different turbulence models (coarse grid, CFL<1):  $\diamond$  Exp; — DLRM; --- LES; -.-  $k-\omega$  SST



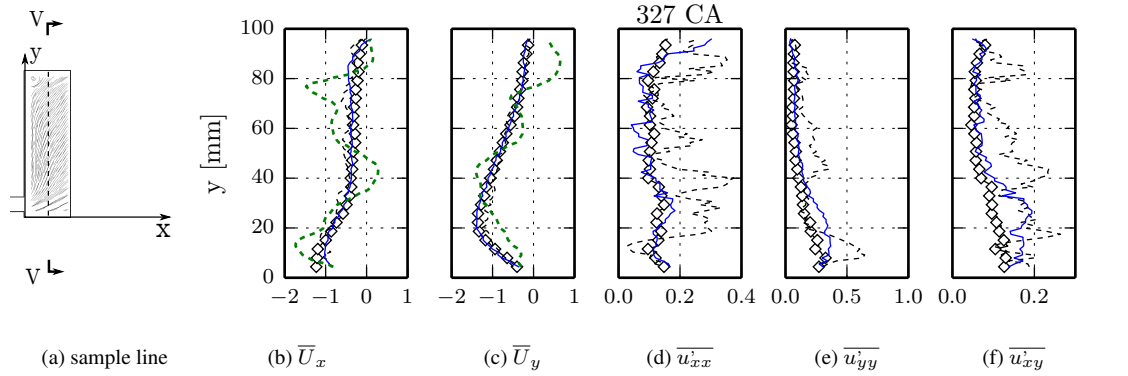
Influence of time step advancement (DLRM, coarse grid): — CFL<1; --- CFL<5



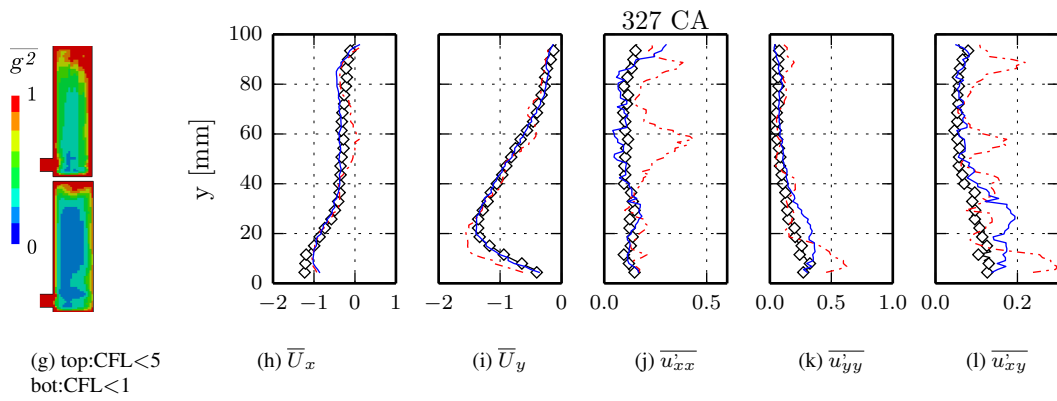
Influence of mesh resolution (DLRM, CFL<5): --- coarse grid; — fine grid

**Figure 5.21:** Comparison of the phase-average and variance of the velocity field calculated by different turbulence models on a centered horizontal line over the mid-cross  $x$ - $y$  measurement plane, “uncompressed vortex” case.

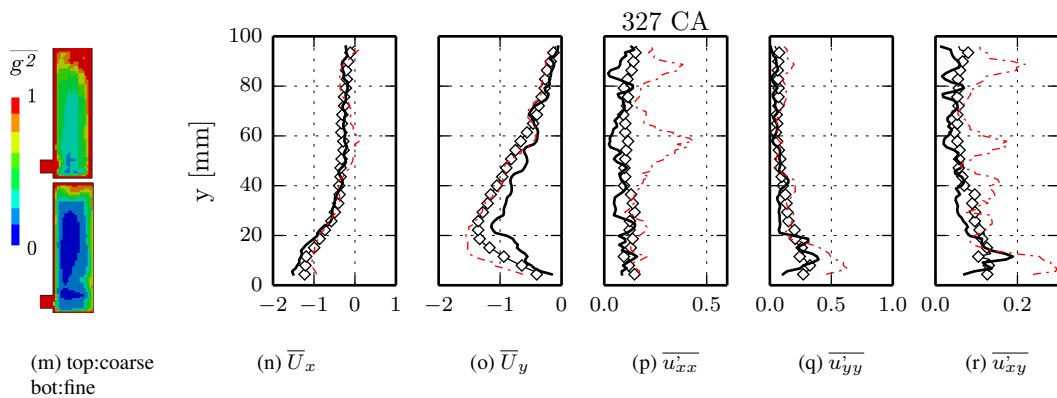
## Chapter 5. Validation of the numerical method



Comparison of different turbulence models (coarse grid, CFL<1):  $\diamond$  Exp; — DLRM; - - - LES; - · - ·  $k-\omega$  SST

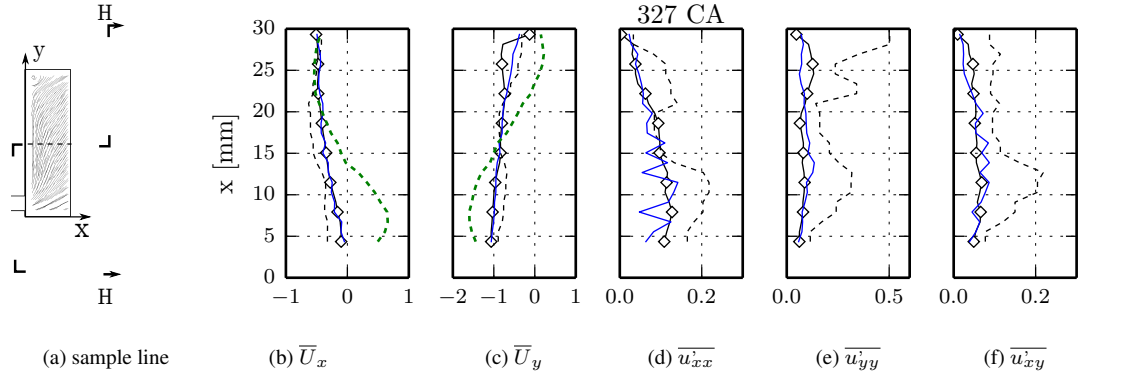


Influence of time step advancement (DLRM, coarse grid): — CFL<1; - - - CFL<5

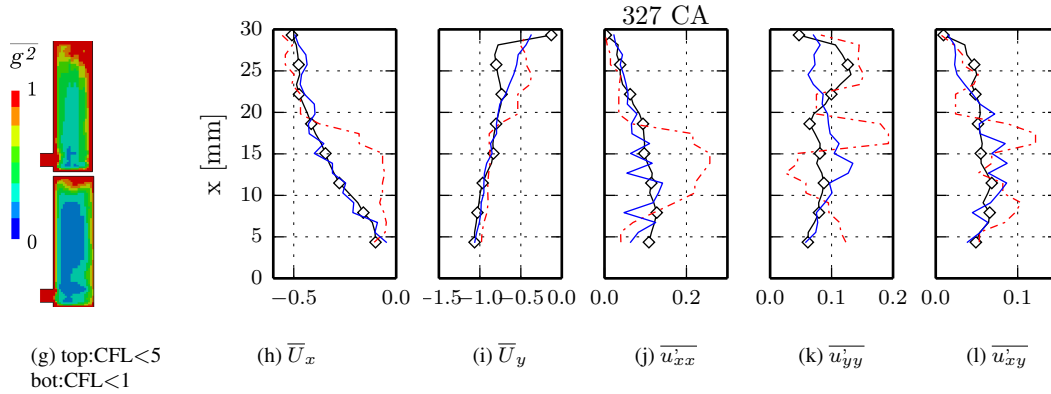


Influence of mesh resolution (DLRM, CFL<5): - - - coarse grid; — fine grid

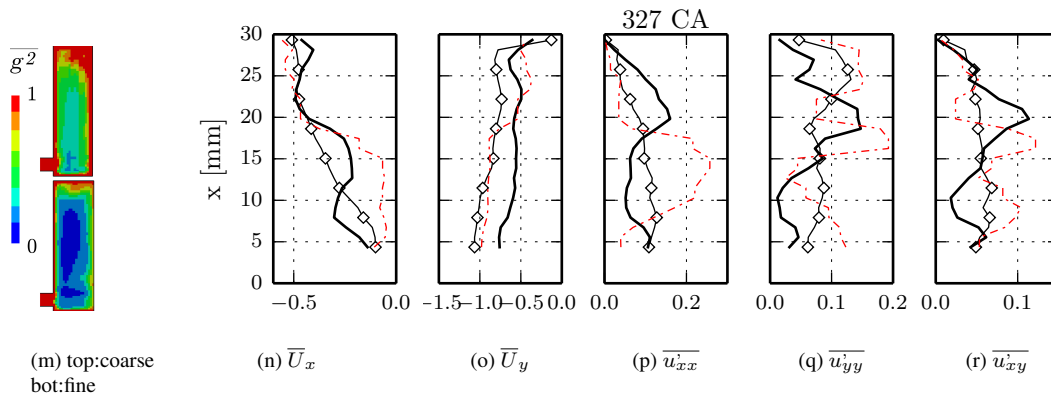
**Figure 5.22:** Comparison of the phase-average and variance of the velocity field calculated by different turbulence models on a centered vertical line over the mid-cross x-y measurement plane, “uncompressed vortex” case.



Comparison of different turbulence models (coarse grid, CFL<1):  $\diamond$  Exp; — DLRM; --- LES; -.-  $k-\omega$  SST

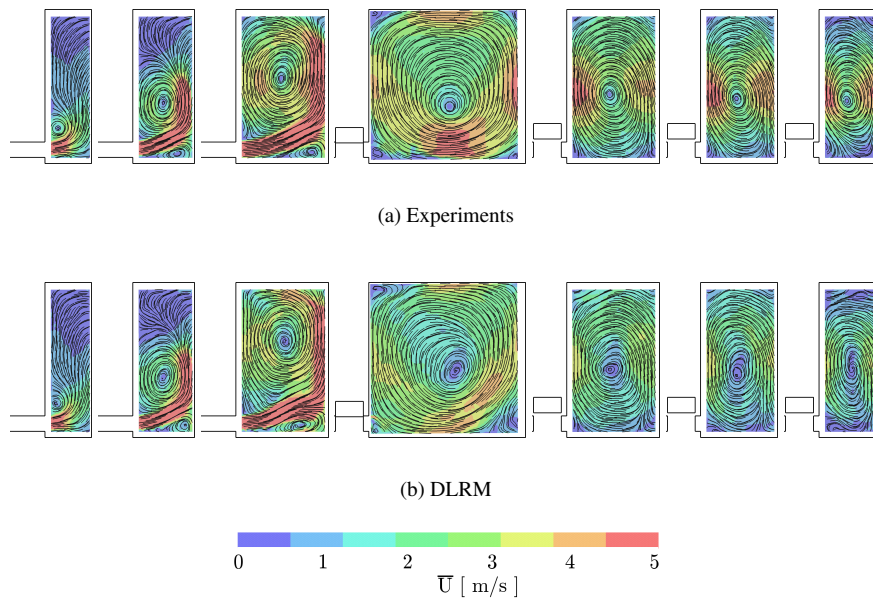


Influence of time step advancement (DLRM, coarse grid): — CFL<1; --- CFL<5



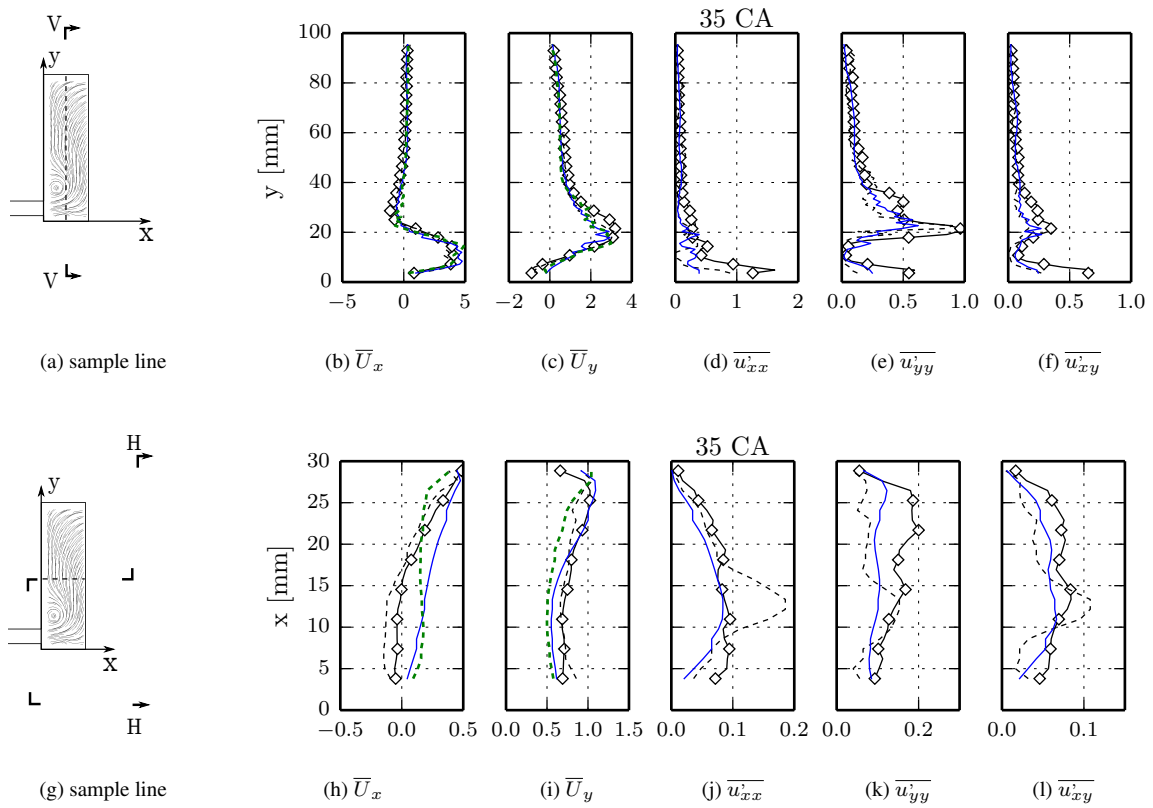
Influence of mesh resolution (DLRM, CFL<5): --- coarse grid; — fine grid

Figure 5.23: Comparison of the phase-average and variance of the velocity field calculated by different turbulence models on a centered horizontal line over the mid-cross x-y measurement plane, “uncompressed vortex” case.



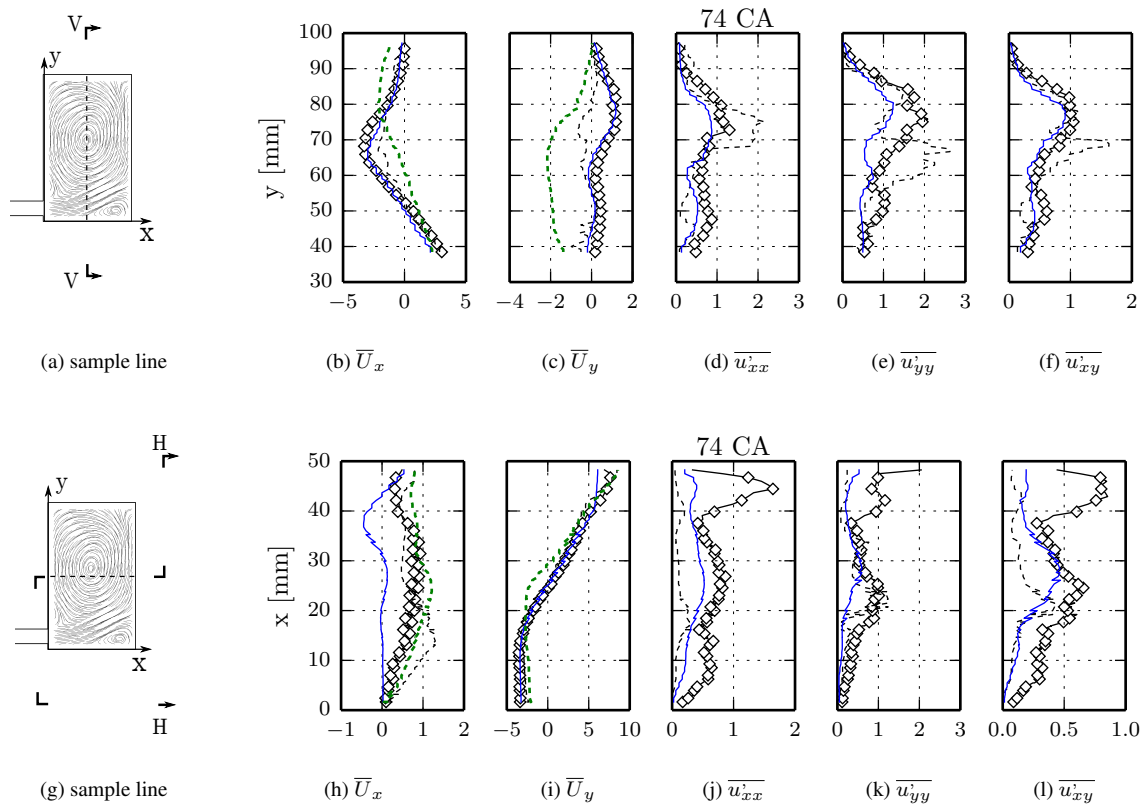
**Figure 5.24:** Evolution of the phase-averaged mean flow on  $x$ - $y$  plane, “compressed vortex” case.: Left-to-right: 35, 57, 90, 185, 278, 293, 310 CA deg. a) Experiments, phase-averaging over 100 PIV realizations; b) coarse grid, DLRM,  $CFL \leq 1$  (phase-averaged over 28 realizations)





Comparison of different turbulence models (coarse grid, CFL<1):  $\diamond$  Exp; — DLRM; --- LES; -.-  $k-\omega$  SST

**Figure 5.25:** Comparison of the phase-average and variance of the velocity field calculated by different turbulence models on vertical and horizontal sample lines of the  $x$ - $y$  measurement plane, “compressed vortex” case.



Comparison of different turbulence models (coarse grid, CFL<1):  $\diamond$  Exp; — DLRM; - - - LES; - · - ·  $k-\omega$  SST

**Figure 5.26:** Comparison of the phase-average and variance of the velocity field calculated by different turbulence models on vertical and horizontal sample lines of the x-y measurement plane, “compressed vortex” case.

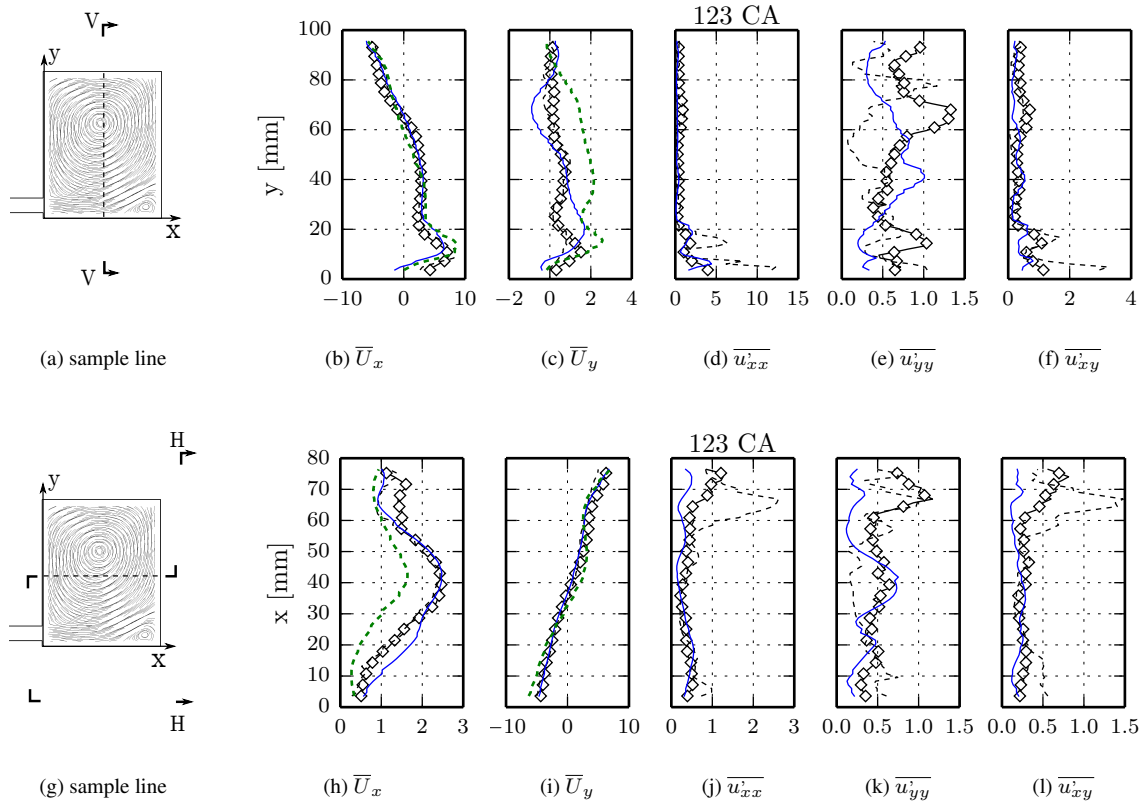
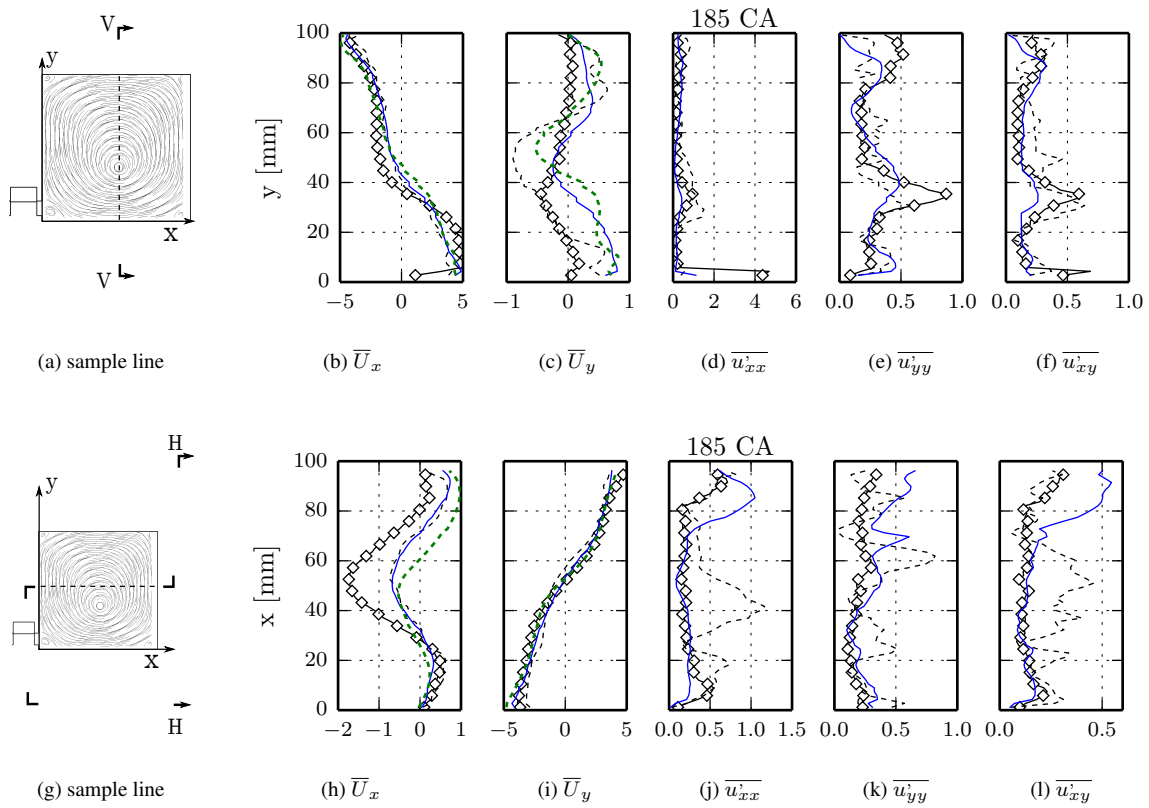


**Figure 5.27:** Comparison of the phase-averaged and variance of the velocity field calculated by different turbulence models on vertical and horizontal sample lines of the  $x$ - $y$  measurement plane, “compressed vortex” case.



Comparison of different turbulence models (coarse grid, CFL<1):  $\diamond$  Exp; — DLRM; - - - LES; - · - ·  $k-\omega$  SST

**Figure 5.28:** Comparison of the phase-average and variance of the velocity field calculated by different turbulence models on vertical and horizontal sample lines of the  $x$ - $y$  measurement plane, “compressed vortex” case.

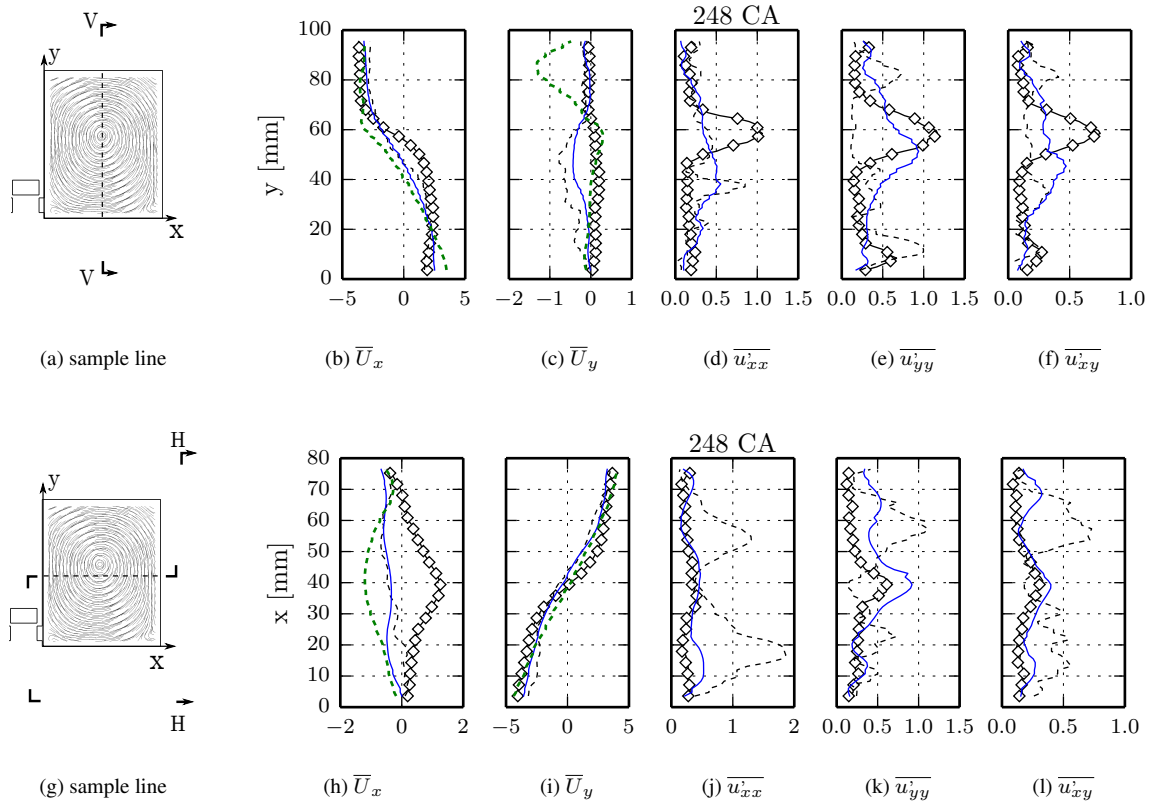
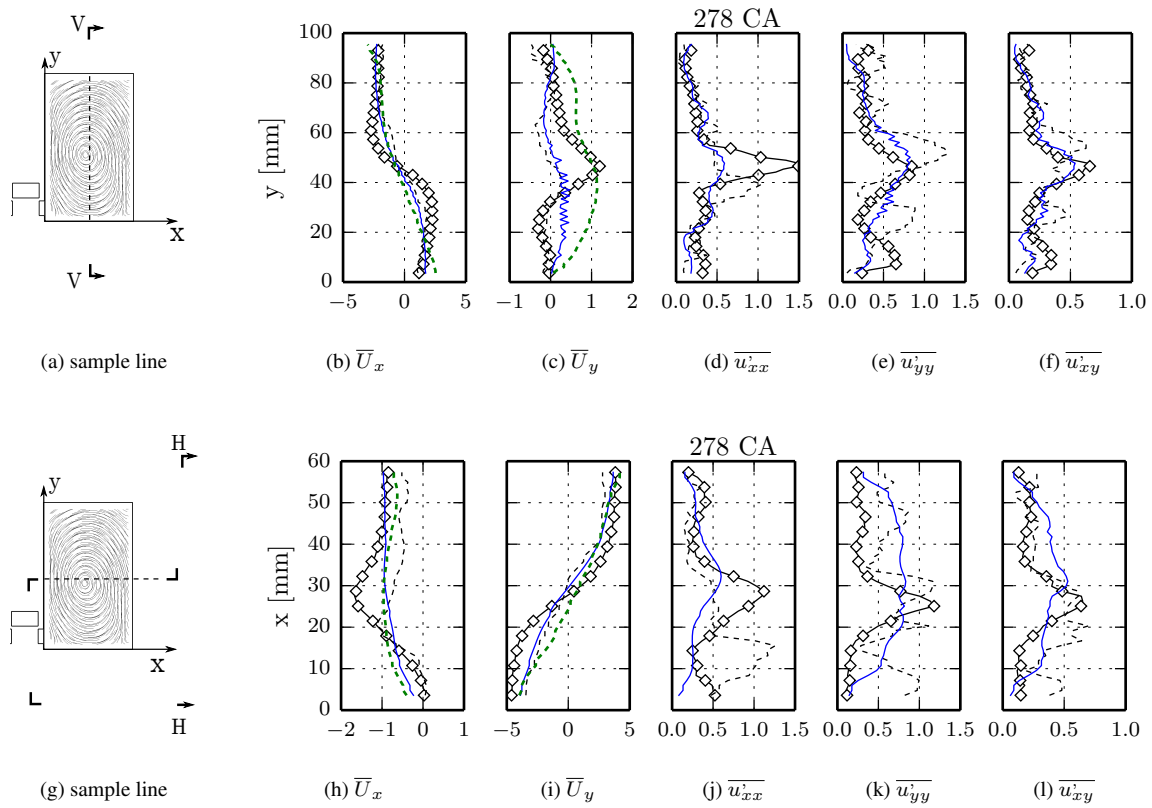


**Figure 5.29:** Comparison of the phase-average and variance of the velocity field calculated by different turbulence models on vertical and horizontal sample lines of the  $x$ - $y$  measurement plane, “compressed vortex” case.



Comparison of different turbulence models (coarse grid, CFL<1):  $\diamond$  Exp; — DLRM; - - - LES; - · - ·  $k-\omega$  SST

**Figure 5.30:** Comparison of the phase-average and variance of the velocity field calculated by different turbulence models on vertical and horizontal sample lines of the  $x$ - $y$  measurement plane, “compressed vortex” case.

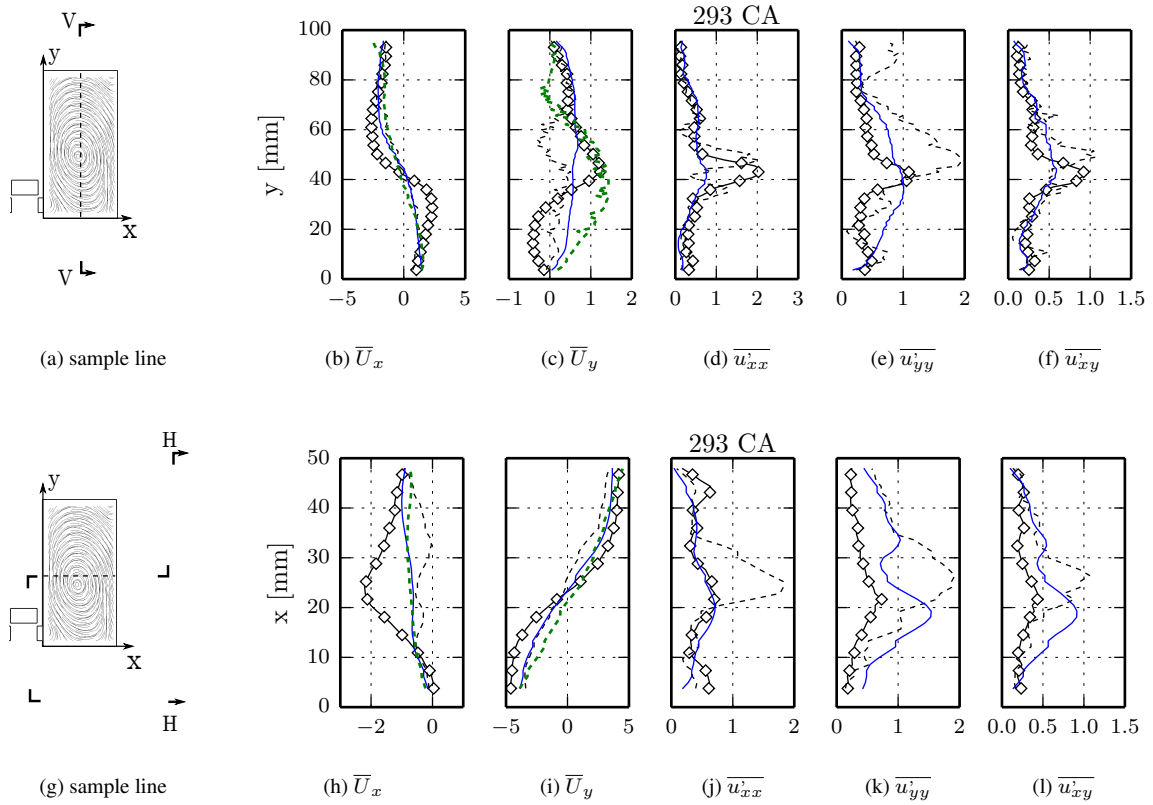


**Figure 5.31:** Comparison of the phase-averaged and variance of the velocity field calculated by different turbulence models on vertical and horizontal sample lines of the  $x$ - $y$  measurement plane, “compressed vortex” case.

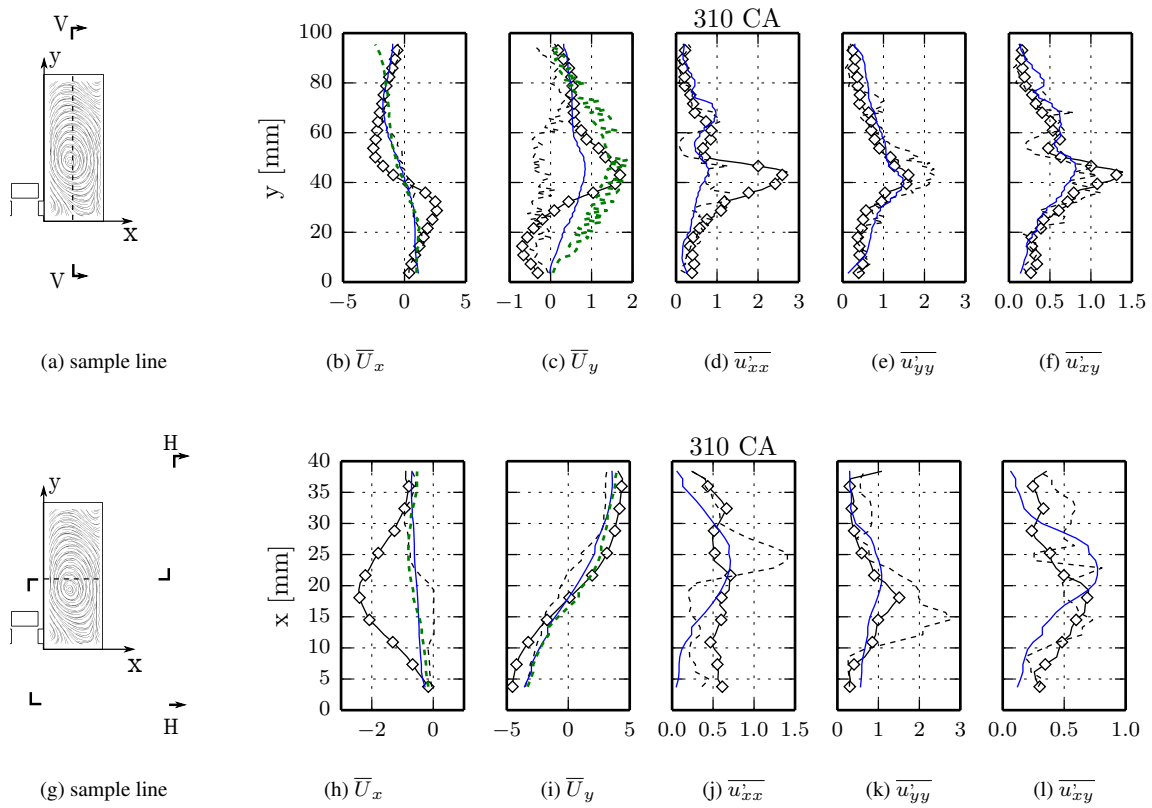
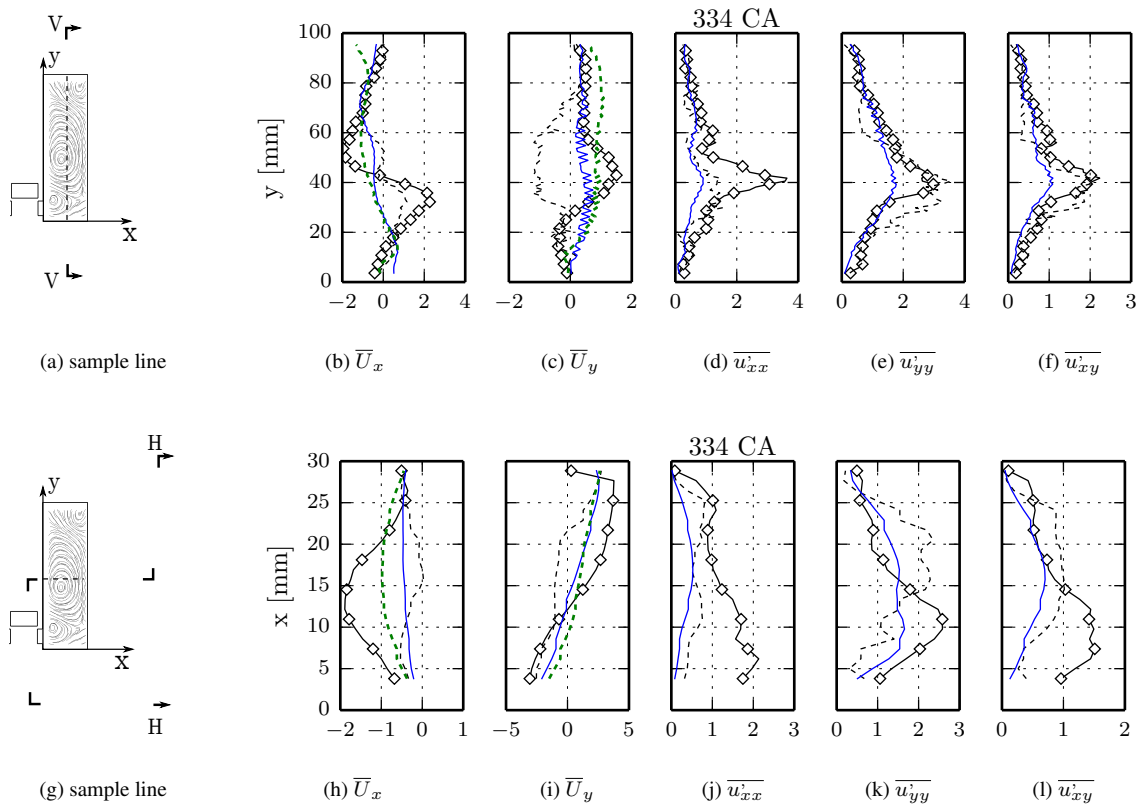


**Figure 5.32:** Comparison of the phase-average and variance of the velocity field calculated by different turbulence models on vertical and horizontal sample lines of the x-y measurement plane, “compressed vortex” case.





Comparison of different turbulence models (coarse grid, CFL<1):  $\diamond$  Exp; — DLRM; --- LES; -.-  $k-\omega$  SST

**Figure 5.33:** Comparison of the phase-averaged and variance of the velocity field calculated by different turbulence models on vertical and horizontal sample lines of the  $x$ - $y$  measurement plane, “compressed vortex” case.

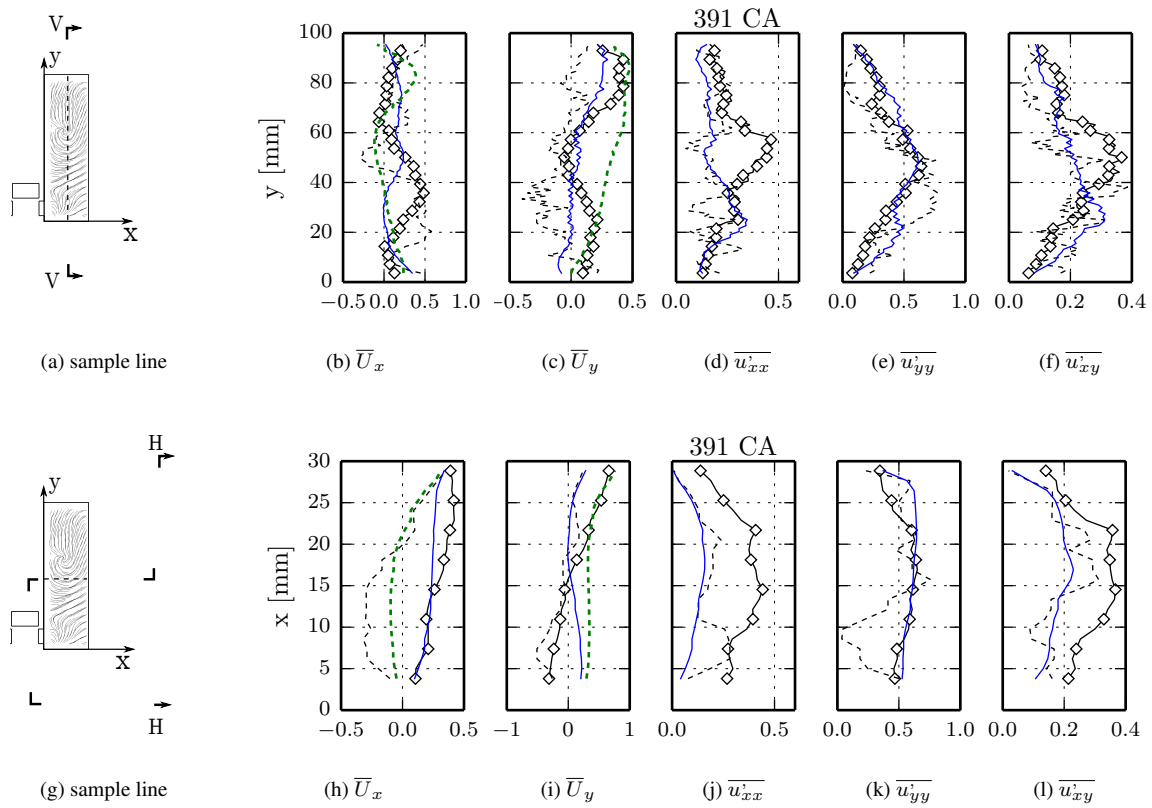
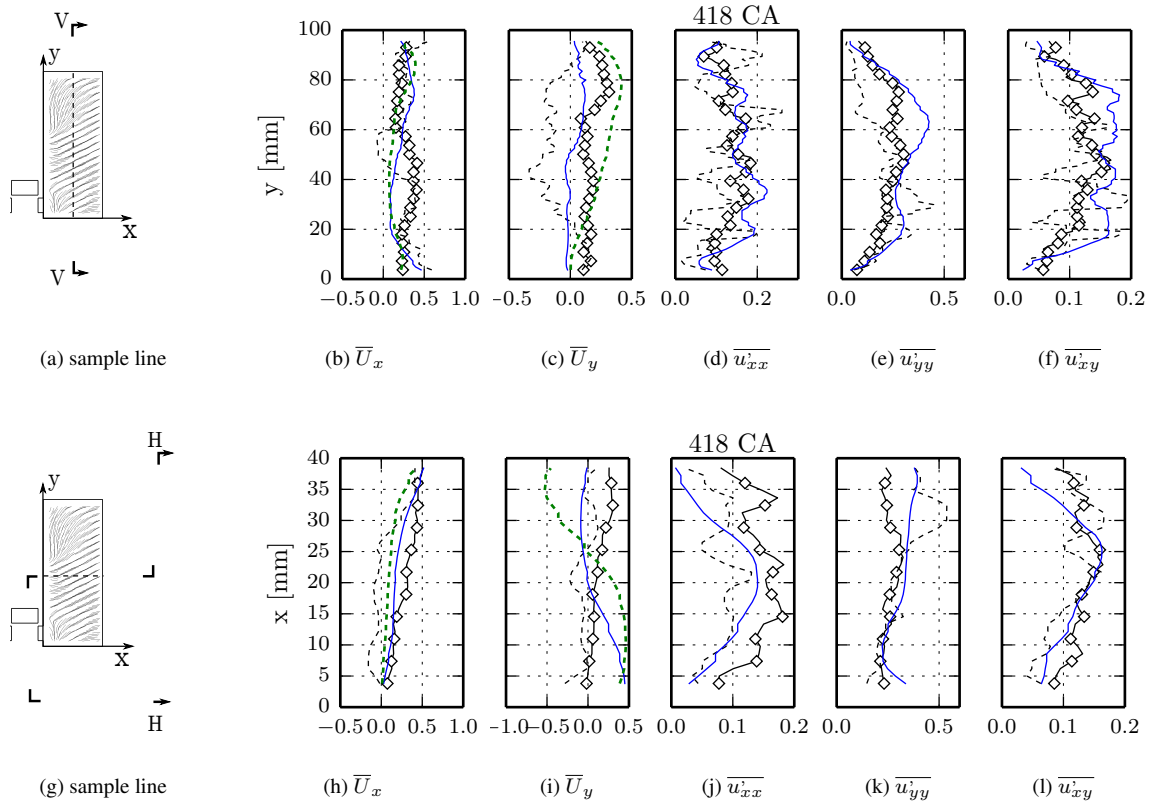


**Figure 5.34:** Comparison of the phase-average and variance of the velocity field calculated by different turbulence models on vertical and horizontal sample lines of the  $x$ - $y$  measurement plane, “compressed vortex” case.



Comparison of different turbulence models (coarse grid, CFL<1):  $\diamond$  Exp; — DLRM; - - - LES; - · - ·  $k-\omega$  SST

**Figure 5.35:** Comparison of the phase-average and variance of the velocity field calculated by different turbulence models on vertical and horizontal sample lines of the  $x$ - $y$  measurement plane, “compressed vortex” case.

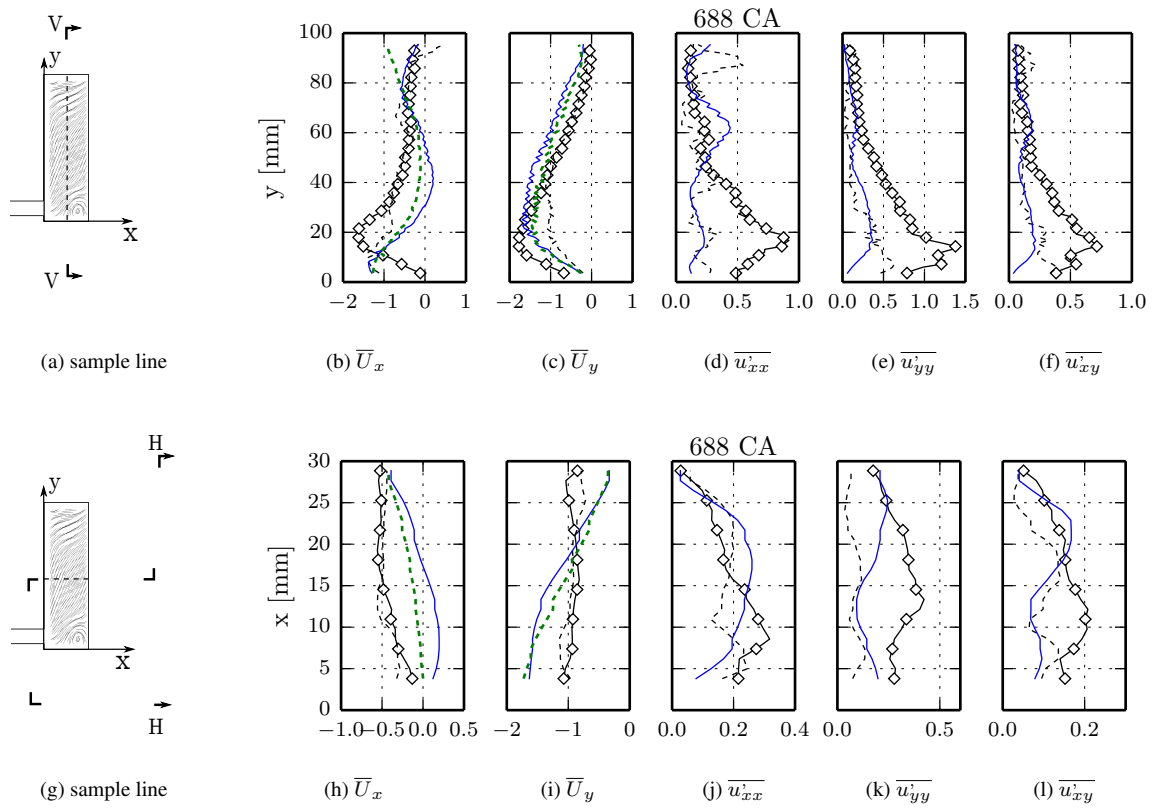


**Figure 5.36:** Comparison of the phase-average and variance of the velocity field calculated by different turbulence models on vertical and horizontal sample lines of the  $x$ - $y$  measurement plane, “compressed vortex” case.

---

# CHAPTER 6

---

## Coherent structure of in-cylinder flow

---

### 6.1 Dynamic system and dimension reduction

---

In the perspective of dynamical systems, turbulent velocity field could be described as function of space and time with (hopefully) complex attractors whose dimension increases with Reynolds number or corresponding turbulence viscosity. In the early work of Landau [42] and Hopf [38], it is envisaged that for dynamic system of the turbulent flow, the first attractor is periodic, followed by quasi-periodic attractors with increasing numbers of independent frequencies. Modern dynamical systems theory also indicates that the flow field corresponds to a phase flow on an  $n$ -dimensional torus in the state (phase) space of the dynamical system. Hopf even proposed a model problem which exhibited just such a bifurcation sequence, which is sometimes referred as “route to chaos”, although later it is realized that quasi-periodic flows are not strongly chaotic, since the solutions do not depend sensitively on initial conditions. More importantly, Hopf also proposed that “to the flows observed in the long run after the influence of the

initial conditions has died down there correspond certain solutions of the Navier–Stokes equations. These solutions constitute a certain manifold in phase space invariant under the phase flow. Presumably owing to viscosity a **finite number of dimensions**” [37,38].

Based on Hopf’s theory on possible low dimension description of the turbulent system, Ruelle and Takens observed that the quasi-periodic flows are not structurally stable and so shall not be regarded as an general attractor. They proposed another example of a structurally stable attractor that can appear after two or three quasi-periodic bifurcations, which lives on a torus of only four dimensions. However, none of these works attempts to make connections between a particular flow modelled by the Navier-Stokes equations with specific boundary conditions and the dynamical systems which exhibited quasi-periodic or strange attractors. Lorenz [46], however, provided an example of drastic truncation to three Fourier modes of the coupled Navier–Stokes and heat equations in a two-dimensional layer. The strange attractor he found, though far beyond the Rayleigh number range in which his truncation was reasonable, is named as the Lorenz attractor [37].

The potential of a low-dimensioned description, along with the evidence that coherent structures [43] exist in the turbulent flow made the viewpoint of dynamical systems theory be acknowledged as an useful tool for the study of fluid systems. This is especially true for closed system (eg. IC engine) where relatively only a few spatial modes are active. Holmes *et al.* further proposed that “a low-dimensional dynamical systems can also provide models for, and hence contribute to the understanding of, certain fully developed, open turbulent flows” [37]. He suggested that 10-100 ordinary differential equations, which is very “low” in the context of fluid dynamics, could capture the key behaviours of flows with predominant coherent structures. To make sure that fluid velocity field in physical space is still represented in the phase space of the dynamical system, a proper flow decomposition technique is necessary so that at least certain “modes” or empirical eigenfunctions that carry the greatest kinetic energy on average are retained. This promotes the application of proper orthogonal or Karhunen–Loève decomposition (POD) for the study of turbulent unsteadiness, which would be discussed in the next section.

## 6.2 Proper orthogonal decomposition

### 6.2.1 Concept and equations

Besides classic descriptive statistics (mean, variance and higher order moments), another useful tool in the field of turbulence description has been found in Proper Orthogonal Decomposition (POD) [11, 37]. POD decomposes realizations of a field (in current study the velocity field) in physical space into a linear combination of orthogonal bases called POD modes. For each POD mode, the weight coefficient represents the energy that the current mode contributes to the original realizations, while the vector basis shows the shape of that mode. POD holds several advantages over other method to extract information from dynamic system. Firstly, it is mathematically well defined, which helps to exclude arbitrariness in the separation of energy scales. Secondly, a clear hierarchy between coherent structures is naturally identified, for the sequence of POD mode is arranged so that the more energy-containing modes (with higher eigenvalues) are in front of less energetic ones.

As any linear decomposition procedure applied on dynamic systems, POD provides a series of energy containing “modes”, each of them could then be decoupled into the product of a scalar and a normal basis function, as shown in Eq. (6.1):

$$\mathbf{u}(\mathbf{x}, t) = \sum_{k=0}^M a(t)^{(k)} \cdot \Phi(\mathbf{x})^{(k)} + \mathbf{r}^{(k)} \quad (6.1)$$

where  $M$  is the number of extracted POD modes.  $a(t)^{(k)}$  are functions of time and they are related to the kinetic energy contained in the corresponding POD mode.  $\Phi(\mathbf{x})^{(k)}$  is the normalized basis, which provides information on the “shape” of the current POD mode, and  $\mathbf{r}^{(k)}$  is the residual motion.

By definition, POD modes are sorted in decreasing order, so the energy contained in any given mode is always higher than the one in the following mode. It could be further proved that such decay of energy has its fastest rate only when POD is used: compared with other decomposition methods and for a given number of modes kept for analysis, POD retains the highest percentage of the information of original system, or in other words, for a given threshold percentage of the information that must be retained,

POD requires the smallest number of modes. This is usually termed as the optimality of POD [11], which is the most important reason why POD is used in this study over other decomposition methods.

While quite expensive when computed with formal methods, POD has an affordable cost when calculated by the “Snapshot method” developed by Sirovich [72], thus it has become a common tool for the analysis of engineering problems since the number of realizations (usually time steps) are much lower than the dimension of spatial locations (usually grid points). For the POD of engine flow, there are basically two strategies to taking account the flow periodicity and hence to organize of the snapshots, namely “Phase-dependent” and “Phase-invariant” POD. The former computes POD mode for every phase angle of the problem, thus the number of snapshots equals the number of available periods. In “Phase-invariant” POD, the flow field is linearly transformed among all phase angles so the snapshot matrix contains all crank-angle positions.

For both “Phase-dependent” and “Phase-invariant” POD, the snapshots are computed as follows: Let  $M$  be the number of realizations of the flow field and  $R_{ij}$  be their correlation tensor, defined as:

$$R_{ij} = \frac{1}{M}(\mathbf{u}(\mathbf{x}, t_i) \cdot \mathbf{u}(\mathbf{x}, t_j)) \quad \text{with } i, j = 1 \dots M \quad (6.2)$$

where “ $\cdot$ ” denotes the inner product operator. It’s worth mentioning that for both original or “snapshots method”, definition of the inner product is maybe the most important choice in POD. Since “energy” is defined through inner product in the space of POD, its formation should be complied with the concept of energy in the physical space. For current study, since  $\mathbf{u}(\mathbf{x}, t_i)$  stands for an “macro-vector” defined on the set of spatial locations, whose elements are the local velocities which are also vectors, the inner product between two “macro-vectors” are defined as the sum of all the inner products between local velocities. Compared with treating the three dimensions of the velocity field separately hence applying POD on each direction individually, which is sometimes the common practice, such definition retains the original definition of kinetic energy in the physical point of view, so the three-dimensioned nature of the coherent structures is kept implicitly.



To compute POD one must first solve the following eigenvalue problem:

$$\mathbf{R}\mathbf{A}^{(k)} = \lambda^{(k)} \mathbf{A}^{(k)} \quad (6.3)$$

to obtain  $M$  eigenpairs  $[\lambda^{(k)}, \mathbf{A}^{(k)}]$ . The eigenvalue  $\lambda^{(k)}$  directly represents the energy content of the  $k$ -th mode. The POD modes  $\Phi^{(k)}(\mathbf{x})$  are computed as:

$$\Phi^{(k)}(\mathbf{x}) = \sum_{m=1}^M [A_m^{(k)} \mathbf{u}^{(m)}(\mathbf{x})] \quad (6.4)$$

while the time-varying coefficient are calculated by projecting the POD modes onto the original snapshot:

$$a^{(k)}(t_i) = (\mathbf{u}(\mathbf{x}, t_i), \Phi^{(k)}(\mathbf{x})) \quad (6.5)$$

where  $i$  is the temporal index.

### 6.2.2 POD on engine flow

Applying POD into the study of engine flow is typically quite expensive, as the engine flow is periodic yet undergoes cyclic variation. A considerable amount of engine cycles have to be examined for an converged POD analysis. Driven by the desire of a low-dimensional description of the complex in-cylinder turbulent processes, most of the early works focused on the PIV data measured experimentally, since the price of scale resolved engine simulation is reduced to a realizable level only recently.

Raposo *et al.* [66] used the PIV measurement of the velocity fields from an steady state water analog test engine for the study of coherent structures inside engine flow. Instead of air, the test engine use water for the working fluid, and only one “crank angle” has to be measured since both the valve and piston are kept unmoved during the experiment. Nevertheless, they found that for the flow field under study, the leading POD corresponds closely to the ensemble mean flow, and the following POD mode clearly identifies the coherent motion which “superimposes on the mean flow to create a varying mean flow field”.

Roudnitzky *et al.* [68] implemented the POD technique to PIV measurements obtained in the tumble plane of spark ignition engine flow. They proposed that the POD

modes of the in-cylinder flow could be decomposed into 3 parts, namely the average part, a coherent part and a random Gaussian fluctuations part. The last part should be isolated from flow analysis since it contains information regarding only small amplitude background fluctuations, which are homogeneous and satisfy the Gaussian properties.

Chen *et al.* [16] performed phase-dependent POD on two 200-cycle PIV data sets of in-cylinder flows. In their work, they raised the question of whether POD should be performed with prior subtraction of the ensemble mean flow, and he also found that the first POD mode is nearly identical to ensemble-averaged flow. However, they suggested not subtract phase-averaged flow prior to POD thus the POD coefficients could reveal the extent to which the mean flow is present and its cycle-to-cycle variability.

As well resolved LES becomes more affordable for the engine simulation in recent years, researchers turn to perform POD on both simulation and experiment results since the former provide much more accessible flow information. To lower the requirement on the number of cycles analysed and a better reveal the temporal correlations, phase-invariant POD had been developed and applied by Liu and Haworth [44] for the analysis of periodic engine flows, showing the economy of their method to describe the energy content and level of organization of the flow at different crank angles.

The economy of phase-invariant POD is favoured by Fogleman *et al.* [25] in their study on engine flow acquired by both experiment measurement and LES. Both phase-invariant and phase-dependent POD are applied in their study. Although experiment and simulation results are acquired on prototype engines with different geometries, they found that the energy cascade of POD modes predicted by simulation agrees reasonably with experiment data, and that vorticity predominately aligned with the plane orthogonal to both the plane of maximum tumble and the piston face.

Liu *et al.* [45] also adopted both phase-invariant and phase-dependent POD to LES results from a four-stroke flat head engine. They echo with the finding that the leading POD mode corresponds essentially to the ensemble-averaged velocity, and that quantification of CCV can be extracted through phase-invariant POD. Recently, however, Montorfano *et al.* demonstrated that phase-dependent POD can be used instead to detect and track turbulent structures that elude both classical descriptive statistics and phase-independent POD, but are indeed responsible of turbulence-driven CCV [55,57].

As most of these studies indicate that coherent structures could be identified objectively by POD, interpolation of the physical explanation of these structures remains unclear. Apart from a common connections being made between the leading POD mode and the ensemble-mean flow, motions in the higher mode, whose existence is generally acknowledged yet being explained by various assumptions under different flow conditions, require more careful and comprehensive studies on their nature. Besides, for the comparison between simulation and experiment results, typically conducted by referring to only the eigenvalues, rarely did the eigenvectors (empirical eigenfunctions) been investigated simultaneously between simulation and experiment, which indeed might provide more quantitative insights into the precision of numerical method.

---

### **6.3 Results and analysis**

---

POD analysis focuses on the flow field of “uncompressed vortex” case. Since the in-cylinder flow field is driven by periodically moving boundaries, POD snapshots are collected on the basis of the phase-dependent strategy: The number of snapshots, or POD modes, equals the number of engine cycles, rather than available time steps [44, 57]. To keep the consistency of the analysis between simulation and experimental data, 3-D simulation results are mapped onto the 2-D PIV grids on which velocity fields were measured. Moreover, the number of POD modes extracted from experimental data is limited to 28, which equals to the number of available simulation cycles, although up to 120 cycles were sampled during the measurement campaign.

Fig. 6.1 shows the eigenvalues  $\lambda^{(k)}$  of the first four modes on ten crank angles for both experiments and simulations. The agreement between predicted and measured values is very good, especially for first mode (which would then be referred to as “Mode 0”, and “Mode 1”, “Mode 2” ... for the following modes). Mode 0 has been found to be closely linked to the ensemble mean, thus the very good match between simulations and experiments is not surprising, for DLRM is capable to predict the mean flow as shown in previous chapters. For all POD modes, magnitudes of eigenvalues evolve with almost the same trend, showing clearly 2 maxima around CA=90° and CA=245°, and 1 minimum around top dead center. This behaviour can be related to the engine piston speed, which is the only momentum source in the present case. Piston speed

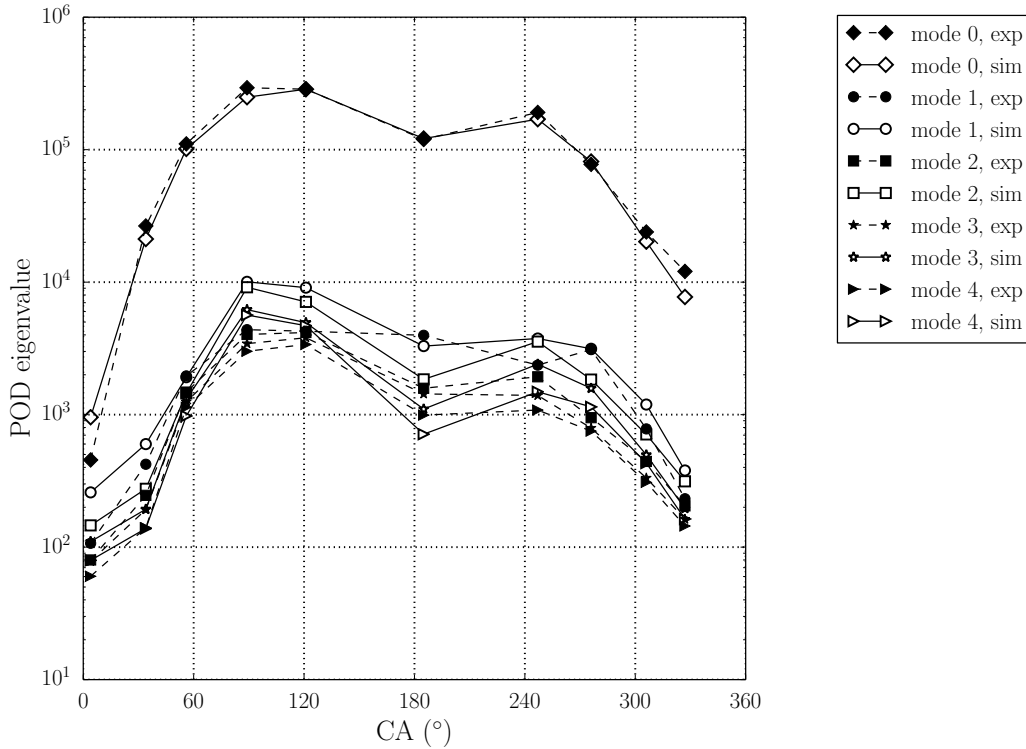


Figure 6.1: Eigenvalues of different POD modes, “uncompressed vortex” case. - - - experiments; — DLRM

reaches its maximum at about half of the stroke and it is not surprising that the flow maximum energy exhibits the same trend.

Distribution of energy among different modes is shown in Fig. 6.2. To have a uniform and proper comparison between modes, eigenvalues are normalized by the mode global energy content. A very fast decay is observed from mode 0 to mode 1, with a difference of about 2 orders of magnitude for all crank angles. Close to TDC and BDC the decay is slower, whereas it is maximized in most energy-containing modes. The reason is that the flow fields around  $CA=90^\circ$  and  $CA=270^\circ$  are not only more energetic, but also more organized, due to the strong coherent structures generated. For all crank angles there is a very good match between simulation and experiment, which represents a further validation of the model that is able to reproduce not only the macroscopic flow features, but also the energy transfer between different length scales on the integral level.

Although the dominance of mode 0 is welcome for simulation, suggesting that turbulence intensity is not of great magnitude, which in turn may reduce the error from turbulence model, it should be noticed that such fast cascade may also suggest that the flow field studied is too much simplified. An engine speed at around 200 RPM might be too low to generate well establish turbulence, besides, a constant open valve could over simplified the flow field, giving the piston motion an overly dominant role. Nevertheless, at least for the engine in current study, decay of energy is slowed down right after mode 1, with neighbour modes usually have eigenvalues of same orders of magnitude. If it is true that higher order POD modes turn to represent more information of higher frequency, smaller scale turbulence structures, such trend echoes with the observation of energy cascade of turbulence, at least in the statistic point of view: small eddies, been more random and chaos, must absorb kinetic energy from larger ones, which in chain is powered by macroscopic, and usually organized driving force (like the moving piston in current case).

As eigenvalues provide an qualitative measurement of the integral kinetic energy contains in different flow structures, eigenvectors are more representative of the flow structure itself. Since direct comparison of the eigenvectors between the results of simulation and experiment is rarely reported in the literature, we shall take a look at them in more detail.

Similar to the post-processing of the mean velocity in the previous chapter, the trajectories of the eigenvectors from the first two POD modes are compared in Fig. 6.3. For better clarity, local magnitudes of the eigenvectors are re-normalized from 0 to 1. This should not bring inconsistency since by definition, POD eigenvectors are already normalized and their integral values over the domain are equal to unity.

For all crank angles the agreement between simulation and experiment in mode 0 is very good. This again confirms the close relation between the leading POD mode and the ensemble-averaged field, as it is already shown in the previous chapter that the mean flow is well predicted by the hybrid turbulence model. In fact, it could be proved that if the integral kinetic energy stays unchanged between different physical realizations, POD Mode 0 of a scalar field converges exactly to the mean value. Admittedly, the application to vector field is not straightforward, however for the flow field in current

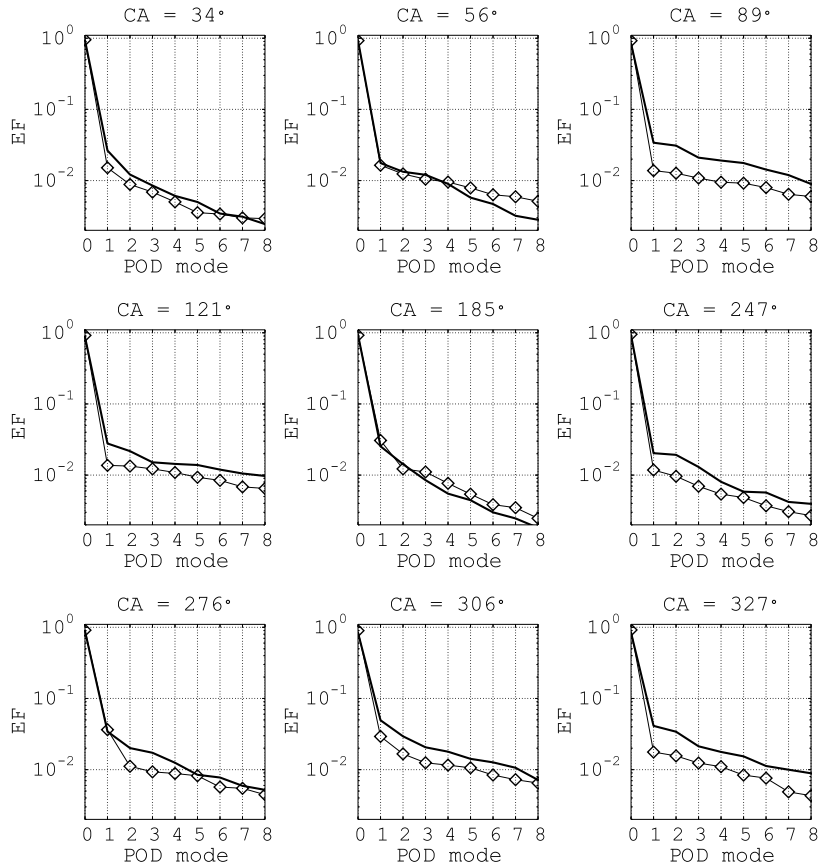


**Figure 6.2:** Energy fractions contained in different POD modes, “uncompressed vortex” case.  $\diamond$  Experiments; — DLRM

study the resemblance is quite close.

More interesting considerations can be done for higher-order modes. By higher it means Mode 1 and Mode 2, since residual modes contain little kinetic energy, as shown by the energy cascade plotted in Fig. 6.1. As a matter of fact, even Mode 2 contains very limited fraction of energy during the entire engine cycle, and it is admitted that the resemblance between simulation and experiment data at Mode 2 justifies little interest for any quantitative investigation.

We shall then focus our attention to eigenvectors of Mode 1, which clearly do not maintain the almost identical agreement as in Mode 0. However, if one compare the eigenvectors of Mode 1 and 0 together, one important correlation in terms of spacial distribution is that the magnitude of Mode 1 typically peaks around the transition area connecting the coherent structures of the mean flow (Mode 1). Apart from  $CA = 34^\circ$ , during the intake stroke ( $56^\circ$ ,  $89^\circ$  and  $121^\circ$ ), the major mean flow structures are the

tumble motion and the recirculation vortex. since they rotate in opposite directions, it is assumed that their competition with each other generates the quasi-vortex motions in Mode 1, which are less organized hence could not maintain itself in the mean flow. For obvious reason, those quasi-vortex motions are typically located around the lower right part of the cylinder, where they gain energy from more organized flow structures.

The contour of eigenvector at  $CA = 34^\circ$  supports such assumption, since at the early stage of intake stroke, the recirculation vortex in the mean flow is not formed or in very low magnitude by itself, so the quasi-vortex motion could not be found at this crank angle either. Instead, the peak of Mode 1 is closer to the connecting region between the initial tumble vortex and the inlet jet.

Situation in the the exhaust stroke ( $CA = 276^\circ, 306^\circ$  and  $327^\circ$ ) further confirms the competition assumption. In the initial stage ( $CA = 276^\circ$ ) the major flow structure in the mean flow is the outlet and the rotation vortex in the lower middle part of the cylinder, and around their connecting region there exist two counter rotating quasi-vortex structures. Similarly, the strength of those quasi-vortices get magnified where the coherent motions in Mode 0 compete with each other. A more evident observation is that at  $CA = 276^\circ$ , quality of simulation results reported in the previous chapter is much less satisfactory compared with other crank angles, which echoes with the prediction of the eigenvector of Mode 1: Both simulation and experiment data exhibit the structures of two counter rotating quasi-vortices, however their locations are quite different, which to some degree also deteriorate the prediction of the mean flow, as shown in both Fig. 6.1 and Fig. 5.7.

To briefly conclude the POD analysis conducted in the thesis study, it is further confirmed that the leading POD mode corresponds almost identically to the ensemble mean flow in the situation that different physical realizations have similar integral kinetic energy. Not only could POD provide a criterion for the validation of the simulation results, but it also helps gain more insight into the origins of the errors of the numerical method under investigated. Moreover, for the identification of the coherent motions (structures) of in-cylinder flow, evidences indicate that competitions of the flow structures in the more organized mode could potentially generate coherent motions in the following modes, which are obviously more transient however could be identified

by means of POD.

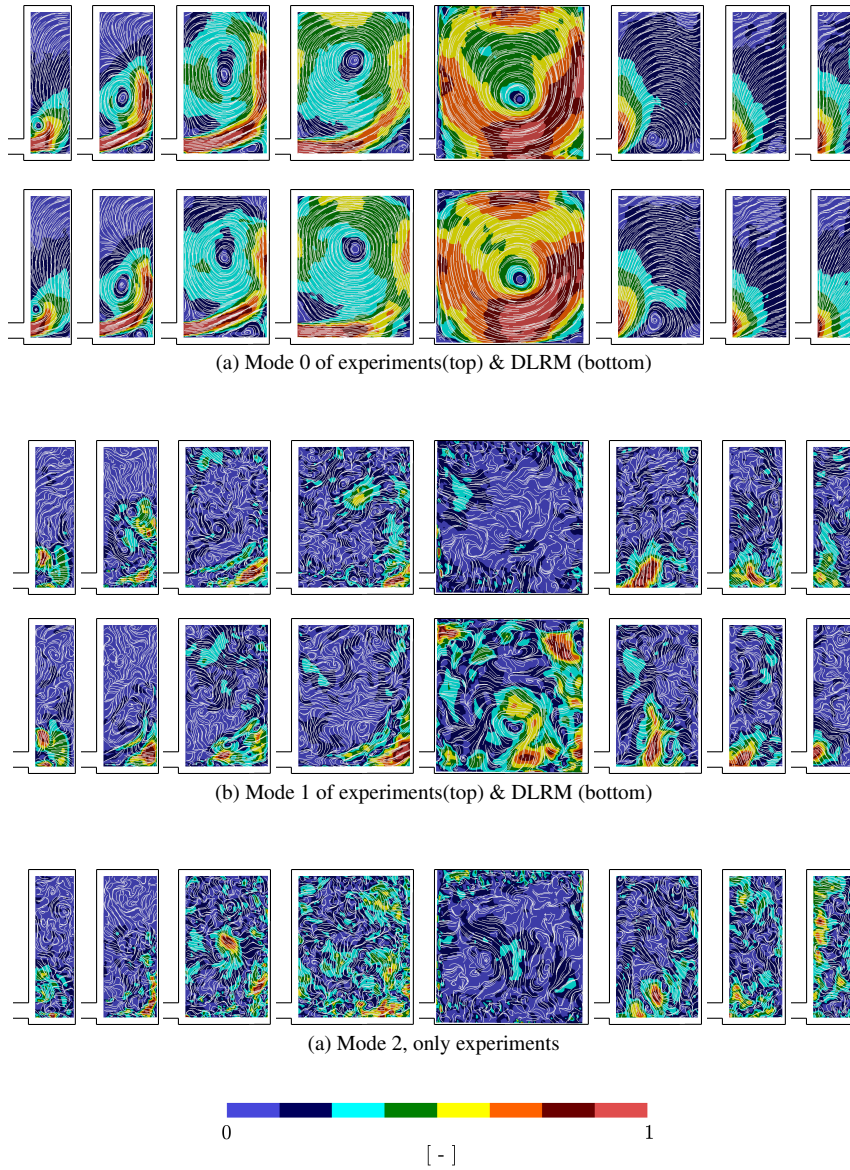


**Figure 6.3:** Normalized eigenvectors of the first three leading POD modes at (left to right): 34, 56, 89, 121, 185, 276, 306, 327 CA, “uncompressed vortex” case.



---

# CHAPTER 7

---

## Conclusion

---

**I**NVESTIGATION into the turbulent unsteadiness of the engine flow requires scale resolving simulation methods that could study the geometrically complex and high-dimensional dynamic system with sufficient numerical precision and affordable computational cost.

The reported thesis work proposes a solution to use a hybrid RANS/LES turbulence model for CFD study of IC engine. Coupled with an enhanced dynamic meshing strategy and proper numerical set-up, the proposed scale resolving model draws a critical balance between the low computational cost of RANS and the resolving capability of LES. Thanks to its cost-effective nature, flow decomposition based on multi-cycle realizations could be conducted on high-fidelity experimental measurement and simulation results simultaneously.

The proposed hybrid turbulence model is the latest development of dynamic length-scale resolution (DLRM) [63], which adjusts its filtering behaviour dynamically

based on the comparison of local resolvable length scale  $\ell_t$  and the estimated turbulence integral length scale  $L_t$ . The renewed definition of  $\ell_t$  treats spatial and temporal resolutions separately, which allows more robust modelling behaviour under different numerical set-up hence the improved adaptivity to coarse mesh and large time step.

Enhancement of the dynamic mesh strategy of the open sourced finite volume CFD library OpenFOAM<sup>®</sup> focuses on the optimization of COUPLING/DECOUPLING algorithms of the mesh interfacing technique `sliding interface`. Run-time topology changes are triggered only when necessary so that renumbering of the grid points is avoided during the time steps when the sliders are not coupled or have no relative displacements.

Validation of the turbulence model and dynamic mesh strategy on an optical test engine confirms the advantage of hybrid turbulence method when simulation is performed on considerably coarse mesh which typically does not satisfy the requirement of conventional “fully resolved” LES. Besides, grid and time step dependency studies also suggest that the simulation results of the proposed hybrid model benefits from a refined numerical resolution even on the very coarse range of spatial resolution far from “inertial sub-range”, which is the main interest of the thesis study.

The POD analysis on the flow field being investigated provides a dynamic system perspective to the understanding of turbulent unsteadiness. After a proper definition of inner product operation in the modal space, it is realized that for the quasi-engine flow without compression, most of the kinetic energy is contained in the ensemble-mean flow, which corresponds closely to the leading POD mode. Further to that, evidence of the competing effect between the mean flow structures is identified in the higher mode flow structures, which are not self-organized enough to maintain its trace in the mean flow.

---

---

## Bibliography

---

- [1] JS Baggett. On the feasibility of merging LES with RANS for the near-wall region of attached turbulent flows. Technical Report 1975, Center for Turbulence Research - Stanford University, 1998.
- [2] B. Basara, S. Krajnovic, S. Girimaji, and Z. Pavlovic. Near wall formulation of the partially averaged navier stokes (pans) turbulence model. *AIAA J.*, 49(12):2627–2636, 2011.
- [3] B. Basara, A. Poredos, and P. Goresek. Scale-resolving simulations of the flow in intake port geometries. *SAE Technical Paper 2016-01-0589*, 2016.
- [4] Branislav Basara, Sinisa Krajnovic, Zoran Pavlovic, and Per Ringqvist. Performance analysis of Partially-Averaged Navier-Stokes method for complex turbulent flows. In *6th AIAA Theoretical Fluid Mechanics Conference, Fluid Dynamics and Co-located Conferences*. American Institute of Aeronautics and Astronautics, June 2011.
- [5] P. Batten, U. Goldberg, and S. Chakravarthy. LNS - an approach towards embedded LES. *American Institute of Aeronautics and Astronautics*, 2002.
- [6] Paul Batten, Uriel Goldberg, and Sukumar Chakravarthy. Interfacing Statistical Turbulence Closures with Large-Eddy Simulation. *AIAA Journal*, 42(3):485–492, 2004.
- [7] M. Baumann, F. Di Mare, and J. Janicka. On the validation of large eddy simulation applied to internal combustion engine flows part II: Numerical analysis. *Flow, Turbulence and Combustion*, 92(1-2):299–317, 2014.
- [8] H. Baya Toda, O. Cabrit, K. Truffin, G. Bruneaux, and F. Nicoud. Assessment of subgrid-scale models with a large-eddy simulation-dedicated experimental database: The pulsatile impinging jet in turbulent cross-flow. *Physics of Fluids*, 26(7), 2014.
- [9] Martin Beaudoin and Hrvoje Jasak. Development of a generalized grid interface for turbomachinery simulations with openfoam. In *Open source CFD International conference*, volume 2, 2008.

## Bibliography

---

- [10] Brandt A. Belson, Jonathan H. Tu, and Clarence W. Rowley. Algorithm 945: modred - A Parallelized Model Reduction Library. *ACM Transactions on Mathematical Software*, 40(4):1–23, July 2014.
- [11] G. Berkooz, P. Holmes, and J. L. Lumley. The proper orthogonal decomposition in the analysis of turbulent flows. *Annual Review of Fluid Mechanics*, 25(16):539–575, 1993.
- [12] J. Borée, S. Maurel, and R. Bazile. Distruption of a compressed vortex. *Physics of Fluids*, 14(7):2543–2556, 2002.
- [13] Jacques Borée and Paul C. Miles. *In-Cylinder Flow*. John Wiley & Sons, Ltd, 2014.
- [14] J. Boussinesq. *Essai sur la théorie des eaux courantes*. Mémoires présentées par divers savants à l’Académie des Sciences. Imprimerie Nationale, 1877.
- [15] B. Merci C. De Langhe and E. Dick. Very Large Eddy Simulation and Rng Turbulence Models. In *15th AIAA Computational Fluid Dynamics Conference*, number c, page 3041, Reston, Virigina, June 2001. American Institute of Aeronautics and Astronautics.
- [16] Hao Chen, David L Reuss, and Volker Sick. On the use and interpretation of proper orthogonal decomposition of in-cylinder engine flows. *Measurement Science and Technology*, 23(8):085302, 2012.
- [17] Sergei G Chumakov and Christopher J Rutland. Dynamic structure subgrid-scale models for large eddy simulation. *International Journal for Numerical Methods in Fluids*, 47(8-9):911–923, March 2005.
- [18] Robert A. Clark, Joel H. Ferziger, and W. C. Reynolds. Evaluation of subgrid-scale models using an accurately simulated turbulent flow. *Journal of Fluid Mechanics*, 91(01):1, march 1979.
- [19] Sébastien Deck. Recent improvements in the zonal detached eddy simulation (zdes) formulation. *Theoretical and Computational Fluid Dynamics*, 26(6):523–550, 2012.
- [20] D. Dietzel, D. Messig, F. Piscaglia, A. Montorfano, G. Olenik, O. Stein, A. Kronenburg, A. Onorati, and C. Hasse. Evaluation of Scale Resolving Turbulence Generation Methods for Large Eddy Simulation of Turbulent Flows. *Computers & Fluids*, 93:116–128, 2014. <http://www.sciencedirect.com/science/article/pii/S0045793014000206>.
- [21] B. Enaux, V. Granet, O. Vermorel, C. Lacour, C. Pera, C. Angelberger, and T. Poinso. LES study of cycle-to-cycle variations in a spark ignition engine. *Proceedings of the Combustion Institute*, 33(2):3115–3122, January 2011.
- [22] P.E. Farrell and J.R. Maddison. Conservative interpolation between volume meshes by local galerkin projection. *Computer Methods in Applied Mechanics and Engineering*, 200(1–4):89 – 100, 2011.
- [23] P.E. Farrell, M.D. Piggott, C.C. Pain, G.J. Gorman, and C.R. Wilson. Conservative interpolation between unstructured meshes via supermesh construction. *Computer Methods in Applied Mechanics and Engineering*, 198(33-36):2632–2642, 2009.
- [24] J. H. Ferziger and M. Perić. *Computational Methods for Fluid Dynamics*. Springer, 3rd edition edition, 2002.
- [25] A. A. Fogleman, K. Lumley, D. Rempfer, and D. C. Haworth. Application of the proper orthogonal decomposition to datasets of internal combustion engine flows. *Journal of Turbulence*, 5(23):1–18, 2004.
- [26] Jochen Fröhlich and Dominic von Terzi. Hybrid LES/RANS methods for the simulation of turbulent flows. *Progress in Aerospace Sciences*, 44(5):349–377, 2008.

- [27] S. Girimaji. Partially-averaged navier-stokes model for turbulence: A reynolds-averaged navier-stokes to dns bridging method. *J. of App. Mech.*, 73:413–421, 2006.
- [28] D. Goryntsev, K. Nishad, A. Sadiki, and J. Janicka. Application of LES for Analysis of Unsteady Effects on Combustion Processes and Misfires in DISI Engine. *Oil & Gas Science and Technology – Revue d'IFP Energies nouvelles*, 69(1):129–140, January 2013.
- [29] D. Goryntsev, A. Sadiki, M. Klein, and J. Janicka. Analysis of cyclic variations of liquid fuel–air mixing processes in a realistic DISI IC-engine using Large Eddy Simulation. *International Journal of Heat and Fluid Flow*, 31(5):845–849, October 2010.
- [30] H. Guillard and C. Farhat. On the significance of the grometric conservation law for flow ccomputation on moving meshes. *Computer Methods in Applied Mechanics and Engineering*, 190:1467–1482, 2000.
- [31] W. Gyllenram and H. Nilsson. Design and Validation of a Scale-Adaptive Filtering Technique for LRN Turbulence Modeling of Unsteady Flow. *Journal of Fluids Engineering*, 130:051401, 2008.
- [32] K. Hanjalić, M. Hadžiabdić, L. Temmerman, and M. Leschziner. *Merging LES and RANS Strategies: Zonal or Seamless Coupling?*, pages 451–464. Springer Netherlands, Dordrecht, 2004.
- [33] C. Hasse. Scale-resolving simulations in engine combustion process design based on a systematic approach for model development. *International Journal of Engine Research*, 17(1):44–62, 2015.
- [34] Christian Hasse, Volker Sohm, and Bodo Durst. Detached eddy simulation of cyclic large scale fluctuations in a simplified engine setup. *Int. J. Heat Fluid Flow*, 30(1):32–43, 2009.
- [35] Christian Hasse, Volker Sohm, and Bodo Durst. Numerical investigation of cyclic variations in gasoline engines using a hybrid URANS/LES modeling approach. *Computers & Fluids*, 39(1):25–48, January 2010.
- [36] D. C. Haworth. Large-eddy simulation of in-cylinder flows. *Oil and Gas Science and Technology*, 54(2):175–185, 1999.
- [37] Philip Holmes, John L. Lumley, Gahl Berkooz, and Clarence W. Rowley. *Turbulence, Coherent Structures, Dynamical Systems and Symmetry*, volume 36. Cambridge University Press, Cambridge, March 2012.
- [38] Eberhard Hopf. A mathematical example displaying features of turbulence. *Communications on Pure and Applied Mathematics*, 1(4):303–322, December 1948.
- [39] B. Khalighi. Study of the intake tumble motion by flow visualization and particle tracking velocimetry. *Experiments in Fluids*, 10(4):230–236, 1991.
- [40] A N Kolmogorov. The Local Structure of Turbulence in Incompressible Viscous Fluid for Very Large Reynolds Numbers. *Proceedings: Mathematical and Physical Sciences*, 434(1890):9–13, 1991.
- [41] O. Laget, B. Reveille, L. Martinez, K. Truffin, and C. Habchi. LES calculations of a four cylinder engine. *SAE Technical Paper 2011-01-0832*, 2011.
- [42] LD Landau and EM Lifshitz. *Fluid mechanics: Landau and Lifshitz: course of theoretical physics*, volume 6. Elsevier, 2013.
- [43] J.T.C. Liu. Contributions to the Understanding of Large-Scale Coherent Structures in Developing Free Turbulent Shear Flows. pages 183–309. 1988.

## Bibliography

---

- [44] K. Liu and D. C. Haworth. Development and assessment of POD for analysis of turbulent flow in piston engines. *SAE technical paper 2011-01-0830*, 2011.
- [45] Kai Liu, Daniel C. Haworth, Xiaofeng Yang, and Venkatesh Gopalakrishnan. Large-eddy Simulation of Motored Flow in a Two-valve Piston Engine: POD Analysis and Cycle-to-cycle Variations. *Flow, Turbulence and Combustion*, 91(2):373–403, 2013.
- [46] Edward N. Lorenz. Deterministic Nonperiodic Flow. *Journal of the Atmospheric Sciences*, 20(2):130–141, March 1963.
- [47] J.L. Lumley. *Engines: An Introduction*. Cambridge University Press, 1999.
- [48] Amin Maghbouli, Tommaso Lucchini, Gianluca D’Errico, and Angelo Onorati. Effects of grid alignment on modeling the spray and mixing process in direct injection diesel engines under non-reacting operating conditions. *Applied Thermal Engineering*, 91:901 – 912, 2015.
- [49] J. Martínez, F. Piscaglia, A. Montorfano, A. Onorati, and S.M. Aithal. Influence of spatial discretization schemes on accuracy of explicit LES: Canonical problems to engine-like geometries. *Computers & Fluids*, 117(0):62 – 78, 2015. "<http://dx.doi.org/10.1016/j.compfluid.2015.05.007>".
- [50] F. R. Menter. Two-equation eddy-viscosity turbulence models for engineering applications. *AIAA Journal*, 32(8):1598–1605, 1994.
- [51] F.R. Menter and Y. Egorov. The scale adaptive simulation method for unsteady turbulent flow prediction, Part 1: Theory and Model Description. *Flow Turbul. Combust.*, 85:113–138, 2010.
- [52] F.R. Menter, M. Kuntz, and R. Langtry. Ten Years of Industrial Experience with the SST Turbulence Model. In K. Hanjalic, Y. Nagano, & M. Tummers, editor, *Turbulence, Heat and Mass Transfer 4*, pages 1598–1605. Begell House, Inc., 2003.
- [53] A. Misdariis, A. Robert, O. Vermorel, S. Richard, and T. Poinsot. Numerical Methods and Turbulence Modeling for LES of Piston Engines: Impact on Flow Motion and Combustion. *Oil and Gas Science and Technology - Rev. IFP Energies nouvelles*, 69(1):83–105, 2013.
- [54] A. Montorfano, F. Piscaglia, G. Baldassarra, A. Onorati, and S.M. Aithal. Application of a dynamic model with lengthscale-dependent RANS/LES hybrid functioning to a wind turbine simulation. In *3rd Symposium on OpenFOAM for wind energy*. Politecnico di Milano, 2015.
- [55] A. Montorfano, F. Piscaglia, and A. Onorati. A LES Study on the Evolution of Turbulent Structures in Moving Engine Geometries by an Open-Source CFD Code. *SAE Technical Paper 2014-01-1147*, 2014.
- [56] A. Montorfano, F. Piscaglia, and A. Onorati. An Extension of the Dynamic Mesh Handling with Topological Changes for LES of ICE in OpenFOAM. *SAE Technical Paper 2015-01-0384*, 2015.
- [57] A. Montorfano, F. Piscaglia, M. Schmitt, Y. M. Wright, C. E. Frouzakis, A. G. Tomboulides, K. Boulouchos, and A. Onorati. Comparison of direct and large eddy simulations of the turbulent flow in a valve/piston assembly. *Flow, Turbulence and Combustion*, 95(2):461–480, 2015.
- [58] F. Nicoud and F. Ducros. Subgrid-scale stress modelling based on the square of the velocity gradient tensor. *Flow, Turbulence and Combustion*, 62:183–200, 1999.

- [59] Franck Nicoud, Hubert Baya Toda, Olivier Cabrit, Sanjeeb Bose, and Jungil Lee. Using singular values to build a subgrid-scale model for large eddy simulations. *Physics of Fluids (1994-present)*, 23(8), 2011.
- [60] U. Piomelli, E. Balaras, H. Pasinato, K.D. Squires, and P.R. Spalart. The Inner-Outer Layer Interface in Large-Eddy Simulations with Wall-layer Models. *Int. J. Heat Fluid Flow*, 24:538–550, 2003.
- [61] F. Piscaglia, A. Montorfano, and A. Onorati. Development of a Non-Reflecting Boundary Condition for Multidimensional Nonlinear Duct Acoustic Computation. *Journal of Sound and Vibration*, 332(4):922–935, 2013. <http://dx.doi.org/10.1016/j.jsv.2012.09.030>.
- [62] F. Piscaglia, A. Montorfano, and A. Onorati. Development of Fully-Automatic Parallel Algorithms for Mesh Handling in the OpenFOAM-2.2.x Technology. *SAE Technical Paper 2013-24-0027*, 2013. <http://dx.doi.org/10.4271/2013-24-0027>.
- [63] F. Piscaglia, A. Montorfano, and A. Onorati. A Scale Adaptive Filtering Technique for Turbulence Modeling of Unsteady Flows in IC Engines. *SAE Int. J. Engines, Paper n. 2015-01-0395*, 2015. <http://dx.doi.org/10.4271/2015-01-0395>.
- [64] S.B. Pope. *Turbulent Flows*. Cambridge University Press, 2000.
- [65] Stephen B Pope. Ten questions concerning the large-eddy simulation of turbulent flows. *New Journal of Physics*, 6(1):35, 2004.
- [66] Jorge Raposo, Werner Hentschel, and Wolfgang Merzkirch. Analysis of the dynamical behavior of coherent structures in in-cylinder flows of internal combustion engines. In *In-Cylinder Flows of Internal Combustion Engines, 10th International Symposium on Applications of Laser Techniques to Fluid Mechanics*, number 1987, pages 1–8, 2000.
- [67] S. Richard, O. Colin, O. Vermorel, A. Benkenida, C. Angelberger, and D. Veynante. Towards large eddy simulation of combustion in spark ignition engines. *Proceedings of the Combustion Institute*, 31 II:3059–3066, 2007.
- [68] Stéphane Roudnitzky, Philippe Druault, and Philippe Guibert. Proper orthogonal decomposition of in-cylinder engine flow into mean component, coherent structures and random Gaussian fluctuations. *Journal of Turbulence*, 7(September 2015):1–19, January 2006.
- [69] C. J. Rutland. Large-eddy Simulations for Internal Combustion Engines - a Review. *Int. J. Eng. Res.*, (12):421–451, 2011.
- [70] P. Sagaut. *Large-Eddy Simulation for Incompressible Flows: an Introduction*. Scientific computation. Springer-Verlag, 2006.
- [71] Mikhail L. Shur, Philippe R. Spalart, Mikhail Kh Strelets, and Andrey K. Travin. A hybrid RANS-LES approach with delayed-DES and wall-modelled LES capabilities. *International Journal of Heat and Fluid Flow*, 29(6):1638–1649, December 2008.
- [72] L. Sirovich. Turbulence and the dynamic of coherent structures. *Quarterly of Applied Mathematics*, 45:561–590, 1987.
- [73] J. Smagorinsky. General circulation experiments with the primitive equations. i: the basic experiments. *Monthly Weather Review*, 91(3):99–165, 1963.

## Bibliography

---

- [74] P. R. Spalart, S. Deck, M. L. Shur, K. D. Squires, M. Kh Strelets, and A. Travin. A new version of detached-eddy simulation, resistant to ambiguous grid densities. *Theoretical and Computational Fluid Dynamics*, 20(3):181–195, 2006.
- [75] Spalart, P.R. Strategies for Turbulence Modelling and Simulations. *Int. J. Heat Fluid Flow*, 21(3):252–263, 2000.
- [76] Spalart, P.R. and Jou, W.H. and Stretlets, M. and Allmaras, S.R. Comments on the Feasibility of LES for Wings and on the Hybrid RANS/LES Approach. In *Advances in DNS/LES, Proceedings of the First AFOSR International Conference on DNS/LES*, 1997.
- [77] C.G. Speziale. A Combined Large-Eddy Simulation and Time-Dependent RANS Capability for High-Speed Compressible Flows. *J. Sci. Comput.*, 13(3):253–274, 1998.
- [78] The OpenFOAM<sup>®</sup> Foundation.
- [79] P.D. Thomas. Geometric conservation law and its application to flow computations on moving grids. *AIAA journal*, 17(10):1030–1037, 1979. cited By (since 1996)511.
- [80] D P Towers and C E Towers. Cyclic variability measurements of in-cylinder engine flows using high-speed particle image velocimetry. *Measurement Science and Technology*, 15(9):1917–1925, sep 2004.
- [81] TOYOTA MOTOR CORPORATION. Toyota Dynamic Force Engine. <http://newsroom.toyota.co.jp/en/download/14447840>.
- [82] A. Travin, M. Shur, M. Strelets, and P. R. Spalart. *Physical and Numerical Upgrades in the Detached-Eddy Simulation of Complex Turbulent Flows*, pages 239–254. Springer Netherlands, Dordrecht, 2002.
- [83] Travin, A.K. and Shur, M.L. and Spalart, P.R. and Strelets, M.K. Improvement of Delayed Detached-Eddy Simulation for LES with Wall Modelling. In *ECCOMAS CFD 2006: Proceedings of the European Conference on Computational Fluid Dynamics, Egmond aan Zee, The Netherlands, September 5-8, 2006*. Delft University of Technology; European Community on Computational Methods in Applied Sciences (ECCOMAS), 2006.
- [84] H. Weller. Controlling the computational modes of the arbitrarily structured C grid. *Monthly Weather Review*, 140:3220–3234, 2012.
- [85] W. Willems. *PhD thesis*. PhD thesis, Institut fur Technische Mechanik, RWTH Aachen, 1996.
- [86] Jie Zhong, David LS Hung, Zhenkan Wang, Yuyin Zhang, and Min Xu. Comparing the cycle-to-cycle variations of pulsing spray characteristics by means of ensemble image and probability presence image analysis techniques. In *Proceedings of 12th Triennial International Conference on Liquid Atomization and Spray Systems, Heidelberg, Germany*, 2012.